A Study of the Late-Stage Mineralogy of Agpaitic Environments: Borosilicates, Niobate Hydrates and Development of Laser Ablation ICP-MS as a Tool to Analyze for High Concentrations of Light Elements (Li, Be, and B)

by

Monika Magdaline-Marion Haring

A thesis submitted in partial fulfillment
of the requirements for the degree of
Doctor of Philosophy (PhD) in Mineral Deposits and Precambrian Geology

The Faculty of Graduate Studies
Laurentian University
Sudbury, Ontario, Canada

THESIS DEFENCE COMMITTEE/COMITÉ DE SOUTENANCE DE THÈSE
Laurentian Université/Université Laurentienne
Faculty of Graduate Studies/Faculté des études supérieures

Title of Thesis Titre de la thèse	A Study of the Late-Stage Mineralogy of Agpaitic Environments: Borosilicates, Niobate Hydrates and Development of Laser Ablation ICP-MS as a Tool to Analyze for High Concentrations of Light Elements (Li, Be, and B)
Name of Candidate Nom du candidat	Haring, Monika Magdaline-Marion
Degree Diplôme	PhD
Department/Program Département/Programme	Mineral Deposits and Precambrian Geology
Date of Defence Date de la soutenance	Oct 25, 2017

APPROVED/APPROUVÉ

Thesis Examiners/Examinateurs de thèse:

Dr. Andrew M. McDonald
(Supervisor/Directeur de thèse)

Dr. Michael Schindler
(Committee member/Membre du comité)

Approved for the Faculty of Graduate Studies
Approuvé pour la Faculté des études supérieures
Dr. David Lesbarrères
Monsieur David Lesbarrères
Dean, Faculty of Graduate Studies
Doyen, Faculté des études supérieures

Dr. Sytle Antao
(External Examiner/Examinateur externe)

Dr. Joy Gray-Munro
(Internal Examiner/Examinateur interne)

ACCESSIBILITY CLAUSE AND PERMISSION TO USE

Abstract

To date, over 400 mineral species have been discovered at Mont Saint-Hilaire (MSH) many of which are new to science. These new minerals tend to occur as late-stage phases with an enrichment high field strength elements (HFSE) (*i.e.* Nb, Ti, Zr) as well as light elements (*i.e.* Li, Be and B). Characterization of these minerals has been hindered by their small crystal sizes (*i.e.* μm scale) as well as enrichment in light elements. This thesis discusses the chracterization and overall implications of franconite group minerals as well as the new boro silicate minerals steedeite and nolzite. Finally the effectiveness of laser ablation ICP-MS as a method of accurately measuring major concentrations of light elements is discussed.

Franconite group minerals (FGM) are hydrous-alkali niobates, inferred to have formed from Nb-rich precursor minerals at low temperatures (~150 °C). The structures of these minerals are held together by hydrogen bonds and are highly flexible with Na, Ca, Mg and possilbly Fe^{2+} and K substituting for one another. Although FGM are Nb-rich, they are notably devoid of Ta despite the two elements being geochemical twins. The FGM are crystallo-chemically similar to scandia octahedral molecular sieves, a group of synthetic compounds known for their cation exchange properties.

Twelve borosilicate phases, including the new minerals steedeite and nolzeite are known from MSH. These are crystallo-chemically similar, both minerals containing of single loop-branched *dreier* chains in their structures. Such chains occur in synthetic compounds (*e.g.* $Li_2Mg_2[Si_4O_{11}]$) but are not known to occur in other naturally occurring minerals. Steedeite is highly ordered with respect to Si and B whereas nolzeite contains a mixed Si/B site despite the two minerals being associated with one another.

Accurate chemical analysis of late-stage minerals, rich in light elements, is hindered by the fact that such elements have low atomic masses. Laser ablation ICP-MS analysis of a variety of mienrals with major concentrations of light elements gave measured concentrations of Li, Be and B that were within ± 10% of expected ideal values for most minerals. Beam widths varying from 6 to 30 μm were employed however; they had no effect on the measured light element concentrations. Four standards including the NIST610 & 612 glasses, natural beryl, and lithium metaborate were used. Of these NIST610 is considered the most suitable as it has the smallest associated errors (1σ error: ± 0.05 to ± 1.68 ppm). Based on this LA-ICP-MS is considered to be a suitable alternative to secondary ion mass spectrometry for analysis of light elements.

Kewords: Mont Saint-Hilaire, steedeite, nolzeite, franconite, charleshatchettite, high field strength elements, light elements, laser ablation ICP-MS,

Co-Authorship Statement

This thesis consists of five manuscripts. Sample preparation and analysis as well as the results and conclusions are the work of the candidate. The five manuscripts are co-authored by Dr. Andrew McDonald who provided samples, guidance as well as edited the manuscripts. Chapter 6 is also co-authored by Dr. Joe Petrus who also provided guidance and expertise. Four of the manuscripts that make up this thesis have been published in peer reviewed journals:

Chapter 2 is published in the February 2014 issue of Canadian Mineralogist and was reviewed by Dr. Daniella Pinto and Dr. Stewart Mills.

Chapter 3 is published February 2017 issue of Mineralogical Magazine and was reviewd by Dr. Edward S. Grew and Dr. Joel Grice.

Chapter 4 is published in the June 2014 issue of Mineralogical Magazine and was reviewed by Dr. Peter Leverett.

Chapter 5 has been accepted for publication by American Mineralogist and was reviewed by Dr. Anthony Kampf.

Acknowledgements

I would like to thank my supervisor Dr. Andrew McDonald for their input and guidance. I would also like to acknowledge Dr. William Zhe, Dr. Joe Petrus, Dr. Joy Gray-Munro, Mark A. Cooper, and Ravinder Sidhu for their contributions and support of the analytical techniques throughout this project. Finally, I would like to thank Dr. Frank C. Hawthorne for providing access to the the four-circle diffractometer at the University of Manitoba.

For their moral support and encouragement throughout this project I would like to thank Roxanne Mehes, Edda Bozatto as well as my family. In addition to his encouragement, I am grateful to my husband Tyler August for providing IT support throughout this project. I am also thankful to my fellow graduate students especially Remy Poulin, Chris Beckett-Brown, and Evan Hastie for their friendship.

Table of Contents

List of Tables

List of Figures

Chapter 1

Introduction to Thesis

1.1 Background

1.1.1 Peralkaline and Alkaline rocks

Peralkaline rocks occur worldwide, generally within intraplate settings, where they form intrusive complexes, parts of complexes, or late-stage pegmatites and veins in non-peralkaline complexes. Notable examples of peralkaline complexes include, Ilimaussaq (Greenland), Lovozero and Khibina (Russia) as well as Mont Saint-Hilaire (Sorensen 1997). The agpaitic or peralaklinity index, first defined by Ussing (1912), is given as $(Na + K)/Al \geq 1.2$. More recently, it has been suggested that the term peralkaline be applied strictly to peralkaline nepheline syenites containing complex Zr and Ti minerals such as eudialyte and mosandrite rather than simple minerals such as zircon and ilmenite (Le Maitre 1989). In this sense, a simple peralkalinity index > 1 should not necessarily be soley used to define a system as being peralkaline. As an example, there are two nepheline syenites, located near McGerrigle, QC, that have identical agpaitic indices of 1.09, yet one was found to contain the minerals zircon and biotite whereas the other contains arfvedsonite, aegirine and eudialyte (Wallace et al. 1990). Evidence for changing alkalinity, such as zircon overgrown by eudialyte and vice versa, has been previously observed in peralkaline rocks (Sorensen 1997). In light of the variability that exists within peralkaline rocks as a whole, Khomyakov (1995) subdivided them into five subgroups based on differences in compositions of rare-element and accessory minerals. The five subgroups include: hyperagpaitic, highly agpaitic, medium agpaitic, low agpaitic, and miaskitic, and their characteristic mineralogy is given in table 1-1.

Geochemically, peralkaline rocks are characterized by high to extreme concentrations of Na, Zr, Cl, F as well as rare-elements such as Li, Be, Rb, Ga, REE, Nb, Ta, Hf, Zn, Sn, U and Th along with depletions in elements such as Mg, Ca, Cr, Sc, Co and Ni. Some peralkaline complexes contain economic concentrations of rare-metals. Both the Lovozero and Ilimaussaq complexes are considered as sources of Zr, Hf, REE, Y and Nb (Sorensen 1997). The compositions of peralkaline rocks suggest that the melts from which they crystallized were rich in Na, rare-elements (listed above) and volatiles (Sorensen 1997). Both $^{87}Sr/^{86}Sr$ and $^{143}Nd/^{144}Nd$ ratios suggest that peralkaline melts are ultimately mantle derived (Currie et al. 1986, Wallace et al. 1990, Kramm et al. 1993, Moreau et al. 1996). In some peralkaline rocks however, $^{87}Sr/^{86}Sr$ values are higher than expected suggesting that peralkaline melts may have undergone some crustal contamination (Currie et al. 1986). The mantle derived melts from which peralkaline rocks fractionate are inferred to be nephelinitic and alkali basaltic in nature (Sorensen 1997). During the latest stages of fractionation, a transition occurrs from low temperature (~ 400 to 500 °C) peralkaline melts rich in volatiles to hydrothermal fluids. These hydrothermal fluids result in late- to post-magmatic alteration of peralkaline rocks and lead to the formation of mineral rich pegmatites and veins as well as hyperagpaitic mineral assemblages. A hyeragpaitic mineral assemblage may include unusual Na – rich minerals such as natrosilite, ussingite, villiaumite, and analcime as well as other important minerals including Li-arfvedsonite, zirsinalite, vuonnemite, lomonosovite, vitusite, chkalovite and steenstrupine (Sorensen 1997).

1.1.2 Mont Saint-Hilaire

Mont Saint-Hilaire (MSH) is a small (~ 3 km in diameter) alkaline intrusion located 40 km east of Montreal, Québec. This intrusion is part of the Monteregian Hills, an east-west trending line of separate yet related intrusions. Three rock suites at MSH have been recognized by Currie *et*

al. (1986) including the Sunrise Suite, Pain du Sucre suite and the East Hill suite. The Sunrise suite is the oldest of the three rock suites, having been emplaced at 134 +/- 6 Ma and consists of alkaline gabbros. The Pain du Sucre suite is younger having been emplaced at 120 +/- 6 Ma and consists of biotite gabbros and nepheline diorites. Finally, the East Hill Suite was emplaced concurrently with the Pain Du Sucre Suite. It however consists of nepheline and sodalite syenites (Currie *et al*. 1986). Of the three rock suites found at MSH, the East Hill Suite contains the greatest diversity of minerals, many of which are only known to occur and MSH. Due to the peralkaline nature of the MSH intrusion, many of these minerals are enriched in incompatible elements such as rare-earth elements (REE), high-field strength elements (HFSE; Ti, Zr, Nb) and large-ion lithophile elements (LILE; Na, K, Li). Subsequent to crystallization, MSH underwent a hydrothermal alteration phase in which rocks underwent a low temperature (< 340 °C) interaction with residual magmatic fluids as well as external fluids derived from the surrounding sediments. This fluid-rock interaction is likely to have caused dissolution of pre-existing minerals, transport of REE, HFSE and LILE, and re-precipitation of characteristic mineral assemblages (Schilling *et al*. 2011).

This may have created the variety of microenvironments found at MSH. The greatest microenvironment diversity is found within the East Hill Suite: pegmatites, altered pegmatites, marble xenoliths, sodalite syenites, nepheline syenites, igneous breccias, sodalite syenite xenoliths and hornfels. These microenvironments and their mineralogy are described in detail in a review by Horvath and Gault (1990).

1.2 Research Problems

Over 400 new mineral species have been discovered at Mont Saint – Hilaire to date with many of these species being new to science (Horvath & Gault 1990, Schilling et al. 2011). This thesis is part of the on going study of the late-stage mineralogy of Mont Saint-Hilaire, Quebec. These minerals typically occur as extremely small crystals (μm scale), making the study of these crystals difficult using conventional single crystal instrumentation. A characterization of the crystal-chemistry of late-stage minerals and their associated mineral assemblages can give important insights into the late stage-evolution of peralkaline intrusions.

As late-stage phases these new minerals can contain high concentrations of HFSE such as Nb as well as light elements - Li, Be and B. Given that Li, Be and B maybe important constituents of late stage minerals in peralkaline intrusions, it is necessary to obtain accurate chemical analyses for these elements. Due to their low atomic masses it can be difficult to analyse for Li, Be and B using standard techniques such as electron microprobe analyses (EMPA). Other techniques such as secondary ion mass spectrometry are difficult to access as well as costly. In this thesis, the effectiveness of laser ablation ICP-MS for measuring light elements in major concentrations in minerals will be tested.

1.3 Thesis Objectives

The objectives to this thesis are to:

1) Solve crystal structures for the late-stage minerals: steedeite, nolzeite, franconite and charleshatchettite.

2) Discuss the origin of the new minerals steedeite, nolzeite, and charleshatchettite and their implications for the late-stage evolution of Mont Saint-Hilaire.
3) Discuss the relationship between the related minerals steedeite and nolzeite.
4) Dicuss how steedeite and nolzeite are related to other borosilicate minerals
5) Test the effectiveness of laser ablation ICP-MS in measuring light elements including Li, Be and B in major concentrations in minerals.
6) Discuss the relationship between franconite and charleshatchettite as well other franconite group minerals.

1.4 Structure of Thesis

This thesis is divided up into six chapters with chapter two to six written in a manuscript format. Chapter 2, entitled "Steedeite, $NaMn_2[Si_3BO_9](OH)_2$: Characterization, crystal-structure determination and origin" provides a detailed description of the new mineral steedeite and its crystal structure. The origin and possible implications for the late-stage evolution of Mont Saint-Hilaire are also discussed.

Chapter 3, entitled "Nolzeite, $Na(Mn,\square)_2[Si_3(B,Si)O_9(OH)_2]\bullet 2H_2O$, a new pyroxenoid mineral from Mont Saint-Hilaire, Quebec, Canada" provides a detailed description of the new mineral nolzeite and its crystal structure. The origin and possible implications for the late-stage evolution of Mont Saint-Hilaire are also discussed. This paper also discusses the relationship between nolzeite and the closely related mineral steedeite.

Chapter 4, entitled "Franconite, $NaNb_2O_5(OH)\bullet 3H_2O$: Structure determination and the role of H-bonding, with comments on the crystal-chemistry of franconite-related minerals" provides, for

the first time, a detailed description of the crystal structure of franconite. Its relationship with chemically similar mineral species such as hochelagaite and ternovite is also discussed.

Chapter 5, entitled "Charleshatchettite, $CaNb_4O_{10}(OH)_2 \cdot 8H_2O$, a new mineral from Mont Saint-Hilaire, Québec, Canada: Description, Crystal-Structure Determination and Origin" provides a detailed description of the new mineral charleshatchettite and its crystal structure. The origin and possible implications for the late-stage evolution of Mont Saint-Hilaire are also discussed. Finally the relationship between franconite group minerals and Scandia octahedral molecular sieves (SOMS), a group of compounds known for their cation exchange capabilities, is discussed

Chapter 6, entitled "Quantitative analysis of major concentrations of Li, Be and B in silicate, borosilicate, and borate minerals using LA-ICP-MS" discusses the effectiveness of LA-ICP-MS for measuring light elements (i.e. Li, Be and B) in silicate, borosilicate, and borate minerals. These minerals contain light elements in variable albeit major concentrations.

1.5 References

Currie, K.L., Eby, G.N. & Gittins, J. (1986): The petrology of the Mont Saint Hilaire complex, southern Quebec: an alkaline gabbro-peralkaline syenite association. Lithos, 19, 65-81.

Horváth, L. & Gault, R.A. (1990): The mineralogy of Mont Saint-Hilaire Québec. Mineralogical Record, 21, 284-359.

Le Maitre, R.W. (ed). (1989): A Classification of Igneous Rocks and Glossary of Terms. Blackwell, Oxford, 193 pp

Khomyakov, A.P. (1995): Mineralogy of hyperagpaitic alkaline rocks. Oxford Scientific Publications. Clarendon Press, Oxford, 222 pp.

Kramm, U., Kogarko, L.N., Kononova, V.A., & Vartiainen, H. (1993) The Kola Alkaline Province of the CIS and Finland: precise Rb-Sr ages define 380-360 Ma age range for all magmatism. Lithos, 30, 33-44.

Moreau, C., Ohnenstetter, D., Demaiffe,D., & Robineau, B. (1996): The Los Archipelago nepheline syenite ring-structure: a magmatic marker of the evolution of the central and equatorial Atlantic. Canadian Mineralogist, 34, 281-99.

Schilling, J., Marks, M.A.W., Wenzel, T., Vennemann, T., Horvath, L., Tarassoff, P., Jacob, D.E., & Markl, G. (2011): Magmatic to hydrothermal evolution of the intrusive Mont Saint-Hilaire complex: insights into the late-stage evolution of peralkaline rocks. Journal of Petrology, 52, 2147-2185.

Sorensen, H., (1997) The agpaitic rocks – an overview*, Mineralogical Magazine, 61, 485-498.

Wallace, G.M., Whalen, J.B. and Martin, R.F. (1990): Agpaitic and miaskitic nepheline syenites of the McGerricle plutonic Complex, GaspeÂ, Quebec: An unusual petrological association. Canadian Mineralogist, 28, 251-66.

Table 1-1. Characteristic mineralogy of peralkaline rock subgroups after Khomyakov (1995).

Peralkaline subgroup	Characteristic minerals
Hyperagpaitic	zirsinalite, vuonnemite, vitusite, steenstrupine, chkalovite, etc. together with Li-arfvedsonite, ussingite, natrosilite, villiaumite
Highly Agpaitic	eudialyte, lamprophyllite, astrophyllite, Li-arfvedsonite, aenigmatite, nepheline, analcime, sodalite, villiaumite
Medium Agpaitic	apatite, titanite, arfvedsonite, nosean
Low Agpaitic	eudialyte, lavenite, titanite, zircon, apatite, katophorite
Miaskitic	allanite, zircon, ilmenite, hastingsite

Chapter 2

Steedeite, $NaMn_2[Si_3BO_9](OH)_2$: Characterization, Crystal-Structure Determination and Origin

2.1 Abstract

Steedeite (2013 – 052), ideally $NaMn_2Si_3BO_9(OH)_2$, is a new mineral discovered in altered sodalite syenite at the Poudrette quarry, La Vallée-du-Richelieu, Montérégie (formerly Rouville County), Québec, Canada. Crystals of steedeite are colourless to pale pink, and acicular with average dimensions of 0.006 x 0.011 x 0.51 mm. They occur as radiating to loose, randomly oriented groupings within vugs associated with aegirine, nepheline, sodalite, eudialyte-group minerals, analcime, natron, pyrrhotite, catapleiite, and two other unidentified minerals temporarily designated UK78 and UK80. The mineral is transparent to translucent with a vitreous lustre and has a weak pale green to pale yellow fluorescence under medium-wave radiation. The Mohs hardness could not be measured owing to the small size of the crystals. No partings or cleavages were observed although crystals exhibit an uneven fracture. The calculated density is 3.106 g/cm^3. Steedeite is nonpleochroic, biaxial with n_{min} = 1.636(2) and n_{max} = 1.656(2) and a positive elongation. Chemical analyses (n = 14) from seven crystals gave an average (range, standard deviation) of: Na_2O 7.51 (6.78 – 8.32, 0.44), CaO 0.17 (0.08 – 0.22, 0.03), MnO 31.02 (29.91 – 32.83, 0.93), FeO 0.86 (0.76 – 1.01, 0.07), SiO_2 46.34 (40.39 – 49.29, 2.56), S 0.39 (**b.d.* –- 2.36, 0.71) (**b.d. = below detection*), B_2O_3 (calc.) 8.73, and H_2O (calc.) 4.52, total 99.53 wt. %. The empirical formula, based on 11 oxygens, is $Na_{0.97}(Mn_{1.75}Fe_{0.05}Ca_{0.01})_{\sum 1.83}(Si_{3.07}S_{0.02})_{\sum 3.09}BO_9(OH)_2$ or ideally $NaMn_2Si_3BO_9(OH)_2$. The

presence of B and OH in steedeite is inferred from results from the single-crystal X-ray refinement. The presence of OH was also inferred based on the Raman spectrum of steedeite which contained bands consistent with O-H stretching. Steedeite crystallizes in space group $P\bar{1}$ (#2) with *a* 6.837(1), *b* 7.575(2), *c* 8.841(2) Å, α 99.91(3), β 102.19, γ 102.78(3)°, *V* 424.81 Å^3, and *Z* = 2. The strongest six lines on the *X*-ray powder-diffraction pattern [*d* in Å (I) (*hkl*)] are: 8.454 (100) ($00\bar{1}$), 7.234 (39) ($0\bar{1}0$), 3.331 (83) ($1\bar{2}1$, $0\bar{1}\bar{2}$, $20\bar{1}$, $1\bar{1}2$), 3.081 (38) ($0\bar{2}\bar{1}$), 2.859 (52) ($0\bar{1}3$), and 2.823 (80) ($21\bar{1}$). The crystal structure of steedeite was refined to *R* = 1.68 % and wR^2 = 4.96 % for 15061 reflections ($F_o > 4\sigma F_o$). The crystal structure is based on silicate chains with a periodicity of three (*i.e.*, *dreier* chain) consisting of four-membered borosilicate rings of the composition $[BSi_3O_9(OH)_2]^{5-}$. The borosilicate chains are classed as single loop-branched *dreier* chains that are linked together through shared corners to bands of edge-sharing $MnO_5(OH)$ octahedra. Steedeite is a chain silicate mineral closely related to the sérandite – pectolite series of the pyroxenoid group and is the first mineral found to contain single loop-branched *dreier* silicate chains.

2.2 Introduction

Steedeite, ideally $NaMn_2Si_3BO_9(OH)_2$, is a new borosilicate from Mont Saint-Hilaire, Québec, Canada, one of the world's most prolific localities for new minerals. The mineral occurs as fine acicular crystals which prohibited the determination of its structure via four-circle diffractometers using Scintillation detectors. Collection of data required for determination of the crystal structure of steedeite has now been made possible, owing to recent advancements in single-crystal X-ray diffraction instrumentation including high-flux sources and charge coupled detectors of greater sensitivity. This was critical not only to confirming the presence of both H_2O and (OH) in the mineral but also in the recognizing the mineral contains essential B_2O_3. In

this contribution we present the crystal structure and chemical composition of steedeite, elucidate the relationship of the mineral to those of the sérandite – pectolite series and provide insights into the conditions that led to its formation. The mineral has been named steedeite for Mr. Anthony Hosford Steede (*b*. 1940) in recognition of his contributions to understanding the mineralogy of Mont Saint-Hilaire. Both the mineral and mineral name have been approved by the International Mineralogical Association, Commission on New Minerals and Mineral Names (2013 – 052). The holotype material is housed in the collections of the Department of Natural History, Royal Ontario Museum (Toronto, Ontario, Canada), catalogue number M56489.

2.3 Occurrence

Steedeite was discovered by Col. Quintin Wight in August 1987 and was temporarily designated UK79. Crystals of steedeite were discovered in ~ 1 cm diameter vugs in a loose boulder (~1 x 1 m) of sodalite syenite at the Poudrette quarry, La Vallée-du-Richelieu, Montérégie (formerly Rouville County), Québec, Canada (45°33′8″N, 73°9′3″W). The loose boulder was found in the south-east portion of the quarry, in proximity to a large number of so-called sodalite syenite xenoliths (tawites) in nepheline syenite (McDonald & Chao 2010, McDonald & Chao 2005). The boulder containing steedeite was first noted owing to the high concentration of relatively thick, euhedral plates of pyrrhotite contained within it. When the boulder was broken up, numerous, centimetre-sized vugs filled with clear, crystalline natron ($Na_2CO_3 \bullet 10H_2O$) or natrite (Na_2CO_3) were exposed. These minerals subsequently decrepitated to thermonatrite ($Na_2CO_3 \bullet H_2O$) and related minerals. The sample containing steedeite consists predominantly of microcline, analcime, nepheline along with aegirine, and pyrrhotite (Table 2-1). The pyrrhotite associated with steedeite is magnetic, suggesting that it is the monoclinic 4*C* polytype. The rest of the sample is dominated by sodalite, a eudialyte-group mineral, sérandite, and thermonatrite

(Table 2-1). Some crystals of sodalite are found to retain their violet color even after prolonged (*i.e.*, several years) to the atmosphere. The sérandite is highly unusual for the locality ranging in colour from dark to pale green and brown to light brown in colour unlike the much more typical pink to orange colouration that characterizes the mineral in other environments at MSH. It may also be noteworthy that sérandite and steedeite have not been found together in the same vug considering the crystal-chemical similarities between them. In addition, there are also two rare, unidentified minerals, tentatively referred to as UK78 and UK80 (Table 2-1). The unidentified minerals like steedeite, also appear to be late stage phases, however the three minerals have not been found together in the same vug.

2.4 Physical and Optical Properties

Crystals of steedeite are euhedral, acicular and elongate along [001], occurring in slightly radiating to loose, randomly oriented groupings ('nests') (Figure 2-1). They exhibit the forms pinacoid {100} (dominant), as well as the pinacoids {010} and {001} (minor). Crystals have average dimensions 0.006 x 0.01 x 0.5 mm with average length-to-width ratios of ~ 46 – 85. They are pale pink to colourless with a white streak and a vitreous lustre. Steedeite is unusual in that its crystals exhibit a weak pale green to pale yellow fluorescence under medium-wave radiation (no fluorescence was observed under short- or long-wave radiation). To date, the only other mineral from MSH known to exhibit fluorescence under medium-wave radiation is lalondeite, $(Na,Ca)_6(Ca,Na)_3Si_{16}O_{38}(F,OH)_2 \bullet 3H_2O$ (McDonald & Chao 2009). Due to the small size of the crystals, a Mohs' hardness could not be measured. A density of 3.106 g/cm^3 was calculated using the empirical chemical formula and unit-cell parameters derived from the crystal-structure analysis.

Steedeite is assumed to be a biaxial, based on symmetry. It exhibits a positive elongation and refractive indices of n_{min} = 1.636(2) and n_{max} = 1.656(2) as measured with a Na-vapour lamp (λ = 589 nm). A complete set of optical data could not be collected due to the small crystal sizes and highly acicular nature of the mineral. No pleochroism was observed. The Gladstone-Dale value, calculated using the empirical formula and unit-cell parameters derived from the crystal structure analysis, has a compatibility index of 0.003 and is considered superior (Mandarino 1981).

2.5 Chemical Composition

Chemical analyses of steedeite were collected using a JEOL JSM 6400 scanning electron microscope equipped with an energy dispersive spectrometer and operating conditions of: voltage = 20 kV, ~1 nA beam current and a ~1 um beam width. Energy-dispersive data were collected using the following standards: albite (Na*K*α), perovskite (Ca*K*α), tephroite (Mn*K*α, Si*K*α), and chalcopyrite (Fe*K*α, S*K*α). Chemical analyses (n = 14) of seven crystals gave an average (range, standard deviation) of: Na_2O 7.51 (6.78 – 8.32, 0.44), CaO 0.17 (0.08 – 0.22, 0.03), MnO 31.02 (29.91 – 32.83, 0.93), FeO 0.86 (0.76 – 1.01, 0.07), SiO_2 46.34 (40.39 – 49.29, 2.56), S 0.39 (**b.d.* –- 2.36, 0.71) (**b.d. = below detection*), B_2O_3 (calc.) 8.73, and H_2O (calc.) 4.52, total 99.53 wt. %. The presence of elements including B and H were confirmed through a combination of crystal structure and Raman analyses (see below), respectively. The empirical formula based on 11 anions is $Na_{0.97}(Mn_{1.75}Fe_{0.05}Ca_{0.01})_{\sum 1.83}(Si_{3.07}S_{0.02})_{\sum 3.09}BO_9(OH)_2$ or ideally $NaMn_2Si_3BO_9(OH)_2$. The ideal formula requires: Na_2O 7.63, MnO 34.95, SiO_2 44.40, B_2O_3 8.58, and H_2O 4.44 wt. %, total 100.00 wt. %. Steedeite does not effervesce in 10% HCl at room temperature.

2.6 Raman Spectroscopy

A Raman spectrum of steedeite, based on an average of three 20 s acquisition cycles over a range of 50 to 4000 cm^{-1}, was collected using a Horiba Jobin Yvon XPLORA Raman spectrometer interfaced with an Olympus BX41 microscope. An excitation radiation of $\lambda = 638$ nm was used along with a 600 grating and 100 x magnification (producing a beam of diameter ~ 2 μm). The excitation radiation of $\lambda = 638$ nm was chosen to minimize fluorescence peaks in the region of ~2000 to 2800 cm^{-1} that were observed with the more commonly used radiation of $\lambda = 532$ nm. Calibration was made using the 521 cm^{-1} line of a silicon wafer. The Raman spectrum (Figure 2) contains five absorption bands located at regions ~ 50 – 500 cm^{-1}, 575 – 750 cm^{-1}, 825 – 1075 cm^{-1}, 1500 – 2000 cm^{-1}, and 3250 – 3500 cm^{-1}. In the first region (~ 50 – 500 cm^{-1}) five weak to strong bands at 120, 197, 264, 330, and 431 cm^{-1} are present. Bands at 197, 264, 330 and 430 cm^{-1} are attributed to Mn-O bonding (Table 2-2) based on data from Julien *et al*. (2004) for manganese oxide minerals such as pyrolusite, ramsdellite, and birnessite. The bands at 330 and 430 cm^{-1} could not be unequivocally assigned due to overlap between lower frequency Mn-O and Na-O, Si-O-Si and Si-O-B bands, respectively (Julien *et al*. 2004, Williams 1995). In the second (575-750 cm^{-1}), one very strong band at 636 cm^{-1} and a weaker band at 696 cm^{-1} are present. These are attributed to Si-O-Si and Si-O-B bending (Williams 1995, Frost *et al*. 2007), although there is potential for overlap as absorption peaks for Mn-O can occur at similar frequencies (Julien *et al*. 2004) (Table 2-2). The third region (~ 800-1075 cm^{-1}) consists of four moderately strong bands at 826, 874, 1000, and 1030 cm^{-1}. The bands at 826 and 874 cm^{-1} are attributed to symmetric stretching of Si-O bonds and bands at 1000 and 1030 cm^{-1} to asymmetric stretching of Si-O bonds (Williams 1995; Table 2-2). Alternatively, the two bands at 1000 and

1030 cm^{-1} could also be attributed to B-O stretching based on data from Frost *et al*. (2007) for ferroaxinite. Two additional bands at 1368 and 1700 cm^{-1} remain unassigned. The fifth region (~3250 and 3500 cm^{-1}) contains two moderately strong bands at 3317 and 3443 cm^{-1} attributed to O-H bending (Williams 1995). Given the chemical and structural similarities between steedeite and sérandite, a Raman spectrum of pink sérandite from MSH was collected (Figure 2-2). Results indicate the two spectra are very similar except that the Raman spectrum for steedeite contains additional weak to moderately strong bands at 826 and 874 cm^{-1}. These additional bands are likely due to the orientation of the steedeite crystals.

2.7 *X*-ray Crystallography and Crystal-Structure Determination

Powder *X*-ray diffraction data were collected using a 114.6 mm diameter Gandolfi camera, 0.3 mm collimator, and Fe-filtered Co*K*α radiation (λ = 1.7902 Å). Intensities were determined using a scanned image of the powder pattern and normalized to the measured intensity of d = 8.454 Å (I = 100). A theoretical powder pattern was calculated using the results from the crystal-structure analysis and the program CRYSCON (Dowty 2002) and was in good agreement with the measured powder pattern (Table 2-3).

X-ray intensity data were collected on a Bruker D8 three-circle diffractometer equipped with a rotating-anode generator, multi-layer optics incident beam path and an APEX-II CCD detector. An excess sphere of X-ray diffraction data (15061 reflections) was collected to 60° 2θ using 20 s per 0.3° frame with a crystal-to-detector distance of 5 cm. The unit-cell parameters were obtained by least-squares refinement of 14135 reflections ($I > 10\sigma I$), and are given in Table 2-3. Empirical absorption corrections (SADABS; Sheldrick, 1998) were applied and identical data

merged to give 15014 reflections covering the entire Ewald sphere. Information pertaining to the data collection is given in Table 2-4.

Solution and refinement of the crystal structure of steedeite were done using SHELXL – 97 (Sheldrick 1997). The crystal structure was solved by direct methods, using the scattering curves of Cromer & Mann (1968) and the scattering factors of Cromer & Liberman (1970). Phasing of a set of normalised structure factors gave the mean $|E^2 - 1|$ value of 0.996, consistent with a centrosymmetric space group. In light of this and the absence of systematic extinctions, $P\bar{1}$ was selected as the correct space group. Phase-normalised structure factors were used to give a difference Fourier map from which one *Na*, three *Si*, two *Mn*, and several *O* sites were located. From subsequent difference-Fourier maps, a [4]-coordinated site was located with bond distances ranging from 1.467to 1.509 Å, consistent with B-O bond lengths observed in other minerals (e.g., vistepite [$SnMn_4B_2Si_4O_{16}(OH)_2$; Hybler *et al*. 1997], bobtraillite [$(Na,Ca)_{13}Sr_{11}(Zr,Y,Nb)_{14}Si_{42}B_6O_{132}(OH)_{12} \bullet 12H_2O$; McDonald & Chao 2005], and reedmergnerite [$NaBSi_3O_8$; Appleman & Clark 1965]); on this basis, the site was assigned to B. Refinement of the site-occupancy factors (SOF) indicated that all of cation and anion sites are fully occupied, a point particularly relevant when discussing the nature of Si-B ordering in steedeite (Table 2-5). Determination of which *O* sites were occupied by OH was based on bond-valence calculations and electroneutrality considerations (Table 2-7). At the later stages of refinement, two *H* sites were located in the difference Fourier maps. These hydrogen sites were inserted into the refinement and the H-O distances were constrained to be close to 0.98 Å. Refinement of this model converged to R = 1.68 % and wR^2 = 4.96%.

2.8 Crystal Structure

The crystal structure of steedeite contains three *Si* sites, two *Mn* sites, and one unique site for *Na* and *B* (Table 2-5). The three *Si* sites are coordinated by four crystallographically distinct O atoms with Si-O bond lengths ranging from 1.602(1) to 1.657(1) Å (Table 2-6; Jacobsen *et al.* 2000). The B site is coordinated by two O atoms and two (OH) groups, forming $BO_2(OH)_2$ tetrahedra with B-(O,OH) bond lengths ranging from 1.467(2) to 1.508(2) Å where both the shortest and longest bond distances correspond to B-OH bonds (Table 2-6). The $BO_2(OH)_2$ tetrahedra is not unique to steedeite, as it can also be found in synthetic phases including $Pb_6B_{11}O_{18}(OH)_9$ (Villars *et al*. 2010) and $(Mn,Fe,Co)^{2+}[BPO_4(OH)_2]$ (Huang *et al*. 2006). Steedeite is the only naturally occurring mineral known to have a $BO_2(OH)_2$ tetahedra however, preliminary structure refinements have demonstrated that the same kind of polyhedron also exists in the unidentified, associated mineral, UK78. The variation observed in the B-(O,OH) bond lengths in steedeite falls within the typical range of 1.462 to 1.512 Å observed in $^{[4]}$B in other borosilicate minerals (Hawthorne *et al*. 1996). Based on radii from Shannon (1976), the ideal B-(O,OH) bond length for tetrahedral B is 1.477 Å (Hawthorne *et al*. 1996) and as the average <B-(O,OH)> bond length of 1.479 Å for steedeite falls within < 1% of this value, the site appears to be only occupied by B (*i.e*., the mineral is strongly ordered with respect to B). In combination with the observed Si-O bond distances, the structural data clearly indicates that Si and B are ordered in steedeite.

The two *Mn* sites are coordinated by five O atoms, and one (OH) group, forming $MnO_5(OH)$ octahedra. These octahedra have Mn-(O,OH) bonds ranging from 2.153(1) to 2.356(1) Å (Table 2-6), similar to Mn-(O,OH) bonds observed in sérandite (Jacobsen *et al*. 2000). The bond-

valence-sums for both Mn sites are close to 2+ (Table 2-7). Furthermore, the average <Mn-(O,OH)> bond lengths are 2.233 and 2.208 Å for the $Mn(1)O_5(OH)$ and $Mn(2)O_5(OH)$ octahedra, respectively. This corresponds to atomic radii of 0.87 and 0.85 Å respectively for Mn(1) and Mn(2) if the ionic radii for O/OH is assumed to be 1.36 Å based on an average O/OH coordination of 3.17 (Shannon 1976). These atomic radii for Mn(1) and Mn(2) are close to the ideal radius of 0.83 Å for Mn^{2+} in [6]-coordination (Shannon 1976) suggesting that Mn in steedeite is largely Mn^{2+}. The *Na* site is coordinated with five O atoms and two (OH) groups, forming $NaO_5(OH)_2$ polyhedra, with Na-(O,OH) bond lengths ranging from 2.342(1) to 2.695(2) Å (<Na-(O,OH)> = 2.481 Å, Table 2-5). Unlike steedeite, the *Na* site in sérandite is coordinated by six O atoms and two (OH) groups, resulting in a $NaO_6(OH)_2$ polyhedron with a slightly larger <Na-(O,OH)> bond length of 2.497 Å (Jacobsen *et al*. 2000).

Each SiO_4 tetrahedron in the crystal structure of steedeite is linked to two adjacent SiO_4 tetrahedra through shared corners forming infinite single silicate chains parallel to *a* (*i.e*. the elongation of steedeite crystals). The silicate chains have a repeat unit consisting of three symmetrically independent SiO_4 tetrahedra: $Si(1)O_4$, $Si(2)O_4$ and $Si(3)O_4$, forming *C*-shaped clusters (Figure 2-3). The *C*-shaped clusters are closed by $BO_2(OH)_2$ tetrahedra via shared corners, generating four-membered $[BSi_3O_{12}]^{7-}$ rings (Figure 2-3). The $BO_2(OH)_2$ tetrahedra are therefore considered to be the branching tetahedra so the silicate chain in steedeite can be classed as a loop-branched *dreier* chain silicate (Liebau 1978). The loop-branched tetrahedral chains are linked through shared corners to double chains of edge-sharing $MnO_5(OH)$ octahedra. The resulting framework contains channels along {011} that are occupied by Na (Figure 2-4). The loop-branched silicate chains and $MnO_5(OH)$ bands form distinct tetrahedral (*T*) and octahedral

(*O*) layers, respectively, resulting in a *T*-*O*-*T*-*O*... stacking along {011} (Figure 2-4). The stacking pattern along with the linkages between the layers of tetrahedra and octahedra give rise to an *I*-beam topology (Thompson 1970) where bands of octahedra are linked to overlying and underlying silicate chains through the apical O atoms in the SiO_4 tetrahedra. In the crystal structure of steedeite, these apical O atoms include O(7), O(5), O(2), and O(1) from the SiO_4 tetahedra as well as OH(11) and OH(10) from the $BO_2(OH)_2$ tetrahedra.

The structure of steedeite contains two (OH) groups, OH(10) and OH(11). The H(1) atoms, bonded to OH(10) groups, project towards adjacent borosilicate chains in the tetrahedral layer (Figure 2-5). Each H(1) atom is located ~ 2.03 Å (Table 2-6) from O(3)-atoms in adjacent borosilicate chains, such that each borosilicate chain within the tetrahedral layer is linked to adjacent chains through hydrogen bonding. The H(2) atoms, bonded to OH(11) groups, project towards borosilicate chains within adjacent tetrahedral sheets (Figure 2-5). Each H(2) atom is located ~ 2.38 Å from O(6)-atoms (Table 2-6) bonded to borosilicate chains such that the tetrahedral layers are linked in part by hydrogen bonds along {011}.

2.9 Related Structures

The *I*-beam topology and the *T*-*O*-*T* stacking pattern present in steedeite is structurally similar to that found in other chain silicate minerals, specifically the pyroxenoids of the pectolite ($NaCa_2[Si_3O_8OH]$)–sérandite ($NaMn_2[Si_3O_8OH]$) series, which are also hydrated and have $P\bar{1}$ symmetry. The crystal structures of these minerals consist of *dreier* silicate chains similar to those in steedeite (Waldemar 1955, Prewitt 1967) but differ in that they are un-branched *dreier* chains, compared to the branched tetrahedral chains in steedeite (Figure 2-4). Although the silicate chains in pectolite–sérandite are unbranched, they contain O...H–O groups (Arakcheeva

et al. 2007) which fulfil the topological role of the $BO_2(OH)_2$ tetrahedra in steedeite. Both steedeite and members of the pectolite–sérandite series contain double chains of edge-sharing octahedra. Steedeite is most closely related to sérandite in terms of its chemistry and crystal structure. Chemically, steedeite has proportions of Na, Mn, and Si identical to those of sérandite, but steedeite also possesses the $BO_2(OH)_2$ group and an additional OH group.

The crystal structure of steedeite is also similar to that of scheuchzerite $\{Na(Mn,Mg)_9[VSi_9O_{28}(OH)](OH)_3\}$; Brugger *et al*. 2006). Both minerals have hydrated loop-branched chain silicate structures but the silicate chains in scheuchzerite are more complex, with a periodicity of seven and six-membered silicate rings that alternate with *C*-shaped silicate clusters similar to those that make up the repeating unit in steedeite (Brugger *et al.* 2006; Figure 2- 4). Each six-membered silicate ring within the silicate chain in scheuchzerite is linked through a shared corner to a single vanadate tetrahedron $(VO_4)^{3-}$ (Brugger *et al*. 2006). The $(VO_4)^{3-}$ group is considered to be a branching tetrahedron, therefore the silicate chain in scheuchzerite can be considered as being both loop-branched and open branched (Liebau 1978). The crystal structures of scheuchzerite and steedeite both contain bands of edge sharing $Mn(O,OH)_6$ octahedra. The bands of $Mn(O,OH)_6$ octahedra in scheuchzerite (Brugger *et al*. 2006) are wider than those in steedeite, with a single octahedral band varying from three to four octahedra wide whereas that in steedeite is only two octahedra wide.

Although the structure of steedeite is closely related to members of the pectolite–sérandite series, the latter have open *dreier* chains while steedeite has loop-branched *dreier* chains (Liebau 1978). Loop-branched *dreier* chains are relatively uncommon and can be found, for example, in charoite $\{(K,Sr,Ba,Mn)_{15\text{-}16}(Ca,Na)_{32}[(Si_{70}(O,OH)_{180})](OH,F)_4 \bullet nH_2O\}$ (Rozhdestvenskaya *et al*. 2010). Here, the loop-branched *dreier* chains link with one another to form tubular *dreier* triple

chains (Rozhdestvenskaya *et al*. 2010). The crystal structure of vlasovite [Na_2Zr (Si_4O_{11})]; Sokolova *et al*. 2006) also contains silicate chains similar to those observed in steedeite with four-membered $[Si_4O_{11}]^{5-}$ rings which are inclined with respect to one another such that the silicate chain has a repeating unit of six instead of three (Sokolova *et al*. 2006, Voronkov & Pyatenko 1962). Unlike steedeite, the crystal structure of vlasovite is a mixed zeolite-like framework where four loop-branched silicate chains are linked through shared corners to ZrO_6 octahedra (Gobechiya *et al*. 2003). There are also two synthetic phases, $Li_2Mg_2[Si_4O_{11}]$ (Maresch & Czank 1985, Czank & Bissert 1993) and $Fe_3Be[Si_3O_9](F,OH)_2$ (Bakakin & Solov'eva 1971), that have single loop-branched *dreier* chains similar to those in steedeite. The crystal structure of $Li_2Mg_2[Si_4O_{11}]$, as in steedeite, has tetrahedral chains consisting of *C*-shaped clusters of three SiO_4 tetrahedra. These *C*-shaped silicate clusters are closed by a fourth SiO_4 tetrahedron instead of a $BO_2(OH)_2$ tetrahedron, generating four-membered $(Si_4O_{11})^{6-}$ rings (Czank & Bissert 1993; Figure 2-4). The silicate chains are linked through shared corners to double chains or bands of edge-sharing MgO_6 octahedra (Czank & Bissert 1993). The crystal structure of $Fe_3Be[Si_3O_9](F,OH)_2$ contains loop-branched *dreier* silicate chains similar to those in steedeite but with BeO_4 tetrahedra instead of $BO_2(OH)_2$ tetrahedra closing the *C*-shaped silicate clusters. The silicate chains in $Fe_3Be[Si_3O_9](F,OH)_2$ are linked through shared corners to triple chains of edge-sharing FeO_6 octahedra.

Four membered borosilicate rings similar to those in steedeite can also be found in the crystal structure of reedmergnerite ($NaBSi_3O_8$; Appleman & Clark 1965) with the latter containing two SiO_4 and two BO_4 tetrahedra. These four-membered rings are linked through shared corners to adjacent rings in three dimensions, generating a framework structure, rather that the chain structure found in steedeite. Given the relationship between steedeite and reedmergnerite, the

silicate chains in steedeite represent a degree of polymerization intermediate between chain silicate structures and framework structures.

2.10 Relationship of Steedeite to Borosilicate Minerals

Similar to silicate minerals, B-bearing minerals may be classified based on the degree of polymerization observed in B(O,OH) polyhedra. Hawthorne (1983) proposed a classification scheme based on the polymerization of polyhedra with high bond valences (*i.e.*, borate polyhedra and silicate tetrahedra). In this classification scheme possible polyhedral clusters include: 1) unconnected polyhedra, 2) finite clusters, 3) infinite chains, 4) infinite sheets and 5) infinite frameworks (Hawthorne 1983). From the perspective of borate polyhedra, borosilicate minerals may be classified as those with crystal structures based on unconnected borate polyhedra (*e.g.*, ferroaxinite, tourmaline, and reedmergnerite) or those with crystal structures based on finite clusters of borate polyhedra (*e.g.*, tadzhikite, hellandite, danburite, and howlite; Hawthorne *et al*. 1996). In this case, the crystal structure of steedeite is based on unconnected BO_4 tetrahedra similar to that of reedmergnerite and ferroaxinite.

There are ~ 100 known borosilicate minerals (excluding the tourmaline group) of which ~ 10 are known to be disordered with respect to Si and B. Since it is clear that the majority of borosilicates show a strong preference for Si-B ordering, it is perhaps not suprising that steedeite does as well. In Si-B ordering experiments conducted on reedmergnerite in the *T* range of 400–500 °C, results indicated that those of longer duration (*i.e.*, >200 hours) promoted higher degrees of Si-B ordering (Mason 1980). This suggests that steedeite crystals, which show a high degree of Si-B ordering, could have cooled over a protracted period of time. The experiments of Mason

(1980) also showed Si-B disordered phases were found to be unstable relative to the Si-B ordered phases, the former exhibiting etching features which are evidence of dissolution (Mason 1980). The relative stability of Si-B ordered phases over Si-B disordered phases could thus explain the paucity of disordered borosilicates.

2.11 Origin

Paragenetically, steedeite along with sérandite, UK78, UK80, and thermonatrite are late-stage phases which overgrow earlier-formed phases such as microcline, aegirine and analcime (Table 2-8). Thermonatrite is inferred to have been the latest crystallizing phase as it overgrows crystals of steedeite. The sequence of formation for steedeite, sérandite, UK78, and UK80 is unclear (Table 2-8) as none of these phases have been found together in the same vug.

The hydrous structure of steedeite and its occurrence in vugs suggests that it precipitated from late-stage aqueous fluids. These fluids are inferred to have been highly alkaline due to the presence of late-stage natrite (Table 2-8). Experimental studies showed that the maximum stability of the latter mineral is in the pH range of ~ 8 to 10 (Marion 2001). Based on fluid inclusion data as well as carbonate-carbonate and carbonate-silicate equilibria, the temperatures of late-stage fluids at Mont Saint-Hilaire are inferred to have been < 400 °C (Schilling *et al*. 2011). The common occurrence of steedeite and the unidentified minerals UK78 and UK80 in vugs of the same xenolith, suggests that these minerals precipitated from similar late-stage aqueous fluids. The presence of late-stage sérandite (Table 2-8) in the same sample as steedeite also suggests that the former mineral formed through precipitation from aqueous late-stage fluids. Both minerals occur in the same sodalite syenite boulder but observations indicate that they are never found in the same vug together. This suggests that the aqueous fluid had localized

variations in $a[SiO_4]^{4-}$ as well as $aB(OH)_3$ and $a[B(OH)_4]^-$ where a decrease in $a[SiO_4]^{4-}$ and an increase in $aB(OH)_3$ and $a[B(OH)_4]^-$ favoured the development of steedeite over sérandite. A preliminary structure refinement of UK78 indicates that it also contains B indicating that both UK78 and steedeite precipitated from similar fluids. Due to the possible variations in aBO_3 in the late-stage fluids, it is unclear whether or not the crystal structure of UK80 also contains B.

Another indication for the low-T formation of steedeite may be the conditions at which minerals of the sérandite–pectolite series form. Pectolite has been synthesized over two to three days under hydrothermal conditions with temperatures in the range of 180 °C to 300 °C with Ca:Si molar ratios of 0.83. (Clark & Bunn 1940, Blakeman *et al*. 1974, Xi & Glasser 1984). Given the existence of late-stage sérandite in the same boulder wherein steedeite is found implies that steedeite likely formed under a similar range in *T*. It is noteworthy that steedeite represents the first mineral known to contain single looped-branched dreier silicate chains suggesting that such structures have limited pressure/temperature ranges. Phase stability experiments completed on $Li_2Mg_2[Si_4O_{11}]$ indicate that this phase is stable over a small pressure/temperature range: T ~ 700–900 °C and $P(H_2O)$ ~ 0–2 kbar (Vitek & Maresch 1993). It is possible that steedeite, like $Li_2Mg_2[Si_4O_{11}]$, also develops over a narrow pressure and temperature range. Studies of fluid inclusion as well as associated minerals however, indicate that steedeite likely forms at temperatures lower than $Li_2Mg_2[Si_4O_{11}]$.

2.12 References

Amthauer, G. & Rossman, G.R. (1984): Mixed valence of iron in minerals with cation clusters. Physics and Chemistry of Minerals, 11, 37-51.

Appleman, D.E. & Clark, J.R. (1965): Crystal structure of reedmergnerite, a boron albite, and its relationship to feldspar crystal chemistry. American Mineralogist, 50, 1827-1850.

Arakcheeva, A., Pattison, P., Meisser, N., Chapuis, G., Pekov, I., & Thélin, P. (2007): New insight into the pectolite – sérandite series: a single crystal diffraction study of $Na(Ca_{1.73}Mn_{0.27})[HSi_3O_9]$ at 293 and 100 K. Zeitschrift für Kristallographie, 222, 696-704.

Bakakin, V.V. & Solo'eva, L.P. (1971): Crystal structure of $Fe_3BeSi_3O_9(F,OH)_2$, an example of a wollastonite-like silicon-oxygen chain based on Fe. Soviet Physics Crystallography, 15, 999-1005.

Blakeman, E.A., Gard, J.A., Ramsay, C.G. & Taylor, H.F.W. (1974): Studies on the system sodium oxide - calcium oxide - silica - water. Journal of Chemical Technology and Biotechnology, 24, 239-245.

Brese, N.E. & O'keefe, M. (1991): Bond-valence parameters for solids. Acta Crystallographica, B47, 192-197.

Brown, I.D. & Altermatt, D. (1985): Bond-valence parameters obtained from a systematic analysis of the inorganic crystal structure database. Acta Crystallographica, B41, 244-247.

Brugger, J., Krivivichev, S., Meisser, N., Ansermet, S., & Armbruster, T. (2006): Scheuchzerite, $Na(Mn,Mg)_9[VSi_9O_{28}(OH)](OH)_3$, a new single-chain silicate. American Mineralogist, 91, 937-943.

Clark, L.M. & Bunn, C.W. (1940): The scaling of boilers. Pt. IV. Identification of of phases in calcium silicate scales. Journal of the Society of Chemical Industry, 59, 155-158.

Cromer, D.T. & Liberman, D. (1970): Relativistic calculation of anomalous scattering factors for X rays. Journal of Physical Chemistry, 53, 1891-1898.

Cromer, D.T. & Mann, J.B. (1968): X-ray scattering factors computed from numerical Hartree-Frock wave functions. Acta Crystallographica, A24, 321-324. ces, 44: 1333-1346.

Czank, M. & Bissert, G. (1993): The crystal structure of $Li_2Mg_2[Si_4O_{11}]$, a loop-branched dreier single chain silicate. Zeitschrift für Kristallographie, 204, 129-142.

Dowty, E. (2002): CRYSCON for Windows and Macintosh Version 1.1. Shape Software Kingsport, Tennessee, USA.

Frost, R.L., Bouzaid, J.M., Martens, W.N. & Reddy, J.B. (2007): Raman spectroscopy of the borosilicate mineral ferroaxinite. Journal of Raman Spectroscopy, 38, 135-141.

Gobechiya, E.R., Pekov, I.V., Pushcharovskiĭ, D.Y., Ferraris, G., Gula, A., Zubkova, N.V. & Chukanov, N.V. (2003): New data on vlasovite: Refinement of the crystal structure and radiation damage of the crystal during the X-ray diffraction experiment. Crystallography Reports, 48, 750-754.

Hawthorne, F.C. (1983): Enumeration of polyhedral clusters. Acta Crystallographica, A39, 724-736.

Hawthorne, F.C., Burns, P.C. & Grice, J.D. (1996): The crystal chemistry of boron. Reviews in Mineralogy, 33, 41-110.

Huang, Y.X., Ewald, B., Schnelle, W., Prots, Y. & Kniep, R. (2006): Chirality and magnetism in a novel series of isotypic borophosphates: $M^{II}[BO_4(OH)_2]$ (M^{II} = Mn, Fe, Co). Inorganic Chemistry Communication, 45, 7578-7580.

Hybler, J., Petricek, V., Jurek, K., Skala, R. & Cisarova, I. (1997): Structure determination of vistepite $SnMn_4B_2Si_4O_{16}(OH)_2$: Isotypism with bustamite, revised crystallographic data and composition. Canadian Mineralogist, 35, 1283-1292.

Jacobsen, S.D., Smyth, J.R., Swope, J.R., & Sheldon, R.I. (2000): Two proton positions in the very strong hydrogen bond of sérandite, $NaMn_2[Si_3O_8(OH)]$. American Mineralogist, 85, 745-752.

Julien, C.M., Massot, M., & Poinsignon, C. (2004): Lattice vibrations of manganese oxides: Part 1. Periodic structures. Spectrochimica Acta Part A, 60, 689-700.

Khomyakov, A.P. (1995): Mineralogy of hyperagpaitic alkaline rocks. Oxford Scientific Publications. Claredon Press. pp 108-109.

Liebau, F. (1978): Silicates with branched anions: a crystallochemically distinct class. American Mineralogist, 63, 918-923.

Maresch, W.V. & CzankZ, M. (1985): The optical and X-ray properties of $Li_2Mg_2[Si_4O_{11}]$, a new type of chain-silicate. Neues Jahrbuch für Mineralogie, 7, 289-297.

Marion, G.M. (2001): Carbonate mineral solubility at low temperatures in the Na-K-Mg-Ca-H-Cl-SO_4-OH-HCO_3-CO_3-CO_2-H_2O system. Geochimica et Cosmochimica Acta, 65, 1883-1896.

Mason, R. A. (1980): Changes in crystal morphology of synthetic reedmergnerite ($NaBSi_3O_8$) during ordering experiments. Mineralogical Magazine, 43, 905-908.

McDonald, A.M. & Chao, G.Y.(2005): Bobtraillite, $(Na,Ca)_{13}Sr_{11}(Zr,Y,Nb)_{14}Si_{42}B_6O_{132}(OH)_{12}\bullet 12H_2O$ a new mineral species from Mont Saint-Hilaire, Québec: description, structure determination and relationship to benitoite and wadeite. Canadian Mineralogist, 43, 747-758.

McDonald, A.M. & Chao, G.Y. (2009): Lalondeite, a new hydrated Na-Ca fluorosilicate species from Mon Saint-Hilaire, Québec: Description and crystal structure. Canadian Mineralogist, 47, 181-191.

McDonald, A.M. & Chao, G.Y. (2010): Rogermitchellite, $Na_{12}(Sr,Na)_{24}Ba_4Zr_{26}Si_{78}(B,Si)_{12}O_{246}(OH)_{24}\bullet 18H_2O$, a new mineral species from Mon Saint-Hilaire, Québec: description, structure determination and relationship with HFSE-bearing cyclosilicates. Canadian Mineralogist, 48, 267-278.

Mustard, J.F. (1992): Chemical analysis of actinolite from reflectance spectra. American Mineralogist, 77, 345-358.

Nagase, T., Hori, H., Kitamine, M., Nagashima, M., Abduriyim, A. & Kuribayashi, T. (2012): Tanohataite, $LiMn_2Si_3O_8(OH)$: a new mineral from the Tanohata mine, Iwate Prefecture, Japan. Journal Mineralogical and Petrological Science, 107, 149-154.

Pekov, I.V. (2000): Lovozero Massid: History, pegmatites, minerals. Ocean Pictures Ltd. pp 387.

Prewitt, C.T. (1967): Refinement of the crystal structure of pectolite, $Ca_2NaHSi_3O_9$. Zeitschrift für Kristallographie, 125, 298-316.

Rozhdestvenskaya, I., Mugnaioli, E., Czank, M., Depmeier, W., Kolb, U., Reinholdt, A., & Weirich, T.(2010): The structure of charoite, $(K,Sr,Ba,Mn)_{15-16}(Ca,Na)_{32}[(Si_{70}(O,OH)_{180})](OH,F)_{4.0}\bullet nH_2O$, solved by conventional and automated electron diffraction. Mineralogical Magazine, 74, 159-177.

Schilling, J., Marks, M.A.W., Wenzel, T., Vennemann, T., Horvath, L., Tarassoff, P., Jacob, D.E., & Markl, G. (2011): Magmatic to hydrothermal evolution of the intrusive Mont Saint-Hilaire complex: insights into the late-stage evolution of peralkaline rocks. Journal of Petrology, 52, 2147-2185.

Shannon, R.D. (1976): Revised effective ionic radii and systematic studies in interatomic distances in halides and chalogenides. Acta Crystallographica, A32, 751-767.

Sheldrick, G.M. (1997): SHELXL-97: A computer program for the Refinement of Crystal Structures. Univ. of Göttingen, Göttingen, Germany.

Sokolova, E., Hawthorne, F.C., Ball, N.A. & Mitchell, R.H. (2006): Vlasovite, $Na_2Zr(Si_4O_{11})$, from the Kipawa alkaline complex, Québec, Canada: crystal-structure refinement and infrared spectroscopy. Canadian Mineralogist, 44, 1349-1356.

Thompson, J.B. (1970): Geometrical possibilities for amphibole structures: Model biopyriboles. American Mineralogist, 63, 239-249.

Villars, P., Cenzual, K., Daams, J., Gladyshevskii, R., Shcherban, O., Dubenskyy, V., Kuprysyuk, V. & Savysyuk, I. (2010): $Pb_6B_{11}O_{18}(OH)_9$. Crystal Structures of Inorganic Compounds, 43A9, 501-502.

Vitek, E., & Maresch, W.V. (1993): Synthesis and stability regions of $Li_2Mg_2[Si_4O_{11}]$. European Journal of Mineralogy, 5, 1121-1131.

Voronkov, A.A. & Pyatenko, Y.A. (1962): The crystal structure of vlasovite. Soviet Physics Crystallography, 6, 755-760.

Waldemar T.S. (1955): The pectolite-serandite series. American Mineralogist. 40, 1022-1031.

Williams, Q. (1995): Infrared, Raman and optical spectroscopy of Earth materials. American Geophysical Union, 291- 302.

Xi, Y. & Glasser L.S.D. (1984): Hydrothermal study in the system Na2O-CaO-SiO2-H2O at 300 degrees celcius. Cement Concrete Research, 14, 741-748.

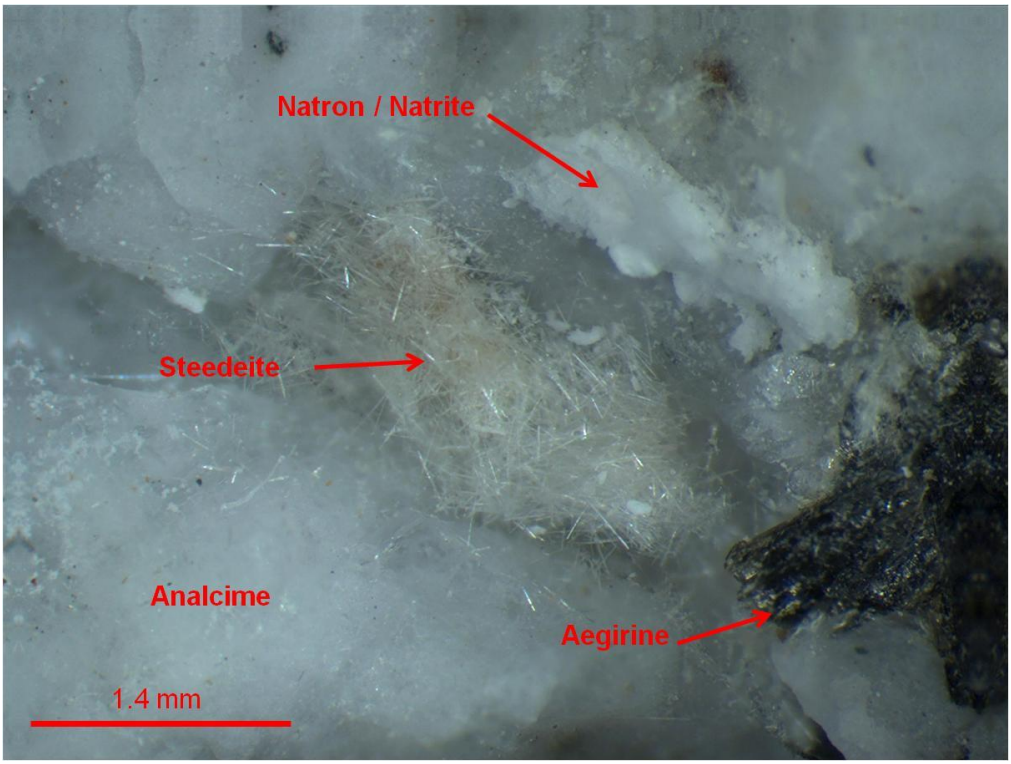

Figure 2-1. Loose aggregates of steedeite with natron, aegirine, and analcime (FOV: 1.0 mm)

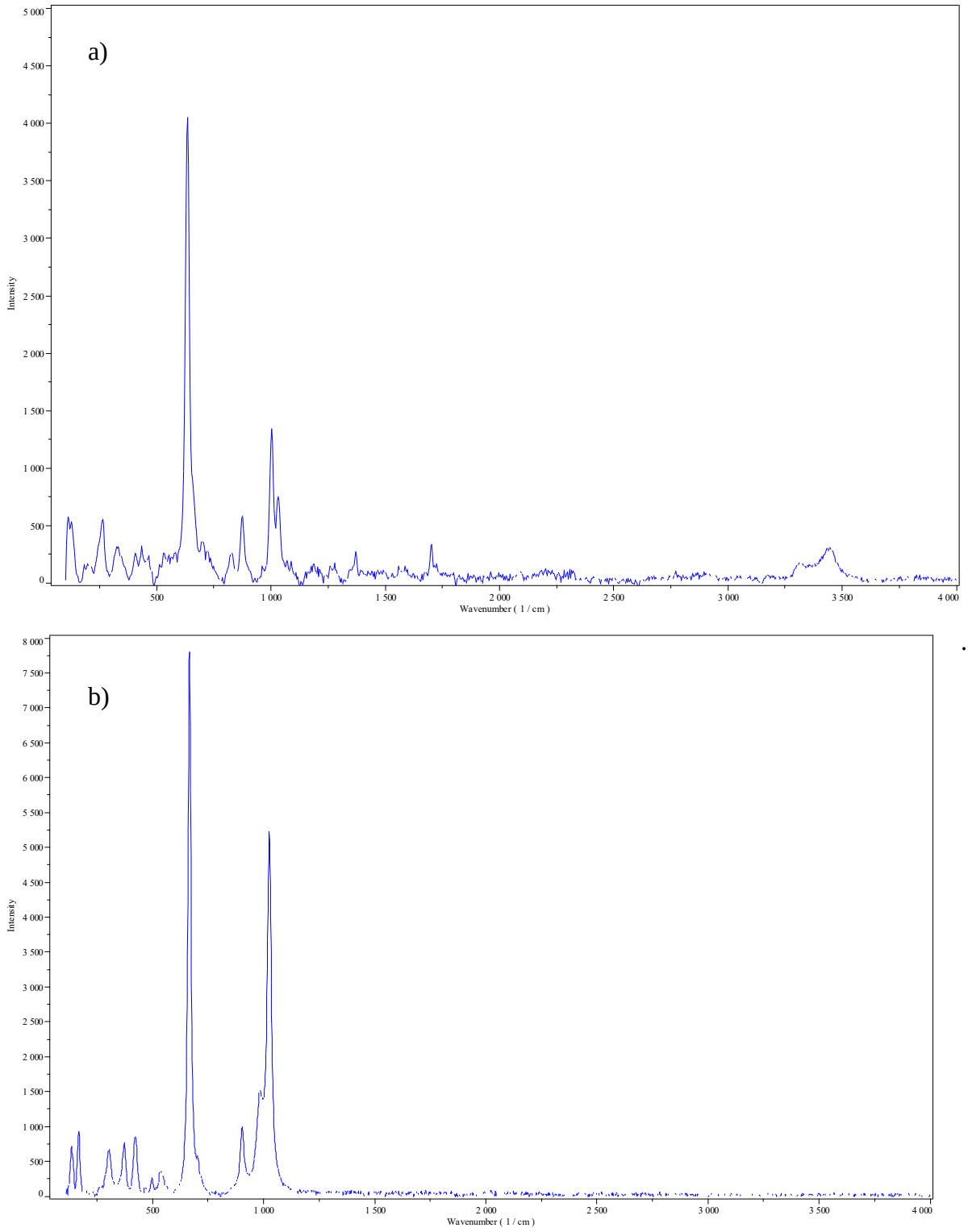

Figure 2-2. Raman spectrum for a) steedeite and b) sérandite

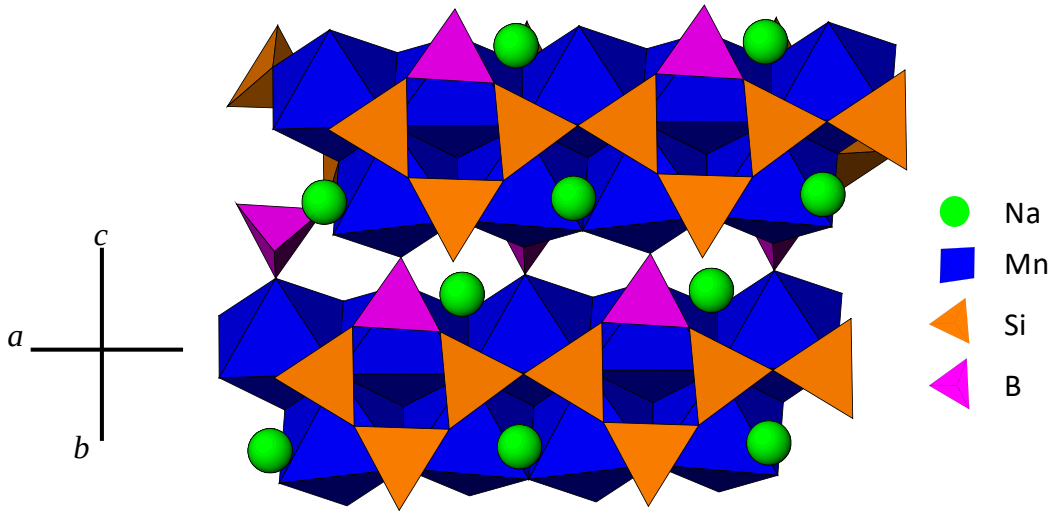

Figure 2-3. The crystal structure of steedeite projected on to [011]. Both the bands of MnO5(OH) and the loop-branched dreier chains run parallel to *a*. The sodium atoms are in green, SiO_4 tetrahedra are orange, $BO_2(OH)_2$ tetrahedra are pink, and the $MnO_5(OH)$ octahedra are blue.

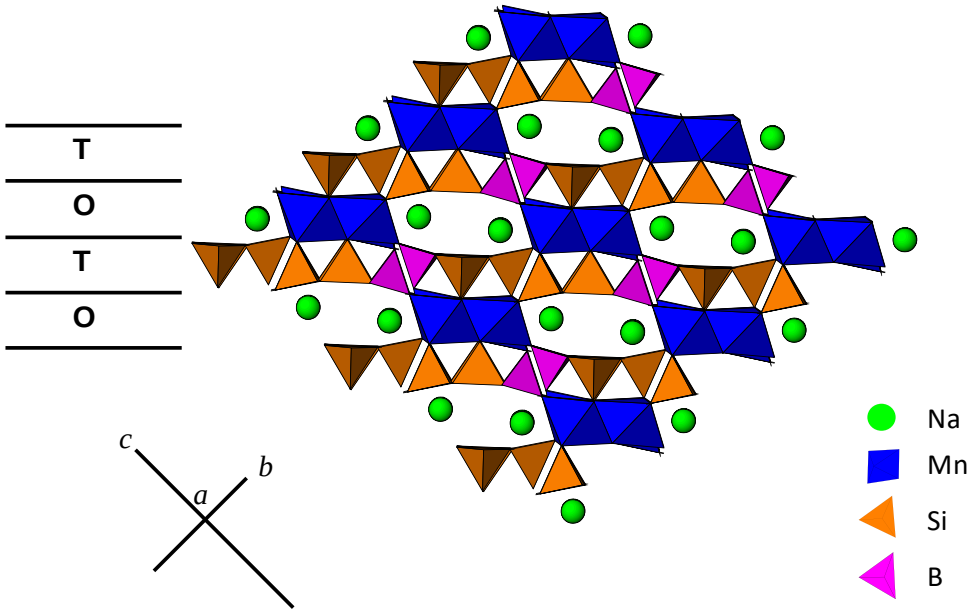

Figure 2-4. The crystal structure of steedeite, projected on to [100], with tetrahedral (T) and octahedral (O) layers alternating along [011]. The sodium atoms are in green, SiO_4 tetrahedra are orange, $BO_2(OH)_2$ tetrahedra are pink, and the $MnO_5(OH)$ octahedra are blue.

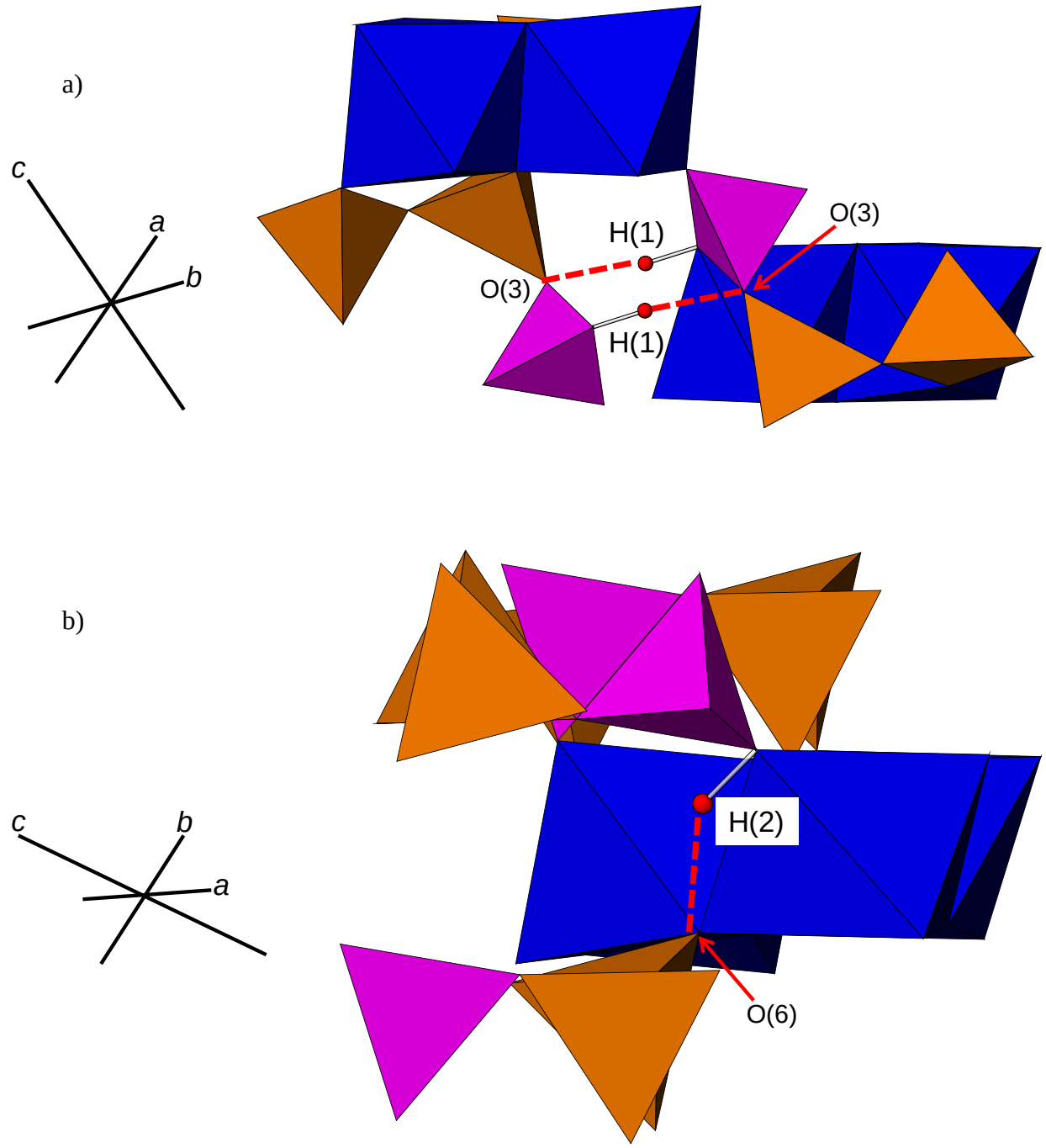

Figure 2-5. Hydrogen bonding environments for a) H(1) atoms and b) H(2) atoms.

Table 2-1. Description and modal abundances of minerals occurring with steedeite.

Mineral	Modal Abundance	Description
Microcline ($KAlSi_3O_8$)	~ 68 %	Aggregates of anhedral light grey crystals with a massive habit and greasy lustre.
Analcime $Na_2(Al_2Si_4O_{12})\bullet 2H_2O$	~ 10 %	Anhedral to subhedral translucent to transparent crystals with a vitreous lustre.
Nepheline $(Na,K)AlSiO_4$	~ 7 %	Anhedral, greenish-grey crystals with a greasy lustre.
Aegirine $NaFe^{3+}Si_2O_6$	~5 %	Dark green, prismatic, euhedral crystals ranging in size from ~ 0.1 to 0.7 mm in length and dominated by the form prism {110}.
Pyrrhotite $Fe_{1-x}S$	~ 5 %	Pseudohexagonal crystals, ~ 4 mm in diameter, displaying the forms pinacoid {001}, pinacoid {100}, prism {100}, and prism {*h*0*l*}.
Sodalite $Na_8(Al_6Si_6O_{24})Cl_2$	~ 2 %	Anhedral, transparent crystals with a pale blue to violet colour and a strong fluoresence under short-, medium-, and long-wave radiation.
Eudialyte-group mineral $Na_{15}Ca_6(Fe^{2+}, Mn^{2+})_3Zr_3[Si_{25}O_{73}](O,OH,H_2O)_3(OH,Cl)_2$	~ 1 %	Euhedral, translucent to transparent crystals with a dark brown to orange colour.
Sérandite $Na(Mn^{2+},Ca)_2Si_3O_8(OH)$	~ 1 %	Radiating spheres composed of prismatic crystals with flattened terminations (pinacoid {001}). These crystals range in colour from dark to pale green and brown to light brown.

Thermonatrite $Na_2CO_3 \bullet H_2O$	~ 1 %	White anhedral to subhedral, translucent crystals.
Catapleiite $(Na,Ca,\square)_2ZrSi_3O_9.2H_2O$	trace	Clear, colourless, pseudo hexagonal plates overgrowing sérandite.
UK78	trace	Clusters of radiating to randomly oriented, acicular, light green crystals with dimensions similar to those of steedeite.
UK80	trace	Flat clusters of radiating, brown crystals with dimensions similar to those of steedeite.

Table 2-2. Observed absorption bands and band assignments for the Raman spectrum of steedeite.

Raman Absorption Bands for steedeite (cm^{-1})	Raman Absorption Bands for sérandite (cm^{-1})	Suggested Assignment
3443		O-H Stretching
3317		O-H Stretching
1700		Unassigned
1368		Unassigned
1030	1026	Asymmetric stretching mode of Si-O_{nbr}/ B-O stretching
1000		Asymmetric stretching mode of Si-O_{nbr}/ B-O stretching
	984	Asymmetric stretching mode of Si-O_{nbr}/ B-O stretching
	903	Asymmetric stretching mode of Si-O_{nbr}/ B-O stretching
874		Symmetric stretching mode of Si-O_{br}
826		Symmetric stretching mode of Si-O_{br}
696	703	Si-O-Si and Si-O-B Bending/ Mn-O
	666	Si-O-Si and Si-O-B Bending/ Mn-O
636		Si-O-Si and Si-O-B Bending/ Mn-O
	535	Si-O-Si and Si-O-B Bending/ Mn-O
	497	Si-O-Si and Si-O-B Bending/ Mn-O
	466	Si-O-Si and Si-O-B Bending/ Mn-O
431	422	Si-O-Si and Si-O-B Bending/ Mn-O
	373	Si-O-Si and Si-O-B Bending/ Mn-O
330		Si-O-Si Bending/ O-Si-O Bending/ Mn-O
	304	Mn-O
264		Mn-O
197		Mn-O
	168	Mn-O/ Na-O
	134	Mn-O/ Na-O
120		Na-O

Table 2-3. Steedeite X-ray Powder Diffraction Data.

I_{meas}	I_{calc}	d_{meas} Å	d_{calc} Å	*h*	*k*	*l*
100	**100**	**8.454**	**8.411**	**0**	**0**	**-1**
39	**30**	**7.234**	**7.190**	**0**	**-1**	**0**
18	13	6.243	6.215	0	-1	1
8	3	4.240	4.264	1	1	0
	4		4.205	0	0	-2
6	6	4.083	4.059	0	-1	2
19	2	3.619	3.620	0	-2	1
	10		3.599	1	1	-2
83	**9**	**3.331**	**3.392**	**1**	**-2**	**1**
	52		**3.314**	**0**	**-1**	**-2**
	2		**3.307**	**2**	**0**	**-1**
	17		**3.289**	**1**	**-1**	**2**
38	**25**	**3.081**	**3.062**	**0**	**-2**	**-1**
11	9	2.979	2.962	1	2	-1
52	**27**	**2.859**	**2.842**	**0**	**-1**	**3**
80	**71**	**2.823**	**2.814**	**2**	**1**	**-1**
18	14	2.525	2.508	0	-2	3
21	13	2.477	2.459	0	-3	1
8	9	2.336	2.324	0	-3	2
12	11	2.248	2.237	2	2	-1
	10		2.229	2	-3	0
25	17	2.169	2.156	0	-1	4
4	7	2.118	2.103	0	0	-4
2	2	2.083	2.072	0	-3	3
6	5	1.948	1.943	2	-3	-2
5	3	1.913	1.915	2	-1	-4
3	3	1.729	1.720	2	-2	4
7	20	1.691	1.709	4	-1	-1
6	6	1.598	1.596	2	-4	-2
4	1	1.482	1.488	4	1	0
	2		1.481	2	4	-2

Table 2-4. Miscellaneous single crystal data for steedeite.

a (Å)	6.837(1)	Monochromator	Graphite
b	7.575(2)	Intensity-data collection	θ:2θ
c	8.841(2)	Criterion for observed	
α (°)	99.91(3)	reflections	$F_o > 4\sigma(F_o)$
β	102.19(3)	GoOF	0.953
γ	102.78(3)	total No. of reflections	15061
V (Å^3)	424.81(1)	No. Unique reflections	2487
Space group	$P\bar{1}$ (#2)	R (merge %)	1.71
Z	2	R %	1.68
D_{calc} (g/cm^{-3})	3.106	wR^2 %	4.96
Radiation	MoKα (50 kV, 40 mA)		

Table 2-5. Positional and displacement parameters for steedeite.

ATOM	*x*	*y*	*z*	U_{eq}	U_{11}	U_{22}	U_{33}	U_{23}	U_{13}	U_{12}
Na	-0.1247	0.64118	0.81008	0.0199	0.0315	0.0176	0.0158	0.0050	0.0101	0.0123
	0.0001	0.00009	0.00007	0.0001	0.0003	0.0003	0.0003	0.0002	0.0003	0.0003
Mn1	0.12800	0.87518	0.60727	0.00946	0.0091	0.0101	0.0085	0.00136	0.00180	0.00222
	0.00003	0.00003	0.00002	0.00006	0.0001	0.0001	0.0001	0.00007	0.00007	0.00007
Mn2	-0.38639	0.86495	0.59872	0.01037	0.0100	0.0098	0.0104	0.00088	0.00130	0.00331
	0.00003	0.00003	0.00002	0.00006	0.0001	0.0001	0.0001	0.00007	0.00007	0.00007
Si1	-0.27055	0.52647	0.38313	0.0076	0.0076	0.0062	0.0083	0.0008	0.0018	0.0016
	0.00005	0.00005	0.00004	0.0001	0.0002	0.0002	0.0002	0.0001	0.0001	0.0001
Si2	-0.53952	0.74187	0.21311	0.0080	0.0062	0.0078	0.0090	0.0001	0.0012	0.0018
	0.00005	0.00005	0.00004	0.0001	0.0002	0.0002	0.0002	0.0001	0.0001	0.0001
Si3	0.01582	0.73835	0.22546	0.0071	0.0065	0.0076	0.0066	0.0007	0.0015	0.0018
	0.00005	0.00005	0.00004	0.0001	0.0002	0.0002	0.0002	0.0001	0.0001	0.0001
B	-0.2798	0.8757	0.0291	0.0057	0.0043	0.0074	0.0046	-0.0011	0.0008	0.0020
	0.0002	0.0002	0.0002	0.0002	0.0005	0.0005	0.0005	0.0004	0.0004	0.0004
O1	0.4415	1.0798	0.6388	0.0101	0.0103	0.0086	0.0095	0.0000	0.0012	0.0017
	0.0001	0.0001	0.0001	0.0002	0.0004	0.0004	0.0004	0.0003	0.0003	0.0003
O2	-0.1887	0.6853	0.5474	0.0104	0.0110	0.0090	0.0099	0.0003	0.0023	0.0021
	0.0002	0.0001	0.0001	0.0002	0.0004	0.0004	0.0004	0.0003	0.0003	0.0003
O3	-0.4806	0.7830	0.0524	0.0140	0.0111	0.0160	0.0128	-0.0005	0.0053	0.0004
	0.0002	0.0001	0.0001	0.0002	0.0004	0.0005	0.0004	0.0003	0.0003	0.0003

O4	0.0839	0.9205	0.3686	0.0101	0.0119	0.0088	0.0085	0.0002	0.0021	0.0022
	0.0002	0.0001	0.0001	0.0002	0.0004	0.0004	0.0004	0.0003	0.0003	0.0003
O5	-0.1274	0.7708	0.0698	0.0135	0.0144	0.0162	0.0097	0.0009	-0.0005	0.0087
	0.0002	0.0001	0.0001	0.0002	0.0004	0.0004	0.0004	0.0003	0.0003	0.0004
O6	0.3217	0.6841	0.5976	0.0110	0.0100	0.0080	0.0155	0.0034	0.0042	0.0021
	0.0001	0.0001	0.0001	0.0002	0.0004	0.0004	0.0004	0.0003	0.0003	0.0003
O7	-0.0939	0.5540	0.2805	0.0117	0.0133	0.0095	0.0136	0.0028	0.0072	0.0022
	0.0002	0.0001	0.0001	0.0002	0.0004	0.0004	0.0004	0.0003	0.0003	0.0003
O8	-0.7925	0.6785	0.1678	0.0109	0.0067	0.0125	0.0124	0.0000	0.0024	0.0028
	0.0001	0.0001	0.0001	0.0002	0.0004	0.0004	0.0004	0.0003	0.0003	0.0003
O9	-0.4764	0.5622	0.2688	0.0133	0.0116	0.0095	0.0161	0.0011	-0.0022	0.0041
	0.0002	0.0001	0.0001	0.0002	0.0004	0.0004	0.0004	0.0003	0.0003	0.0003
OH10	0.1985	0.9290	0.8689	0.0127	0.0134	0.0118	0.0123	0.0021	0.0020	0.0037
	0.0002	0.0001	0.0001	0.0002	0.0004	0.0004	0.0004	0.0003	0.0003	0.0003
OH11	-0.3053	0.8805	0.8609	0.0244	0.0424	0.0320	0.0092	0.0084	0.0091	0.0259
	0.0002	0.0002	0.0001	0.0003	0.0007	0.0006	0.0004	0.0004	0.0005	0.0006
H1	0.287	0.855	0.914	0.053						
	0.003	0.003	0.003	0.008						
H2	-0.417	0.766	0.84	0.39						
	0.009	0.007	0.01	0.06						

Table 2-6. Interatomic distances (Å) in steedeite.

Na$O_6(OH)_2$ Polyhedron			*Si*(1)O_4 Tetrahedron		
Na	-O5	2.342(1)	*Si*1	-O6	1.602(1)
	-O2	2.367(1)		-O2	1.621(1)
	-O8	2.414(1)		-O9	1.654(1)
	-OH11	2.441(1)		-O7	1.657(1)
	-O7	2.477(1)	<*Si*1	-O>	1.634
	-OH10	2.627(2)			
	-O9	2.695(2)	*Si*(2)O_4 Tetrahedron		
<*Na*	-O>	2.481	*Si*2	-O1	1.615(1)
				-O3	1.618(1)
Mn(1)O_5(OH) Octahedron				-O8	1.630(1)
*Mn*1	-O4	2.165(1)		-O9	1.638(1)
	-O6	2.171(1)	<*Si*2	-O>	1.625
	-OH10	2.205(1)			
	-O2	2.216(1)	*Si*(3)O_4 Tetrahedron		
	-O1	2.281(1)	*Si*3	-O5	1.602(1)
	-O4	2.356(1)		-O4	1.608(1)
<*Mn*1	-O>	2.233		-O8	1.627(1)
				-O7	1.635(1)
Mn(2)O_5(OH) Octahedron			<*Si*3	-O>	1.618
*Mn*2	-O6	2.153(1)			
	-O2	2.178(1)	*B*$O_2(OH)_2$ Tetrahedron		
	-O1	2.183(1)	*B*	-O5	1.468(2)
	-O1	2.233(1)		-O3	1.470(2)
	-OH11	2.243(1)		-OH11	1.467(2)
	-O4	2.259(1)		-OH10	1.508(2)
<*Mn*2	-O>	2.208	<*B*	-O>	1.479

Hydrogen Bonding

Donor-H	*d*(D-H; Å)	*d*(H..A; Å)	<DHA (°)	*d*(D..A; Å)	Acceptor
OH10-H1	0.980	2.029	161.83	2.976	O3
OH11-H2	0.987	2.384	116.51	2.960	O6

Table 2-7. Bond-valence table (*v.u.*) for steedeite.

	Na	Mn(1)	Mn(2)	Si(1)	Si(2)	Si(3)	B	∑	H(1)	H(2)	Σ
O1		$0.265^{\downarrow\rightarrow}$	$0.648^{\downarrow\rightarrow}$		$1.025^{\downarrow\rightarrow}$			1.938			1.938
O2	$0.216^{\downarrow\rightarrow}$	$0.316^{\downarrow\rightarrow}$	$0.350^{\downarrow\rightarrow}$	$1.008^{\downarrow\rightarrow}$				1.890			1.890
O3					$1.016^{\downarrow\rightarrow}$		$0.765^{\downarrow\rightarrow}$	1.781	$0.12^{\downarrow\rightarrow}$		1.901
O4		$0.580^{\downarrow\rightarrow}$	$0.282^{\downarrow\rightarrow}$			$1.044^{\downarrow\rightarrow}$		1.906			1.906
O5	$0.231^{\downarrow\rightarrow}$					$1.061^{\downarrow\rightarrow}$	$0.769^{\downarrow\rightarrow}$	2.061			2.061
O6		$0.357^{\downarrow\rightarrow}$	$0.375^{\downarrow\rightarrow}$	$1.061^{\downarrow\rightarrow}$				1.793		$0.08^{\downarrow\rightarrow}$	1.873
O7	$0.160^{\downarrow\rightarrow}$			$0.915^{\downarrow\rightarrow}$		$0.971^{\downarrow\rightarrow}$		2.046			2.046
O8	$0.190^{\downarrow\rightarrow}$				$0.984^{\downarrow\rightarrow}$	$0.992^{\downarrow\rightarrow}$		2.166			2.166
O9	$0.089^{\downarrow\rightarrow}$			$0.922^{\downarrow\rightarrow}$	$0.963^{\downarrow\rightarrow}$			1.974			1.974
OH10	$0.107^{\downarrow\rightarrow}$	$0.326^{\downarrow\rightarrow}$					$0.691^{\downarrow\rightarrow}$	1.124	$0.88^{\downarrow\rightarrow}$		2.004
OH11	$0.177^{\downarrow\rightarrow}$		$0.294^{\downarrow\rightarrow}$				$0.771^{\downarrow\rightarrow}$	1.242		$0.92^{\downarrow\rightarrow}$	2.162
Σ	1.170	1.844	1.949	3.906	3.988	4.068	2.996		1.00	1.00	

* Bond valences for H sites determined using parameters from Brown and Altermatt (1985). Bond valences for other sites determined using parameters from Brese and O'Keeffe (1991).

Table 2-8. Mineral paragenesis.

Mineral	Timing
Microcline	
Aegirine	
Eudialyte	
Analcime	
Sodalite	
Pyrrhotite	
Serandite	
Steedeite	
UK78	
UK80	
Catapleiite	
Natrite/Thermonatrite	

Chapter 3

Nolzeite, $Na(Mn,\square)_2[Si_3(B,Si)O_9(OH)_2]\bullet 2H_2O$, a new pyroxenoid mineral from Mont Saint-Hilaire, Quebec, Canada

3.1 Abstract

Nolzeite, $Na(Mn,\square)_2[Si3(B,Si)O_9(OH)_2]\bullet 2H_2O$, is a new mineral found in altered sodalite syenite at the Poudrette quarry, La Vallée-du-Richelieu, Montérégie (formerly Rouville County), Québec, Canada. Crystals are colourless to pale green and are acicular with average dimensions of 5 x 8 x 55 μm. They occur as radiating to loose, randomly oriented groupings within vugs associated with aegirine, nepheline, sodalite, eudialyte-group minerals, analcime, natron, pyrrhotite, catapleiite, steedeite and the unidentified mineral, UK80. Nolzeite is non-pleochroic, biaxial, with n_{min} = 1.616(2) and n_{max} = 1.636(2) and has a positive elongation. The average of six chemical analyses gives the empirical formula:

$Na_{1.04}(Mn_{1.69}\square_{0.24}Fe_{0.05}Ca_{0.02})_{\Sigma=2.00}(Si_{2.96}S_{0.04})_{\Sigma=3.00}(B_{0.70}Si_{0.30})_{\Sigma=1.00}O_9(OH)_2\bullet 2H_2O$ based on 13 anions. The Raman spectrum shows six distinct bands occurring at ~ 3600 – 3300 cm^{-1} and 1600 – 1500 cm^{-1} (O-H and H-O-H bending),1300 – 1200 cm^{-1} (B-OH bending), 1030 – 800 cm^{-1} (Si-O-Si stretching) as well as 700 – 500 cm^{-1} and 400 – 50 cm^{-1} (Mn-O and Na-O bonding, respectively). The FTIR spectrum for nolzeite shows bands at ~ 2800 – 3600 cm^{-1} (O-H) stretching, a moderately sharp band at 1631 cm^{-1} (H-O-H) bending, strong, sharp bands at ~650 – 700 cm^{-1}, ~ 800 – 840 cm^{-1}, and ~ 900 – 1100 cm^{-1} (Si-O and B-O) bonds. Nolzeite is triclinic, crystallizing in space group $P\bar{1}$ with *a* 6.894(1), *b* 7.632(2), *c* 11.017(2) Å, α 108.39(3), β 99.03, γ 103.05(3)°, *V* 519.27 $Å^3$, and *Z* = 2. The crystal structure was refined to *R* = 12.37 % and wR^2 = 31.07 % for 1361 reflections ($F_o > 4\sigma F_o$). It is based on chains of

tetrahedra with a periodicity of three (*i.e.*, a *dreier* chain) consisting of three symmetrically independent SiO_4 tetrahedra forming *C*-shaped clusters closed by $BO_2(OH)_2$ tetrahedra, producing single loop-branched *dreier* borosilicate chains. The chains are linked through shared corners to double chains of edge-sharing $MnO_5(OH)$ octahedra. Nolzeite is a chain silicate closely related to steedeite and members of the sérandite-pectolite series. Paragenetically, nolzeite is late-stage, likely forming under alkaline conditions and over a narrow range of low pressures and temperatures.

3.2 Introduction

Nolzeite, ideally $Na(Mn,\square)_2Si_3(B,Si)O_9(OH)_2 \bullet 2H_2O$, is a new borosilicate from Mont Saint-Hilaire, Québec, Canada, one of the world's most prolific localities for new minerals (Chao *et al*. 1990). It was investigated as part of a broader examination of borosilicate minerals found at this locality, a list of which currently numbers twelve. The mineral occurs as fine acicular crystals whose small size initially inhibited determination of its structure *via* standard single crystal diffractometers employing scintillation detectors. Determination and refinement of the crystal structure were critical not only to confirming the presence of both H_2O and (OH) in the mineral but also in recognizing that the mineral contains essential B_2O_3. In this contribution we present a complete crystal-chemical characterization of nolzeite, elucidate the relationship of this mineral to members of the sérandite – pectolite series and provide insights into the conditions that led to its formation. Nolzeite is named for Dr. Gert Nolze (*b*. 1960), a crystallographer at the Federal Institute for Materials Research and Testing (BAM), Berlin, Germany. Dr. Nolze, in conjunction with Dr. Werner Kraus, developed *Powdercell* (Kraus & Nolze 1996; currently in ver. 2.4), a program that has been extensively used in the calculation of powder X-ray diffraction patterns of minerals. Dr. Nolze is an expert in the field of electron microbeam techniques, in particular,

electron back-scatter diffraction (EBSD) and he has applied his knowledge to the study of minerals in meteorites (Nolze *et al*. 2005). Both the mineral and mineral name have been approved by the International Mineralogical Association, Commission on New Minerals and Mineral Names (2014 – 086). The holotype material is housed in the collections of the Canadian Museum of Nature (Gatineau, Quebec, Canada), catalogue number CMNMC 86851.

3.3 Occurrence

Nolzeite was discovered by Col. Quintin Wight in August 1987 and was provisionally designated UK78. The mineral was initially found in ~ 1 cm diameter vugs in a loose boulder (~1 x 1 m) of sodalite syenite at the Poudrette quarry, La Vallée-du-Richelieu, Montérégie (formerly Rouville County), Québec, Canada (45°33′8″N, 73°9′3″W). The loose boulder was found in the south-east portion of the quarry, in proximity to a large number of so-called sodalite syenite xenoliths (tawites) in nepheline syenite (McDonald & Chao 2010, McDonald & Chao 2005). The boulder containing nolzeite was first noted because of the unusually high concentration of relatively thick, euhedral plates of pyrrhotite contained within it. When the boulder was broken up, numerous, centimetre-sized vugs filled with clear, crystalline natron ($Na_2CO_3•10H_2O$) or natrite (Na_2CO_3) were exposed. These minerals subsequently decrepitated to thermonatrite ($Na_2CO_3•H_2O$) and related minerals. The sample containing nolzeite consists predominantly of microcline, analcime, nepheline along with aegirine, and pyrrhotite (Table 3-1). The pyrrhotite associated with nolzeite is magnetic, suggesting that it is the monoclinic 4*C* polytype. The rest of the sample is dominated by sodalite, a eudialyte-group mineral, sérandite, and thermonatrite (Table 3-1). Interestingly, some crystals of sodalite are found to atypically retain a pronounced violet color even after prolonged exposure (*i.e*., several years) to light. The sérandite is highly unusual for the locality, ranging in colour from dark to pale green and brown to light brown in

colour unlike the much more typical pink to orange colouration that characterizes the mineral in other environments at Mont Saint-Hilaire. This green to brown colouration is attributed to trace amounts of iron in the sérandite. It may also be noteworthy that sérandite, steedeite [$NaMn_2Si_3BO_9(OH)_2$; Haring & McDonald (2014)] and nolzeite, although occurring in the same samples, have not been specifically found together in the same vug. These minerals are all late-stage phases, having a strong crystal-chemical similarity, implying they all formed under similar geochemical conditions.

3.4 Physical and Optical Properties

Crystals of nolzeite are euhedral, acicular and elongate along [001], occurring in slightly radiating to loose, randomly oriented groupings ('nests'; Fig. 3-1). They exhibit the forms pinacoid {100}, pinacoid {010} and pinacoid {001}. Crystals have average dimensions 5 x 8 x 55 μm and average length-to-width ratios of ~ 69 – 110. They are pale green to colourless with a white streak and a vitreous lustre. Nolzeite does not show any fluorescence under short-, medium-, or long-wave UV radiation unlike the closely related species steedeite. This feature may thus be useful in distinguishing between the two minerals. Due to the small size of the crystals, a Mohs' hardness for nolzeite could not be measured. A density of 2.79 g/cm^3 was calculated using the empirical chemical formula and unit-cell parameters derived from the crystal-structure analysis.

Nolzeite is assumed to be a biaxial, based on its crystal system. A complete set of optical data could not be collected due to the small crystal size and highly acicular habit of the mineral. It exhibits a positive elongation and refractive indices of n_{min} = 1.616(2) and n_{max} = 1.636(2) as measured with a Na-vapour lamp (λ = 589 nm). These refractive indices are lower than those of

steedeite (n_{min} = 1.636 (2) and n_{max} = 1.656(2)) (Haring & McDonald 2014) and sérandite-pectolite (n_{min} = 1.674(2) and n_{max} = 1.710(2)) possibly due to the more hydrous chemistry of nolzeite compared to steedeite and sérandite-pectolite. No pleochroism was observed. The Gladstone - Dale relation (Mandarino, 1981) gives a compatibility index $1-(K_P/K_C)$ = 0.020 (excellent) using the empirical formula and unit-cell parameters derived from the crystal structure analysis.

3.5 Chemical Composition

Chemical analyses of nolzeite were collected using a JEOL JSM 6400 scanning electron microscope equipped with an energy-dispersive spectrometer and operating conditions of: voltage = 20 kV, ~1 nA beam current and a beam width of ~1 um (Central Analytical Facility, Laurentian University). Energy-dispersive data were collected using the following standards: albite (Na*K*α), diopside (Ca*K*α, Si*K*α), tephroite (Mn*K*α), and chalcopyrite (Fe*K*α, S*K*α). Chemical analyses (n = 6) of four crystals gave an average (range, standard deviation) of: Na_2O 7.34 (6.30 – 8.10, 0.66), CaO 0.29 (0.21 – 0.35, 0.05), MnO 27.29 (25.99 – 28.52, 0.97), FeO 0.83 (0.76 – 0.93, 0.08), SiO_2 44.17 (43.30 – 45.35, 0.79), SO_3 0.67 (0.35 – 1.02, 0.30), B_2O_3 (calc.) 5.45, and H_2O (calc.) 12.16, total 98.20 wt. %. The empirical formula based on 13 anions is: $Na_{1.04}(Mn_{1.69}\square_{0.24}Fe_{0.05}Ca_{0.02})_{\Sigma=2.00}(Si_{2.96}S_{0.04})_{\Sigma=3.00}(B_{0.70}Si_{0.30})_{\Sigma=1.00}O_9(OH)_2 \bullet 2H_2O$ or ideally $Na(Mn,\square)_2[Si_3(B,Si)O_9(OH)_2] \bullet 2H_2O$. The ideal formula requires: Na_2O 7.24, MnO 28.16, SiO_2 46.30, B_2O_3 5.69, and H_2O 12.62 wt. %, total 100.00 wt. %, assuming that the *Mn* sites are 85 % occupied and the *B* site is fully occupied with a substitution of 30 % Si. Amounts of B, OH, and H_2O were calculated based on electroneutrality considerations and their presence was confirmed through a combination of crystal-structure and infrared analyses (see below), respectively. The presence of B was further confirmed through qualitative analyses made by SEM-EDS using an

operating voltage of 5 kV, a beam current of ~ 1 nA, a beam diameter of ~1 μm, a 15 s count time (longer count times led to sample degradation) and a light-element detector. The samples were Au-coated so as to mitigate problems associated with the near-overlap of C and B in EDS spectra. Results show that the EDS spectra of nolzeite and a tourmaline-supergroup mineral both contain peaks at ~ 0.17 keV (Fig. 3-2) which can be attributed to B (ideally, B*K*α = 0.183 eV), confirming the presence of B in both minerals. Nolzeite does not effervesce in 10% HCl at room temperature.

3.6 Raman Spectroscopy

A Raman spectrum of nolzeite, based on an average of three 20 s acquisition cycles over a range of 50 to 4000 cm^{-1}, was collected using a Horiba Jobin Yvon XPLORA Raman spectrometer interfaced with an Olympus BX41 microscope (Central Analytical Facility, Laurentian University). An excitation radiation of λ = 638 nm was used along with a 600 lines/mm grating and 100 x magnification (producing a beam of diameter ~ 2 μm). The excitation radiation of λ = 638 nm was chosen to minimize fluorescence peaks in the region of ~2000 to 2800 cm^{-1} that were observed when the mineral was analyzed using the more typically employed radiation of λ = 532 nm. Calibration was made using the 521 cm^{-1} line of a silicon wafer. Six distinct groups of bands occur in the Raman spectrum of nolzeite at ~ 3600 – 3300 cm^{-1}, 1600 – 1500 cm^{-1}, 1300 – 1200 cm^{-1}, 1030 – 800 cm^{-1}, 700 – 500 cm^{-1}, and 400 – 50 cm^{-1} (Fig. 3-3). The first of these bands at ~3600 – 3300 cm^{-1} consists of two broad, low intensity peaks that are attributed to O-H stretching (Table 3-2) (Williams 1995). The next band at 1600 – 1500 cm^{-1} contains a single sharp, moderate intensity peak at 1586 cm^{-1} attributed to H-O-H bending. A single moderately sharp, low intensity peak occurs in the band at 1300 – 1200 cm^{-1} at 1290 cm^{-1}. A similar peak can also be found in the Raman spectrum of steedeite at 1368 cm^{-1} (Haring & McDonald 2014).

The Raman spectrum of steedeite (Table 3-2) was calculated using the computer programs Gaussian (Frisch *et al*. 2013) and Vibratz (Dowty 2009) so as to confirm band assignments for both nolzeite and steedeite. Given the chemical and structural similarities between steedeite and nolzeite, it is likely that the peak at 1290 cm^{-1} in the spectrum of nolzeite is also the result of B-OH bonding. The reason for the shift in the B-OH peak in nolzeite relative to steedeite is unknown. An increase in the Si↔B substitution is expected to cause the B-OH peak to shift higher wave numbers in the Raman spectrum of nolzeite compared to that of steedeite. Instead the opposite is observed where the B-OH peak in the spectrum nolzeite is observed at lower wave numbers than the corresponding peak in the spectrum of steedeite. The Raman band at 1030 – 800 cm^{-1} contains two sharp, low intensity peaks at 1009 and 842 cm^{-1} attributed to asymmetric Si-O_{nbr}/B-O stretching and symmetric Si-O stretching respectively (Williams 1995). Similar peaks occur in steedeite at 874 and 1000 cm^{-1} but these are sharper with higher intensities compared to those in nolzeite. Furthermore, the peak at 842 cm^{-1} in nolzeite is at a lower wave number compared to the equivalent peak in steedeite, this being attributed to the slightly longer and lower energy Si-O contains two sharp, high intensity peaks at 626 and 553 cm^{-1}. These peaks are attributed to a combination of Si-O-Si bending and Mn-O bonding (Williams 1995). Finally the band at 400 – 50 cm^{-1} contains five sharp, low to high intensity peaks at 390, 341, 268, 223, and 167 cm^{-1} attributed to Mn-O as well as Na-O bonding. Steedeite and nolzeite may be distinguished based on their Raman spectra. Unlike the Raman spectrum of nolzeite, the Raman spectrum of steedeite contains no peaks in the region of 1500 – 1600 cm^{-1} (H-O-H bending). Furthermore, the peaks in the spectrum of nolzeite tend to occur at lower wave numbers than those of steedeite due to the longer Si-O bonds in nolzeite (see discussion above).

3.7 Infrared Spectroscopy

An infrared (FTIR) spectrum (Fig. 3-4) was collected at the over a range of 600 to 4000 cm^{-1} using a Bruker Alpha spectrometer (Department of Chemistry and Biochemistry, Laurentian University) equipped with a KBr beam splitter and a DTGS detector. The spectrum, obtained by averaging 128 scans with a resolution of 4 cm^{-1}, reveals five distinct bands at ~650 – 700 cm^{-1}, 800 – 840 cm^{-1}, 900 – 1100 cm^{-1}, 1631 cm^{-1}, ~ 2800 – 3600 cm^{-1}. The 800 – 840 cm^{-1} are associated with symmetric Si-O bending, and the bands at 900 – 1100 cm^{-1} are associated with asymmetric Si-O bending or possibly B-O bending (Frost et al. 2007, Williams 1995). The remaining bands at 1631 cm^{-1} and ~ 2800 – 3600 cm^{-1} are associated with H-O-H and O-H bending, respectively (Williams 1995). Peaks associated with Na-O bonds tend to occur below 600 $cm^{-1}$and were thus not detected. The FTIR and Raman spectra for nolzeite both show a peak in the region of 600 to 700 cm^{-1} but that in the FTIR spectrum occurs at a higher wave number (697 cm^{-1}) than the equivalent in the Raman spectrum (626 cm^{-1}). In addition, both spectra show peaks in the region of 800 to 1100 cm^{-1} however, more peaks with higher intensities occur in the 800 to 1100 cm^{-1} region of the FTIR spectrum. This could be due to the fact that crystals of nolzeite were powdered to make a KBr pellet for FTIR analysis, whereas Raman analysis was conducted on single crystals. The powdering of nolzeite during the preparation of KBr pellets would have minimized preferred-orientation effects. Finally the FTIR spectrum, unlike the Raman spectrum, shows distinct bands in the regions of ~ 1600 – 1700 cm^{-1} and ~2800 – 3600 cm^{-1} attributed to H-O-H and O-H bending. The bands attributed to O-H and H-O-H are weak to non-existent in the Raman spectrum, possibly owing to the low polarizability of H-O bonds.

3.8 X-ray Crystallography and Crystal Structure Determination

Powder *X*-ray diffraction data were collected using 114.6 mm diameter Gandolfi camera, 0.3 mm collimator, and Fe-filtered Co*K*α radiation (λ = 1.7902 Å). Intensities were determined using a scanned image of the powder pattern and normalized to the measured intensity of d = 10.113 Å (I = 100). A calculated X-ray pattern, determined using the results from the crystal-structure analysis and the program PowderCell (Kraus & Nolze 1996), is in good agreement with the observed pattern (Table 3-4).

X-ray intensity data were collected on a Bruker D8 three-circle diffractometer (Department of Geological Sciences, University of Manitoba) equipped with a rotating-anode generator, multi-layer optics incident beam path and an APEX-II CCD detector. X-ray diffraction data (9610 reflections) were collected to 60 °2θ using 20 s per 0.3° frame with a crystal-to-detector distance of 5 cm. The unit-cell parameters were obtained by least-squares refinement of 2706 reflections ($I > 10\sigma I$), and are given in Table 3-3. Empirical absorption corrections (SADABS; Sheldrick, 1998) were applied and identical data merged to give 1361 reflections covering the entire Ewald sphere. Information pertaining to the data collection is given in Table 3-5.

Solution and refinement of the crystal structure of nolzeite were done using SHELXL – 2014 (Sheldrick 2008). The crystal structure was solved by direct methods, using the scattering curves of Cromer & Mann (1968) and the scattering factors of Cromer & Liberman (1970). Phasing of a set of normalised structure factors gave the mean $|E^2 - 1|$ value of 0.996, consistent with a centrosymmetric space group. In light of this and the absence of systematic extinctions, space group P-1 was chosen for the structure solution and refinement. Phase-normalised structure

factors were used to give a difference Fourier map from which one *Na*, three *Si*, two *Mn*, and several *O* sites were located. From subsequent difference-Fourier maps, a [4]-site with bond distances ranging from 1.317 to 1.608 Å was located. This site was assigned to B based on several arguments: (1) the mineral is morphologically, chemically, and on a crystal-structure basis, very similar to steedeite, $NaMn_2Si_3BO_9(OH)_2$, a confirmed a Na-Mn-borosilicate; (2) the two minerals occur together in the same samples from the same occurrence at Mont Saint-Hilaire, suggesting they arose *via* similar physio-chemical processes, including similar late-stage fluids; (3) refinement of the crystal structure of indicates the presence of three [4]-sites attributable to Si and a fourth [4]-site, whose bond distances are shorter-than-ideal for Si-O, but consistent with those for B-O and (4) qualitative EDS scans of both nolzeite and a member of the tourmaline supergroup (preliminary semi-quantitative EDS analyses indicate it to be the species, dravite) confirms the presence of B in both minerals. Determination of which *O* sites were occupied by OH or H_2O was based on bond-valence calculations and electroneutrality considerations (Table 3-8).

Refinement of this model converged to R = 12.81 % and wR^2 = 29.80 %. The relatively high R-factor for the refined crystal structure of nolzeite is attributed to the fact that the crystal studied by single-crystal X-ray diffraction (SXRD) was extremely thin in two directions (measuring 7 x 8 x 60 μm) and that it may not have been truly single. Although preliminary examination of this crystal with a polarized-light microscope indicated a sharp, strong extinction, implying it was single, further examination of the SXRD data revealed a subtle, but detectable, splitting of some diffraction spots, suggesting that the crystal may not in fact have been truly single. Single crystal data produced from this crystal gave R_{int} = 4.75 % and R_{sym} = 7.13%. In light of this, a second

SXRD data collection was attempted on an even thinner crystal measuring 4 x 6 x 50 μm, the data from which did not indicate any pronounced splitting of diffraction spots, *i.e.*, that it was single. However, the second crystal was found to be an extremely poor X-ray scatterer (presumably due to its fine acicular size), *i.e.*, significantly less than that for the first crystal, for which data were produced out to $2\theta = 60$ °. Despite the reduction in observable data for the second crystal, attempts were made to refine the crystal structure but these were unsuccessful, as the *R*-factor could not be reduced below 30%.

3.9 Crystal Structure

The crystal structure of nolzeite contains three *Si* sites, two *Mn* sites, and two unique *Na* and *B* sites (Table 3-6). All of the sites were found to be fully occupied with the exception of the *Mn* sites which refined to site occupancies of 0.85. The three *Si* sites are coordinated by four crystallographically distinct O atoms with Si-O bond lengths ranging from 1.60(1) to 1.69(1) Å (Table 3-7). The *B* site is coordinated by two O atoms and two (OH) groups, forming a $BO_2(OH)_2$ tetrahedron with B-(O,OH) bond lengths ranging from 1.32(4) to 1.61(3) Å (Table 3-6). This type of B-O tetrahedron is extremely unusual, having only been reported in two other minerals: rogermitchellite [$Na_{12}(Sr,Na)_{24}Ba_4Zr_{26}Si_{78}(B,Si)_{12}O_{246}(OH)_{24}\bullet 18H_2O$; McDonald & Chao (2010)] and steedeite [$NaMn_2Si_3BO_9(OH)_2$; Haring & McDonald (2014)], both of which are known to occur only at Mont Saint-Hilaire. The site attributed to B has B-(O,OH) lengths ranging from 1.32(4) to 1.61(3) Å with an average<B-O> length of 1.52 Å. The range of B-(O,OH) lengths in nolzeite is greater than those observed in rogermitchellite (1.49 – 1.52 Å) (McDonald & Chao (2010)) and steedeite (1.468 – 1.508 Å) (Haring & McDonald (2014)). For these three minerals, there appears to be no correlation between B-(O,OH) bond length and whether or not B is bonded to O or an OH group. Instead the range of B-(O,OH) lengths

observed in nolzeite may be attributed to Si↔B substitution on the *B* site (see discussion below). The average <B-(O,OH)> length in nolzeite is slightly longer than the ideal length of 1.477 Å for B in tetrahedral coordination (Hawthorne *et al.* 1996). We attribute this longer-than-ideal bond distance to significant (~30%) B ↔Si substitution in the site (Figure 3-5), a fact supported by SEM-EDS data for the mineral which show an excess in SiO_2 over that predicted for an ideal amount (*i.e.*, 44.17 *vs*. 40.78 wt. % SiO_2). The ~30% substitution of B with Si is estimated based on chemical data as well as the unusually long B-O bond lengths.

The two *Mn* sites are octahedrally coordinated with a combination of O anions as well as OH and H_2O groups. Two distinct types of $MnO_5\varphi$ (φ = OH, H_2O) octahedra occur in the crystal structure of nolzeite: 1) $Mn(1)O_5(H_2O)$ octahedra and 2) $Mn(2)O_5(OH)$ octahedra. Both have similar Mn-(O,OH,H_2O) bond lengths, ranging from 2.16(1) to 2.31(1) Å (Table 3-7), which are consistent with the Mn-(O,OH) bonds observed in sérandite (Jacobsen *et al*. 2000). The *Na* site is coordinated by four O atoms, one (OH) group, and two (H_2O) groups, forming $NaO_4(OH)(H_2O)_2$ polyhedra, with Na-(O,OH,H_2O) bond lengths ranging from 2.26(2) to 2.69 (2) Å (<Na-(O,OH)> = 2.48 Å, Table 3-5).

Each SiO_4 tetrahedron in the crystal structure of nolzeite is linked to two adjacent SiO_4 tetrahedra through shared corners, forming infinite single silicate chains parallel to *a* (*i.e.*. the elongation direction). The silicate chains have a repeat unit consisting of three symmetrically independent SiO_4 tetrahedra: $Si(1)O_4$, $Si(2)O_4$ and $Si(3)O_4$, forming *C*-shaped clusters (Fig. 3-6). These clusters are closed by $BO_2(OH)_2$ tetrahedra *via* shared corners, generating four-membered $[BSi_3O_{12}]^{7-}$ rings (Fig. 3-6). The $BO_2(OH)_2$ tetrahedra are therefore branching

tetahedra so the silicate chain in nolzeite can be classed as a loop-branched *dreier* chain silicate (Liebau 1978). Such borosilicate chains are unusual and have been found in only one other naturally occurring mineral, steedeite (Haring & McDonald 2014). The loop-branched tetrahedral chains are linked through shared corners to double chains of edge-sharing $MnO_5\varphi$ octahedra completing the 3D structure. The loop-branched silicate chains and $MnO_5(OH)$ chains form distinct tetrahedral (*T*) and octahedral (*O*) layers, respectively, resulting in a *T*-*O*-*T*-*O*... stacking sequence perpendicular to {101} (Fig. 3-7). This stacking orientation is slightly different from that of steedeite, where the T-O stacking is perpendicular to {011}, resulting in the variation in refractive indices and Raman spectra between the two minerals. The stacking pattern in nolzeite, along with the linkages between the layers of tetrahedra and octahedra, gives rise to an *I*-beam topology (Thompson 1970). These "I-beams" are linked through shared corners to adjacent ones to form layers along {001}, which alternate with layers containing the $NaO_4(OH)(H_2O)_2$ polyhedra.

3.10 Related Structures

The *I*-beam topology and the *T*-*O*-*T* stacking pattern present in nolzeite is similar to that found in other chain silicate minerals, specifically steedeite, as well as pyroxenoids of the pectolite ($NaCa_2[Si_3O_8OH]$)–sérandite ($NaMn_2[Si_3O_8OH]$) series, which are also hydrated and have $P\bar{1}$ symmetry. The crystal structure of nolzeite most closely resembles that of steedeite as the single loop-branched *dreier* borosilicate chains present are identical to those in steedeite (Haring & McDonald 2014). The crystal structures of pectolite – sérandite series pyroxenoids also consist of *dreier* silicate chains (Waldemar 1955, Prewitt 1967) similar to those in nolzeite, but differ in that they are unbranched *dreier* chains (Fig. 3-4). Nolzeite, steedeite and members of the

pectolite–sérandite series also all contain double chains of edge-sharing octahedra. Chemically, nolzeite has proportions of Na, Mn, and Si identical to those of steedeite, but nolzeite contains H_2O groups and has a mixed B/Si site.

The crystal structure of nolzeite is also similar to that of scheuchzerite $\{Na(Mn,Mg)_9[VSi_9O_{28}(OH)](OH)_3\}$; Brugger *et al*. 2006). Both minerals have hydrated loop-branched chain silicate structures but the silicate chains in scheuchzerite are more complex, with a periodicity of seven and six-membered silicate rings that alternate with *C*-shaped silicate clusters (Brugger *et al.* 2006; Fig. 3-4). Each six-membered silicate ring within the silicate chain in scheuchzerite is linked through a shared corner to a single tetrahedron $(VO_4)^{3-}$ tetrahedron (Brugger *et al*. 2006). The $(VO_4)^{3-}$ group is considered to be a branching tetrahedron, therefore the silicate chain in scheuchzerite can be considered as being both loop-branched and open branched (Liebau 1978). The crystal structures of scheuchzerite and nolzeite both contain bands of edge-sharing $Mn(O,OH)_6$ octahedra. The bands of $Mn(O,OH)_6$ octahedra in scheuchzerite (Brugger *et al*. 2006) are wider than those in nolzeite, with a single and of octahedra varying from three to four octahedra wide, while that in nolzeite is only two octahedra wide.

There are also two synthetic phases, $Li_2Mg_2(Si_4O_{11})$ (Maresch & Czank 1985, Czank & Bissert 1993) and $Fe_3Be(Si_3O_9)(F,OH)_2$ (Bakakin & Solov'eva 1971) that have single loop-branched *dreier* chains similar to those in nolzeite. The crystal structure of $Li_2Mg_2(Si_4O_{11})$, as in nolzeite, has tetrahedral chains consisting of *C*-shaped clusters of three SiO_4 tetrahedra. These clusters are closed by a fourth SiO_4 tetrahedron [rather than a $BO_2(OH)_2$ tetrahedron as in nolzeite] generating four-membered $(Si_4O_{11})^{6-}$ rings (Czank & Bissert 1993; Fig. 3-4). The silicate chains

are linked through shared corners to double chains or bands of edge-sharing MgO_6 octahedra (Czank & Bissert 1993). The crystal structure of $Fe_3Be(Si_3O_9)(F,OH)_2$ contains loop-branched *dreier* silicate chains similar to those in nolzeite but with BeO_4 tetrahedra instead of $BO_2(OH)_2$ tetrahedra closing the *C*-shaped silicate clusters. The silicate chains in $Fe_3Be(Si_3O_9)(F,OH)_2$ are linked through shared corners to triple chains of edge-sharing FeO_6 octahedra.

3.11 Origin

Paragenetically, nolzeite, along with sérandite, steedeite, UK80, and thermonatrite are late-stage phases which overgrow earlier-formed phases such as microcline, aegirine and analcime (Table 3-9). Thermonatrite is inferred to have been the latest crystallizing phase. The paragenetic sequence of nolzeite relative to sérandite, steedeite, and UK80 is unclear (Table 3-9), as none have been found together in the same vug (see discussion below).

In general, the hydrous structure of nolzeite and its occurrence in vugs suggests that it crystallized from late-stage aqueous fluids. These fluids are inferred to have been highly alkaline due to the presence of late-stage natrite (Table 3-9). Experimental studies showed that the maximum stability of the latter mineral is in the pH range of ~ 8 to 10 (Marion 2001). Based on fluid-inclusion data as well as carbonate-carbonate and carbonate-silicate equilibria, the temperatures of late-stage fluids at Mont Saint-Hilaire are inferred to have been < 400 °C (Schilling *et al*. 2011). The occurrence of nolzeite, steedeite, sérandite, and the unidentified mineral UK80 in vugs of the same xenolith, suggests that these minerals precipitated from similar late-stage aqueous fluids. The presence of late-stage sérandite (Table 3-9) in the same sample as nolzeite and steedeite also suggests that the aqueous fluid had localized variations in $a_{[SiO2]4-}$ as well as $a_{B(OH)3}$ and $a_{[B(OH)4]^-}$, whereas a decrease in $a_{[SiO4]4^-}$ and an increase in both

$a_{B(OH)3}$ and $a_{[B(OH)4]-}$ favoured the development of nolzeite and steedeite over sérandite (Haring & McDonald 2014). Due to the possible variations in $a_{B(OH)3}$ in the late-stage fluids, it is unclear whether or not the crystal structure of UK80 also contains B.

Another indication for the low-*T* formation of nolzeite may be the conditions at which minerals of the sérandite–pectolite series form (Haring & McDonald 2014, Clark & Bunn 1940, Blakeman *et al*. 1974, Xi & Glasser 1984). Given the existence of late-stage sérandite in the same boulder wherein nolzeite was found implies that nolzeite likely formed under a similar range in *T*. It is noteworthy that nolzeite and steedeite are the only minerals known to contain single looped-branched *dreier* silicate chains, suggesting that they may be stable over a very narrow *P – T* range (Haring & McDonald 2014).

3.12 References

Bakakin, V.V. & Solo'eva, L.P. (1971): Crystal structure of $Fe_3BeSi_3O_9(F,OH)_2$, an example of a wollastonite-like silicon-oxygen chain based on Fe. Soviet Physics Crystallography, 15, 999-1005.

Blakeman, E.A., Gard, J.A., Ramsay, C.G. & Taylor, H.F.W. (1974): Studies on the system sodium oxide - calcium oxide - silica - water. Journal of Chemical Technology and Biotechnology, 24. 239-245.

Brese, N.E. & O'Keeffe, M. (1991): Bond-valence parameters for solids. Acta Crystallographica, B47, 192-197.

Brugger, J., Krivovichev, S., Meisser, N., Ansermet, S., & Armbruster, T. (2006): Scheuchzerite, $Na(Mn,Mg)_9[VSi_9O_{28}(OH)](OH)_3$, a new single-chain silicate. American Mineralogist, 91, 937-943.

Chao, G.Y., Conlon, R.P. & Velthuizen, J. (1990): Mont Saint-Hilaire Unknowns. The Mineralogical Record, 21, 363-368.

Clark, L.M. & Bunn, C.W. (1940): The scaling of boilers. Pt. IV. Identification of phases in calcium silicate scales. Journal of the Society of Chemical Industry. 59, 155-158.

Cromer, D.T. & Liberman, D. (1970): Relativistic calculation of anomalous scattering factors for X rays. Journal of Physical Chemistry, 53, 1891-1898.

Cromer, D.T. & Mann, J.B. (1968): X-ray scattering factors computed from numerical Hartree-Frock wave functions. Acta Crystallographica, A24, 321-324. ces, 44: 1333-1346.

Czank, M. & Bissert, G. (1993): The crystal structure of $Li_2Mg_2[Si_4O_{11}]$, a loop-branched dreier single chain silicate. Zeitschrift für Kristallographie, 204, 129-142.

Dowty, E. (2009): VIBRATZ for Windows and Macintosh Version 2.2. Shape Software Kingsport, Tennessee, USA.

Frisch,M. J., Trucks, G. W. Schlegel, H. B., *et al*. (2013): Gaussian 09, Revision D.01. Gaussian, Inc., Wallingford CT.

Frost, R.L., Bouzaid, J.M., Martens, W.N. & Reddy, J.B. (2007): Raman spectroscopy of the borosilicate mineral ferroaxinite. Journal of Raman Spectroscopy, 38, 135-141.

Haring, M.M.M. & McDonald A.M. (2014): Steedeite, NaMn2[Si3BO9](OH)2: Characterization, crystal-structure determination, and origin. Canadian Mineralogist, 52, 47-60.

Hawthorne, F.C., Burns, P.C. & Grice, J.D. (1996): The crystal chemistry of boron. Reviews in Mineralogy, 33, 41-110.

Jacobsen, S.D., Smyth, J.R., Swope, J.R., & Sheldon, R.I. (2000): Two proton positions in the very strong hydrogen bond of sérandite, $NaMn_2[Si_3O_8(OH)]$. American Mineralogist, 85, 745-752.

Kraus, W. & Nolze, G. (1996): Powder Cell – a program for the representation and manipulation of crystal structures and calculatuion of the resulting x-ray powder patterns. Journal of Applied Crystallography, 29, 301-303.

Liebau, F. (1978): Silicates with branched anions: a crystallochemically distinct class. American Mineralogist, 63, 918-923.

Mandarino J. A. (1981): The Gladstone–Dale relationship. IV. The compatibility concept and its application. Canadian Mineralogist, 19,441-450.

Maresch, W.V. & Czank, M. (1985): The optical and X-ray properties of $Li_2Mg_2[Si_4O_{11}]$, a new type of chain-silicate. Neues Jahrbuch für Mineralogie, 7, 289-297.

Marion, G.M. (2001): Carbonate mineral solubility at low temperatures in the Na-K-Mg-Ca-H-Cl-SO_4-OH-HCO_3-CO_3-CO_2-H_2O system. *Geochimica et Cosmochimica Acta, 65*, 1883-1896.

McDonald, A.M. & Chao, G.Y.(2005): Bobtraillite, $(Na,Ca)_{13}Sr_{11}(Zr,Y,Nb)_{14}Si_{42}B_6O_{132}(OH)_{12}\bullet 12H_2O$ a new mineral species from Mont Saint-Hilaire, Québec: description, structure determination and relationship to benitoite and wadeite. Canadian Mineralogist, 43, 747-758.

McDonald, A.M. & Chao, G.Y. (2010): Rogermitchellite, $Na_{12}(Sr,Na)_{24}Ba_4Zr_{26}Si_{78}(B,Si)_{12}O_{246}(OH)_{24}•18H_2O$, a new mineral species from Mont Saint-Hilaire, Québec: description, structure determination and relationship with HFSE-bearing cyclosilicates. Canadian Mineralogist, 48, 267-278.

Nolze, G., Geist, V., Neumann, R.S. & Buchheim, M. (2005): Investigation of orientation relationships by EBSD and EDS on the example of the Watson iron meteorite. Crystallographic Research and Technology, 40, 791-804.

Prewitt, C.T. (1967): Refinement of the crystal structure of pectolite, $Ca_2NaHSi_3O_9$. Zeitschrift für Kristallographie, 125, 298-316.

Schilling, J., Marks, M.A.W., Wenzel, T., Vennemann, T., Horvath, L., Tarassoff, P., Jacob, D.E., & Markl, G. (2011): Magmatic to hydrothermal evolution of the intrusive Mont Saint-Hilaire complex: insights into the late-stage evolution of peralkaline rocks. Journal of Petrology, 52, 2147-2185.

Shannon, R.D. (1976): Revised effective ionic radii and systematic studies in interatomic distances in halides and chalogenides. Acta Crystallographica, A32, 751-767.

Sheldrick, G.M. (2008): A short history of *SHELX*. Acta Crystallographica, A64, 112–122.

Thompson, J.B. (1970): Geometrical possibilities for amphibole structures: Model biopyriboles. American Mineralogist, 63, 239-249.

Waldemar, T.S. (1955): The pectolite-serandite series. American Mineralogist, 40, 1022-1031.

Williams, Q. (1995): Infrared, Raman and optical spectroscopy of Earth materials. American Geophysical Union, 291- 302.

Xi, Y. & Glasser L.S.D. (1984): Hydrothermal study in the system Na2O-CaO-SiO2-H2O at 300 degrees celcius. Cement Concrete Research, 14. 741-748.

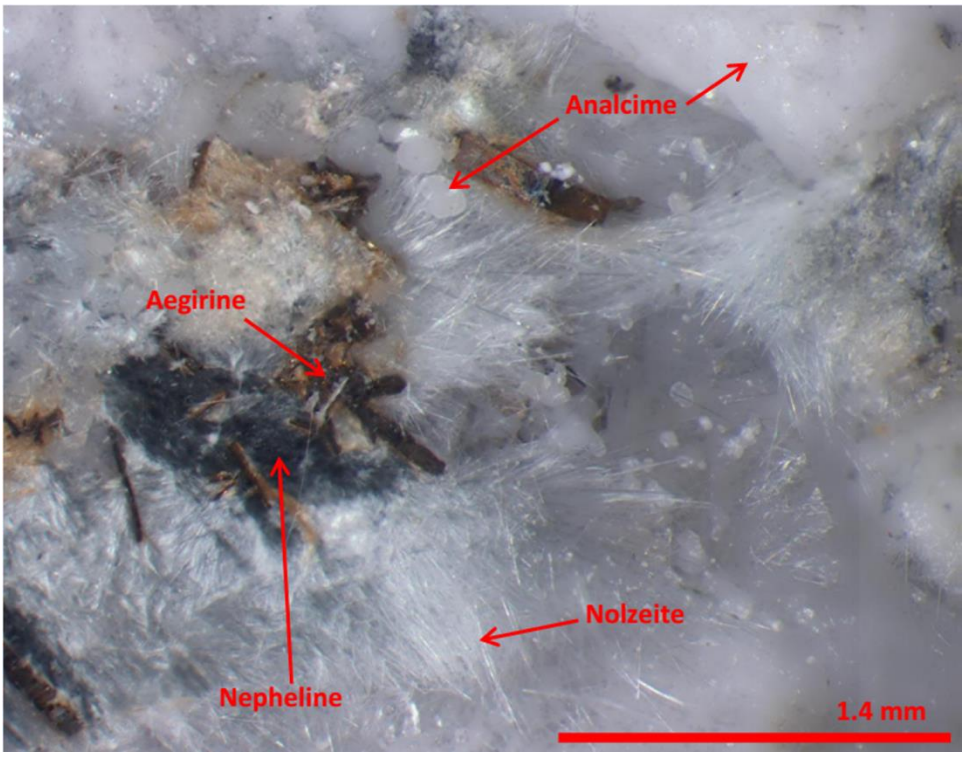

Figure 3-1. Loose aggregates of nolzeite with nepheline, aegirine, and analcime.

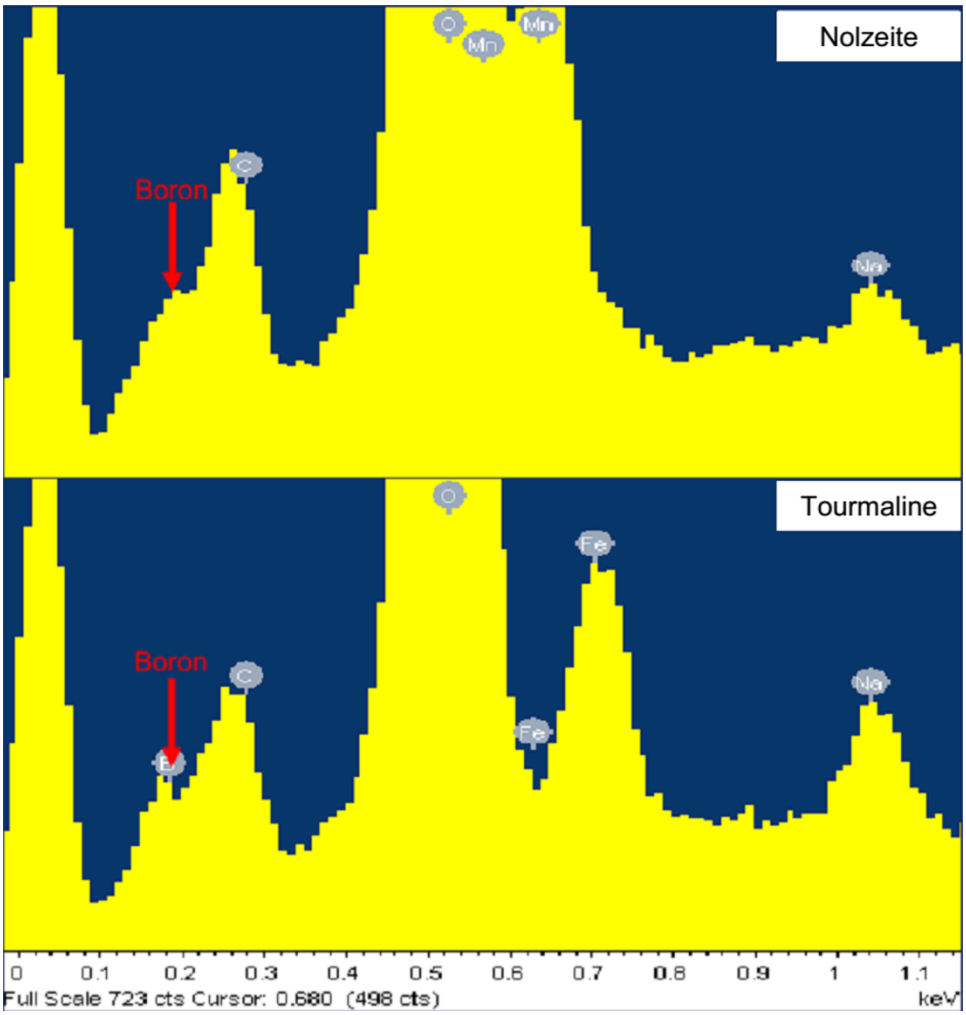

Figure 3-2. Overlay of the EDS spectra for nolzeite and a tourmaline supergroup mineral showing distinctive peaks with similar intensities, attributable to B*Kα*. The presence of C is attributed to contamination.

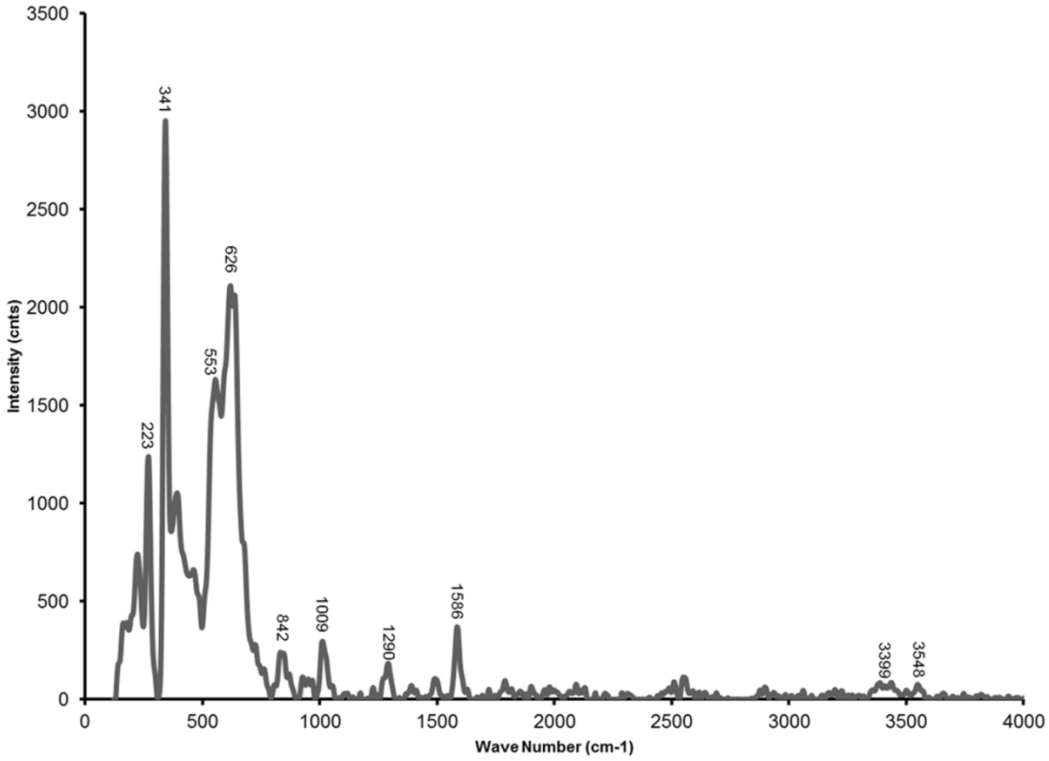

Figure 3-3. Raman spectrum for nolzeite.

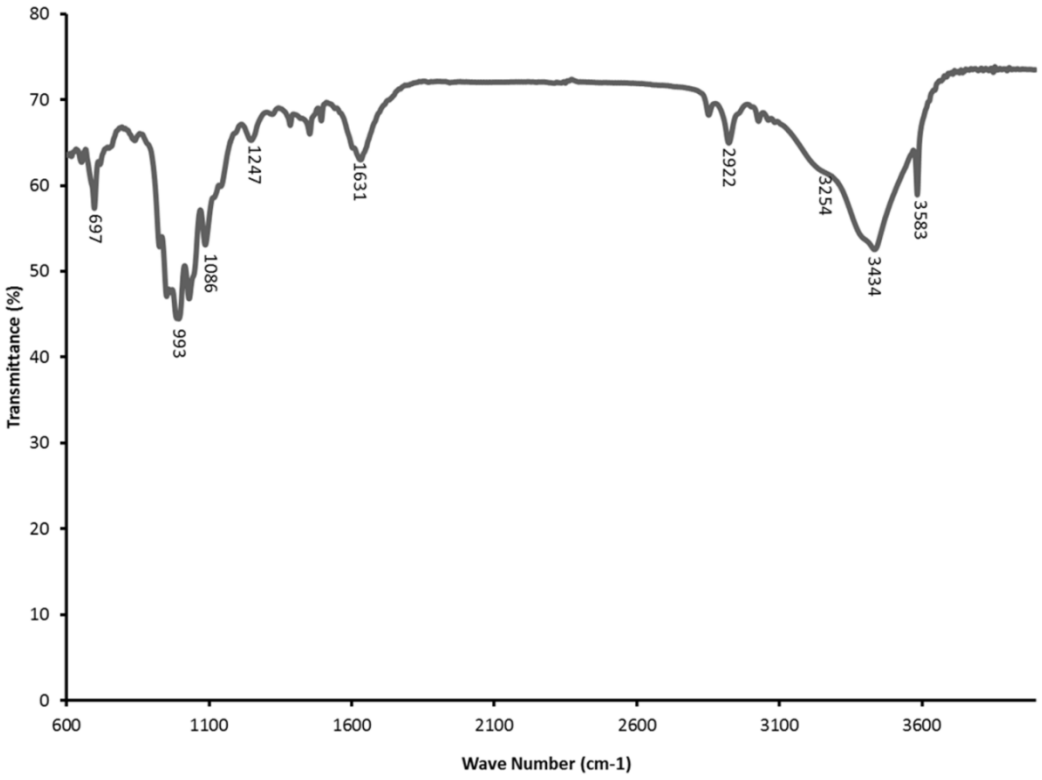

Figure 3-4. FTIR spectrum of nolzeite.

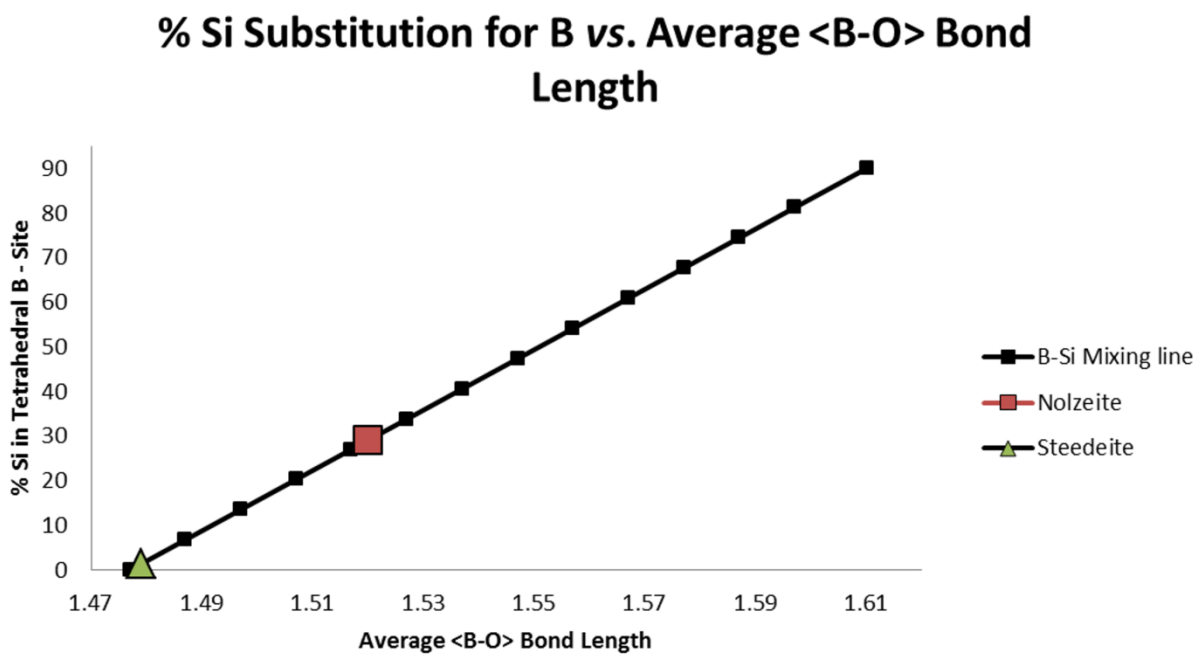

Figure 3-5. The relationship between average <B-O> bond length and the proportion (%) of Si atoms within the B site. The % Si obtained using the following formula: % Si = [(observed<B-O> - 1.477)/(1.630-1.477] * 100.

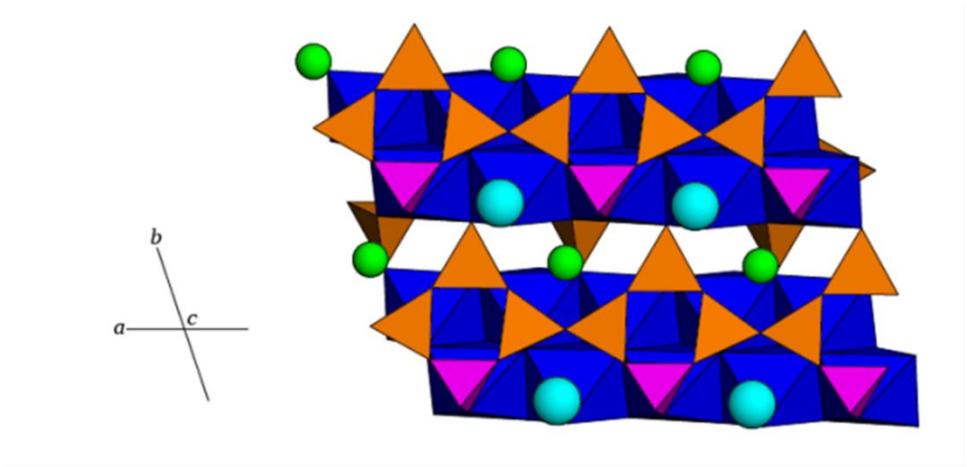

Figure 3-6.The crystal structure of nolzeite projected on to [011]. Both the bands of $MnO_5(OH)$ and the loop-branched *dreier* chains run parallel to *a*. Dark blue octahedra = $MnO_5(OH)$, orange tetrahedra = SiO_4, pink tetrahedra = $BO_2(OH)_2$, light blue spheres = H_2O, and green spheres = Na.

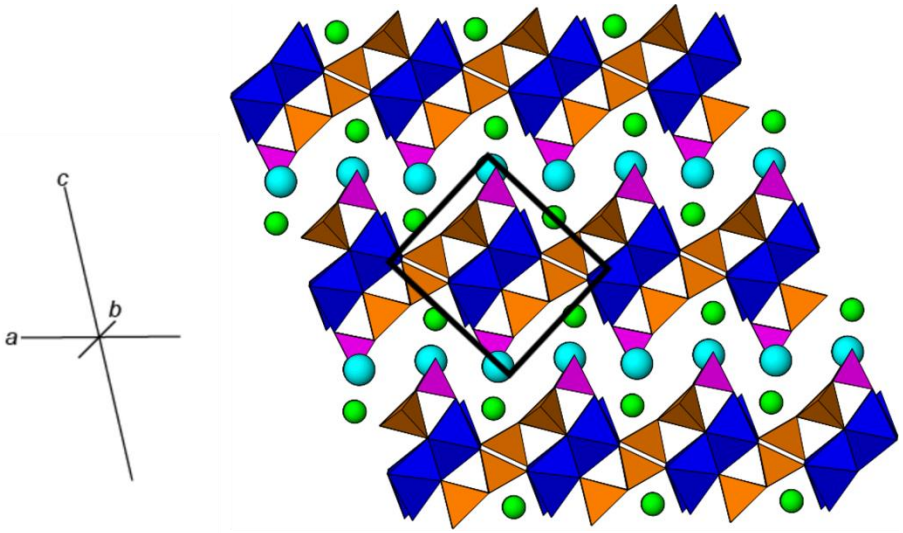

Figure 3-7. The crystal structure of nolzeite with layers of tetrahedra and octahedra alternating along [011] generating an *I*-beam topology. The Mn-borosilicate *I*-beams (outlined in black) form distinct layers that alternate with layers containing water and sodium along [001]. Dark blue octahedra = $MnO_5(OH)$, orange tetrahedra = SiO_4, pink tetrahedra = $BO_2(OH)_2$, light blue spheres = H_2O, green spheres = Na.

Table 3-1. Description and modal abundances of minerals occurring with nolzeite.

Mineral	Modal Abundance	Description
Microcline ($KAlSi_3O_8$)	~ 68 %	Aggregates of anhedral light grey crystals with a massive habit and greasy lustre.
Analcime $Na_2(Al_2Si_4O_{12})•2H_2O$	~ 10 %	Anhedral to subhedral translucent to transparent crystals with a vitreous lustre.
Nepheline $(Na,K)AlSiO_4$	~ 7 %	Anhedral, greenish-grey crystals with a greasy lustre.
Aegirine $NaFe^{3+}Si_2O_6$	~5 %	Dark green, prismatic, euhedral crystals ranging in size from ~ 0.1 to 0.7 mm in length and dominated by the form prism {110}.
Pyrrhotite $Fe_{1-x}S$	~ 5 %	Pseudohexagonal crystals, ~ 4 mm in diameter, displaying the forms pinacoid {001}, pinacoid {100}, prism {100}, and prism {*h0l*}.
Sodalite $Na_8(Al_6Si_6O_{24})Cl_2$	~ 2 %	Anhedral, transparent crystals with a pale blue to violet colour and a strong fluoresence under short-, medium-, and long-wave radiation.

Eudialyte-group mineral $Na_{15}Ca_6(Fe^{2+}, Mn^{2+})_3Zr_3[Si_{25}O_{73}](O,OH,H_2O)_3(OH,Cl)_2$	~ 1 %	Euhedral, translucent to transparent crystals with a dark brown to orange colour.
Sérandite $Na(Mn^{2+},Ca)_2Si_3O_8(OH)$	~ 1 %	Radiating spheres composed of prismatic crystals with flattened terminations (pinacoid {001}). These crystals range in colour from dark to pale green and brown to light brown.
Thermonatrite $Na_2CO_3•H_2O$	~ 1 %	White anhedral to subhedral, translucent crystals.
Catapleiite $(Na,Ca,□)_2ZrSi_3O_9.2H_2O$	trace	Clear, colourless, pseudo hexagonal plates overgrowing sérandite.
Steedeite	trace	Clusters of radiating to randomly oriented, acicular, white to light pink crystals with dimensions similar to those of nolzeite.
UK80	trace	Flat clusters of radiating, brown crystals with dimensions similar to those of nolzeite.

Table 3-2. Absorption bands (cm^{-1}) and band assignments for the Raman spectra of nolzeite and steedeite.

Nolzeite	*Steedeite	Calc. Raman Absorption Bands for steedeite	Assignments
3548	-	-	O-H Stretching
-	3443	3450	O-H Stretching
3399	-	-	O-H Stretching
-	3317	-	O-H Stretching
-	1700	-	unassigned
1586	-	-	H-O-H bending
-	1368	-	B-OH bonds
-	-	1342	B-OH bonds
1290	-	-	B-OH bonds
-	1030	1021	Asymmetric Si-O_{nbr}/B-O stretching
1009	1000	1006	Asymmetric Si-O_{nbr}/B-O stretching
-	874	876	Symmetric Si-O_{br} stretching
842	-	-	Symmetric Si-O_{br} stretching
-	-	852	Symmetric Si-O_{br} stretching
-	826	-	Symmetric Si-O_{br} stretching
-	696	690	Si-O-Si Bending
626	636	624	Si-O-Si Bending/Mn-O
553	-	-	Si-O-Si Bending/Mn-O
-	-	451	Si-O-Si Bending/Mn-O
-	431	-	Mn-O
390	-	-	Mn-O
341	-	-	Mn-O
-	-	366	Mn-O
-	330	-	Mn-O
-	-	289	Mn-O
268	264	-	Mn-O/Na-O
223	-	-	Na-O
-	197	-	Na-O
-	-	156	Na-O
167	-	-	Na-O

* Haring & McDonald (2014)

Table 3-3. FTIR peaks and peak assignments for nolzeite

Peak Position (cm^{-1})	Assignment
3583	O-H stretching
3434	O-H stretching
3254	O-H stretching
2922	O-H stretching
2852	O-H stretching
1631	H-O-H Bending
1247	B-OH bonds
1086	Asymmetric Si-O_{nbr}/B-O stretching
1030	Asymmetric Si-O_{nbr}/B-O stretching
993	Asymmetric Si-O_{nbr}/B-O stretching
951	Asymmetric Si-O_{nbr}/B-O stretching
925	Asymmetric Si-O_{nbr}/B-O stretching
839	Symmetric Si-O_{br} stretching
810	Symmetric Si-O_{br} stretching
697	Si-O-Si bending
652	Si-O-Si bending

Table 3-4. X-ray powder diffraction data for nolzeite.

I_{obs}	I_{calc}	d_{meas} (Å)	d_{calc} (Å)	h	k	l	I_{obs}	I_{calc}	d_{meas} (Å)	d_{calc} (Å)	h	k	l
100	**100**	**10.113**	**10.131**	**0**	**0**	**-1**	6	2	1.950	1.949	2	0	-5
16	**14**	**6.911**	**6.923**	**0**	**-1**	**0**		2		1.948	2	-1	4
4	1	5.034	5.066	0	0	-2	4	1	1.897	1.906	0	-3	5
13	**11**	**3.593**	**3.596**	**0**	**-1**	**3**		1		1.906	2	-3	-2
9	5	3.520	3.522	0	-1	-2		1		1.903	1	-4	2
	1		3.517	0	-2	2	2	1	1.838	1.836	0	-4	3
	2		3.514	1	-2	0	7	1	1.713	1.715	2	1	-6
15	**13**	**3.026**	**3.032**	**0**	**-2**	**3**		1		1.715	2	-2	5
3	2	2.953	2.954	1	2	-1		2		1.714	2	-3	-3
50	**20**	**2.808**	**2.820**	**2**	**1**	**-1**		1		1.714	2	2	2
	21		**2.820**	**2**	**-2**	**0**	5	2	1.687	1.689	0	0	-6
	1		**2.797**	**1**	**-1**	**-3**	4	1	1.663	1.666	2	-4	-1
	1		**2.787**	**1**	**-2**	**3**		1		1.666	2	3	0
7	4	2.767	2.778	2	1	-2	3	1	1.630	1.637	2	3	-5
			2.777	2	-2	1		1		1.637	2	-4	4
6	5	2.719	2.720	0	-1	4	9	2	1.545	1.550	2	-4	-2
12	**8**	**2.675**	**2.675**	**0**	**-1**	**-3**		2		1.550	2	3	1
12	4	2.463	2.469	0	-2	-2		1		1.548	4	-2	-3
	4		2.467	0	-3	2		1		1.548	4	0	1
4	2	2.284	2.292	2	0	-4	4	2	1.498	1.506	2	1	-7
	2		2.290	2	-1	3		2		1.505	2	-2	6
7	2	2.243	2.250	2	2	-2	5	1	1.481	1.481	0	-4	-2
	2		2.250	2	-3	1	3	1	1.445	1.449	4	-2	-4
6	2	2.173	2.180	2	2	-3		1		1.449	4	0	2
	2		2.180	2	-3	2		1		1.447	0	0	-7
8	5	2.138	2.140	0	-1	-4	5	2	1.405	1.407	0	-5	5
3	1	2.093	2.100	2	-1	-4	5	1	1.331	1.334	2	1	-8
	1		2.099	2	0	3		1		1.334	2	-2	7
3	1	2.068	2.069	0	-2	-3	4	1	1.306	1.309	0	-5	-1
7	1	2.024	2.029	2	2	-4							
	1		2.029	2	-3	3							
	2		2.026	0	0	-5							

Table 3-5. Miscellaneous single crystal data for nolzeite.

a (Å)	6.894(1)	Monochromator	Graphite
b	7.632(2)	Intensity-data collection	θ:2θ
c	11.017(2)	Criterion for observed	
α (°)	108.39(3)	reflections	$F_o > 4\sigma(F_o)$
β	99.03(3)	GoF	2.000
γ	103.05(3)	total No. of reflections collected	9610
V (Å^3)	519.27(1)	No. Unique reflections	1361
Space group	*P* $\bar{1}$ (#2)	No. Observed reflections	918
Z	2	R (int %)	4.75
D_{calc} (g/cm^{-3})	2.79	*R* (sym %)	7.13
Crystal Size	7 x 8 x 60 μm	*R* %	12.81
Radiation	Mo*K*α (50 kV, 40 mA)	wR^2 %	29.80

Table 3-6. Atomic coordinates (Å^2) and displacement parameters for nolzeite.

ATOM	*x*	*y*	*z*	SOF	U_{11}	U_{22}	U_{33}	U_{23}	U_{13}	U_{12}	U_{eq}
Na1	0.821(1)	0.072(1)	-0.239(1)	1	0.044(6)	0.057(6)	0.057(7)	0.012(5)	0.010(5)	0.020(5)	0.054(3)
Mn1	0.9536(4)	-0.2913(4)	-0.4112(3)	0.85	0	0.012(2)	0.015(2)	0.004(1)	0.004(1)	0.005(1)	0.009(1)
Mn2	0.5558(4)	-0.7001(4)	-0.5925(3)	0.85	0	0.011(2)	0.015(2)	0.005(1)	0.004(1)	0.004(1)	0.009(1)
Si1	1.3001(9)	0.1011(9)	-0.4088(6)	1	0.013(3)	0.037(4)	0.036(4)	0.007(3)	0.009(3)	0.010(3)	0.030(2)
Si2	1.6857(8)	-0.5657(8)	-0.2701(5)	1	0.015(3)	0.022(3)	0.025(3)	0.009(3)	0.005(3)	0.010(3)	0.020(1)
Si3	1.1474(8)	-0.5689(8)	-0.2708(5)	1	0.012(3)	0.019(3)	0.029(3)	0.010(3)	0.008(3)	0.006(2)	0.019(1)
B Si	1.529(3)	-0.285(4)	-0.087(4)	0.7 0.3	0.051(2)	0.10(2)	0.25(4)	0.10(3)	0.05(2)	0.04(1)	0.12(1)
O1	1.155(2)	-0.483(2)	-0.388(1)	1	0.004(7)	0.022(7)	0.026(8)	-0.007(6)	-0.003(6)	0.006(6)	0.018(3)
O2	1.661(2)	-0.485(2)	-0.389(1)	1	0.013(7)	0.024(7)	0.024(7)	0.012(6)	0.010(6)	0.006(6)	0.018(3)
O3	1.281(2)	0.144(2)	-0.548(1)	1	0.011(7)	0.031(8)	0.038(9)	0.013(7)	0.010(6)	0.012(7)	0.025(3)
O4	1.311(2)	-0.429(2)	-0.133(1)	1	0.005(7)	0.07(1)	0.025(8)	0.013(8)	0.005(6)	0.013(7)	0.035(4)
O5	1.242(2)	-0.123(2)	-0.425(1)	1	0.006(7)	0.032(8)	0.041(9)	0.019(7)	0.010(6)	0.010(6)	0.024(3)
O6	1.544(2)	-0.787(2)	-0.315(1)	1	0.024(8)	0.024(8)	0.037(9)	0.006(7)	0.001(7)	0.004(7)	0.031(4)
O7	1.667(2)	-0.426(2)	-0.133(1)	1	0.027(9)	0.039(9)	0.029(9)	0	0.007(7)	0.012(7)	0.034(4)
O8	1.155(2)	-0.791(2)	-0.317(1)	1	0.029(9)	0.04(1)	0.05(1)	0.009(7)	0.018(7)	0.009(7)	0.038(5)
O9	0.921(2)	-0.587(2)	-0.231(1)	1	0	0.06(1)	0.05(1)	0.015(8)	0.014(7)	0.016(7)	0.036(4)

OH10	1.585(2)	-0.186(2)	0.041(1)	1	0.015(8)	0.05(1)	0.012(7)	-0.004(7)	-0.002(6)	0.016(7)	0.030(4)
OH11	1.542(2)	-0.162(2)	-0.180(1)	1	0.020(8)	0.05(1)	0.031(8)	0.012(7)	0.007(7)	0.024(7)	0.033(4)
OW12	0.926(2)	0.230(2)	-0.018(1)	1	0.018(8)	0.06(1)	0.032(8)	0.022(8)	0.018(7)	0.023(7)	0.030(4)
OW13	1.046(2)	-0.113(2)	-0.191(1)	1	0.024(9)	0.06(1)	0.031(9)	0.001(8)	0.005(7)	0.021(8)	0.040(4)

Table 3-7. Interatomic distances (Å) in nolzeite.

NaO_4(OH)$(H_2O)_2$ Polyhedron			*Si*(1)O_4 Tetrahedron		
Na	-OW12	2.26(2)	*Si*1	-O5	1.61(1)
	-O3	2.28(2)		-O3	1.66(1)
	-OW13	2.42(2)		-O8	1.69(1)
	-O9	2.50(2)		-O6	1.69(1)
	-O6	2.55(2)	<*Si*1	-O>	1.66
	-OH11	2.63(2)			
	-O8	2.69(2)	*Si*(2)O_4 Tetrahedron		
<*Na*	-O>	2.48	*Si*2	-O7	1.60(1)
				-O2	1.62(1)
Mn(1)$O_5(H_2O)$ Octahedron				-O6	1.62(1)
*Mn*1	-O5	2.16(1)		-O9	1.67(1)
	-O1	2.22(1)	<*Si*2	-O>	1.63
	-O3	2.23(1)			
	-O1	2.27(1)	*Si*(3)O_4 Tetrahedron		
	-OW13	2.27(1)	*Si*3	-O4	1.62(1)
	-O2	2.31(1)		-O8	1.62(1)
<*Mn*1	-O>	2.24		-O1	1.62 (1)
				-O9	1.67(1)
Mn(2)O_5(OH) Octahedron			<*Si*3	-O>	1.63
*Mn*2	-O5	2.17(1)			
	-O3	2.21(1)	*B*$O_2(OH)_2$ Tetrahedron		
	-O2	2.21(1)	*B*	-OH10	1.32(4)
	-O1	2.25(1)		-O4	1.55(3)
	-O2	2.30(1)		-OH11	1.59(3)
	-OH11	2.31(1)		-O7	1.61(3)
<*Mn*2	-O>	2.24	<*B*	-O>	1.52

Table 3-8. Bond-valence table (*v.u.*) for nolzeite.

	Na	Mn(1)	Mn(2)	Si(1)	Si(2)	Si(3)	B	Σ
O1		$0.577^{\downarrow\rightarrow}$	$0.281^{\downarrow\rightarrow}$			$1.027^{\downarrow\rightarrow}$		1.885
O2		$0.246^{\downarrow\rightarrow}$	$0.565^{\downarrow\rightarrow}$		$1.022^{\downarrow\rightarrow}$			1.833
O3	$0.273^{\downarrow\rightarrow}$	$0.308^{\downarrow\rightarrow}$	$0.313^{\downarrow\rightarrow}$	$0.898^{\downarrow\rightarrow}$				1.792
O4						$1.050^{\downarrow\rightarrow}$	$0.706^{\downarrow\rightarrow}$	1.756
O5		$0.347^{\downarrow\rightarrow}$	$0.348^{\downarrow\rightarrow}$	$1.061^{\downarrow\rightarrow}$				1.756
O6	$0.138^{\downarrow\rightarrow}$			$0.793^{\downarrow\rightarrow}$	$1.027^{\downarrow\rightarrow}$			1.958
O7					$1.093^{\downarrow\rightarrow}$		$0.692^{\downarrow\rightarrow}$	1.785
O8	$0.094^{\downarrow\rightarrow}$			$0.819^{\downarrow\rightarrow}$		$0.989^{\downarrow\rightarrow}$		1.902
O9	$0.156^{\downarrow\rightarrow}$				$0.869^{\downarrow\rightarrow}$	$0.905^{\downarrow\rightarrow}$		1.93
OH10							$0.968^{\downarrow\rightarrow}$	0.968
OH11	$0.104^{\downarrow\rightarrow}$		$0.254^{\downarrow\rightarrow}$				$0.576^{\downarrow\rightarrow}$	0.934
OW12	$0.302^{\downarrow\rightarrow}$							0.302
OW13	$0.186^{\downarrow\rightarrow}$	$0.273^{\downarrow\rightarrow}$						0.459
Σ	1.253	1.751	1.761	3.571	4.011	3.971	2.942	

* Bond valences for other sites determined using parameters from Brese and O'Keeffe (1991).

Table 3-9. Paragenetic sequence for nolzeite and other minerals in vugs in a single xenolith at Mont Saint-Hilaire, Quebec, Canada.

Mineral	Time
Microcline	
Aegirine	
Eudialyte	
Analcime	
Sodalite	
Pyrrhotite	
Serandite	
Steedeite	
Nolzeite	
UK80	
Catapleiite	
Natrite /thermonatrite	

Chapter 4

Franconite, $NaNb_2O_5(OH)\bullet 3H_2O$: Structure determination and the role of H-bonding, with comments on the crystal-chemistry of franconite-related minerals

4.1 Abstract

The crystal structure of franconite, $NaNb_2O_5(OH)\bullet 3H_2O$, has been characterized by single-crystal X-ray diffraction using material from Mont Saint-Hilaire, Québec, Canada. Results give a = 10.119(2) b = 6.436(1) c = 12.682(2) Å and β = 99.91(3) ° and confirm the correct space group as $P2_1/c$. The crystal structure, refined to R = 4.63 % and wR^2 =11.95 %, contains one *Na* site, two distorted octahedral *Nb* sites, and nine *O* sites. It consists of clusters of four edge-sharing $Nb(O,OH)_6$ octahedra, linked through shared corners to adjacent clusters, forming layers of $Nb(O,OH)_6$ octahedra. These alternate along [100] with layers composed of $NaO(H_2O)_4$ polyhedra, the two being linked together by well-defined hydrogen bonding. The predominance of H-bonding, essential to the mineral, results in a perfect {100} cleavage. Chemical analyses (n = 7) of four crystals give the empirical formula $(Na_{0.73}Ca_{0.13}\square_{0.14})_{\sum=1.00}(Nb_{1.96}Ti_{0.02}Si_{0.02}Al_{0.01})_{\sum=2.01}O_5(OH)\bullet 3H_2O$ (based on 9 oxygens) or ideally $NaNb_2O_5(OH)\bullet 3H_2O$. Franconite is crystallo-chemically related to SOMS [Sandia Octahedral Molecular Sieves; $Na_2Nb_{2-x}M_xO_{6-x}(OH)_x\bullet H_2O$ with M = Ti, Zr, Hf], a group of synthetic compounds with strong ion exchange capabilities. Both hochelagaite ($CaNb_4O_{11}\bullet nH_2O$) and ternovite ($MgNb_4O_{11}\bullet nH_2O$) have X-ray powder diffraction patterns and cation ratios similar to those of franconite indicating that these minerals likely have similar structures.

4.2 Introduction

Franconite, $NaNb_2O_5(OH)•3H_2O$, is the Na-dominant end-member of a ternary system with other hydrated Nb-oxides including hochelagaite ($CaNb_4O_{11}•nH_2O$; Jambor *et al*. 1986) and ternovite ($MgNb_4O_{11}•nH_2O$; Subbotin *et al*. 1997). The mineral was first discovered at the Francon quarry in the St-Michel district of Montreal, Québec where it occurs in vugs within dawsonite-bearing sills as white polycrystalline globules (average diameter ~ 0.15 mm) consisting of radiating, extremely thin, blades (average dimensions = 0.030 x 0.005 x 0.001 mm; Jambor *et al*. 1986). It has also been discovered in other agpaitic environments including Mont Saint-Hilaire (Horváth & Gault 1990), the Saint-Amable sill (Horváth *et al*. 1998), the Khibiny massif (Pekov & Podlesnyi 2004), the Vuoriyarvi alkaline-ultrabasic massif (Belovitskaya & Pekov 2004), and the Vishnevogorsk alkali complex (Nikandrov, 1990). In the original description, Jambor et al. (1984) gave a unit cell of a = 22.22(1), b = 12.857(5), c = 6.359(4) Å and β = 92.24(6) °. Data from chemical analyses indicated the ideal formula $Na_2Nb_4O_{11}•nH_2O$ (n = 8 - 9) but with variable Na:Ca ratios, as well as trace Ti, Al, Si, and Sr (Jambor *et al*. 1984). Quite likely, the variable Na:Ca ratios are a function of both franconite and hochelagaite being found together in the same complex globules, an observation made during this current study. The two minerals also have similar optical properties, making them indistinguishable megascopically (Jambor *et al*. 1986, Jambor *et al*. 1984).

To date, only X-ray powder diffraction (XRPD) studies have been completed on franconite as the small crystal size of the mineral has precluded analyses by typical single-crystal methods. As such, the true chemical formula and crystal structure of the mineral have largely remained unknown. With the introduction of extremely bright X-ray sources arising from a combination of rotating-anode generators coupled with multi-layer optics, incident-beam paths, and highly

sensitive detectors, it is now possible to study the crystal structures of minerals (Cooper & Hawthorne 2012) such as franconite. In this study we report on the results from a successful single crystal study of franconite, present a description of its structure and describe the complex nature of H-bonding within franconite, along with commenting on the significance of the crystal structure in the context of the chemical variation involving franconite and the related minerals, hochelagaite and ternovite. As franconite is a late-stage mineral occurring in many agpaitic environments, understanding of its crystal structure can also help to better understand processes related to the low-temperature alteration of Nb-rich minerals.

4.3 Occurrence and Description

The franconite used in this study was collected at the Poudrette quarry, La Vallée-du-Richelieu, Montérégie (formerly Rouville County), Québec, Canada, where is occurs as a rare mineral in sodalite syenite, miarolitic cavities, and hornfels microenvironments (Horvath & Gault 1990). The material used in this study came from sodalite syenite where it occurs in association with microcline, analcime, sodalite, siderite, and pyrite (Table 4-1). Franconite occurs in spherical aggregates of radiating bladed crystals that are ~ 0.15 – 0.20 mm in diameter. Individual crystals of franconite are on average 0.008 x 0.020 x 0.060 mm, euhedral, with a perfect {100} cleavage and display the forms pinacoid {100} and {011}.

4.4 Chemistry

Chemical analyses of franconite were made using a JEOL JSM 6400 scanning electron microscope using a voltage of 20 kV, a beam current of ~1 nA, and a beam width of 1 μm. Data from energy-dispersive spectrometry (EDS) were collected using the following standards (X-ray lines): $CaTiO_3$ (Ca*K*α, Ti*K*α), synthetic $MnNb_2O_6$ (Nb*K*α), and albite (Na*K*α, Si*K*α, Al*K*α). The

globules analyzed in this study were found to contain crystals of near end-member franconite, along with those with compositions intermediate between franconite and hochelagaite (*i.e.*, with variable Na:Ca ratios), and near end-member hochelagaite. None of the crystals appear to be chemically zoned when viewed perpendicular to the layering. Due to the variation of Na and Ca in the globules of franconite, fifteen separate crystals were isolated for chemical analysis. Of these, four were found to have franconite-rich compositions, with the remaining ones having either hochelagaite-rich or intermediate franconite-hochelagaite compositions. Chemical analyses (n = 7) of the four franconite-rich crystals give the average (range) composition (wt.%): Na_2O 6.45 (5.03 – 8.87), CaO 2.00 (0.34 – 3.27), Nb_2O_5 74.23 (72.50 – 75.43), TiO_2 0.52 (0.40 – 0.75), SiO_2 0.42 (0.27 – 0.81), Al_2O_3 0.11 (0.04 – 0.27) and H_2O (calc.) 17.96, and total = 101.69, corresponding to the empirical formula: $(Na_{0.73}Ca_{0.13}\square_{0.14})_{\sum=1.00}$ $(Nb_{1.96}Ti_{0.02}Si_{0.02}Al_{0.01})_{\sum=2.01}O_5(OH) \bullet 3H_2O$ (based on 9 oxygens) or ideally $NaNb_2O_5(OH)\bullet 3H_2O$. Although the *Na* site was determined to be fully occupied in the crystal structure refinement, the empirical formula indicates a minor deficiency in *Na* site, a feature that may be explained by the instability of the mineral and possible migration of Na under the electron beam. The ideal formula originally proposed for franconite by Jambor *et al*. (1984) was $Na_2Nb_4O_{11}\bullet nH_2O$, determined on the basis of ΣNb+Ti+Si+Al = 4, as the nature of the anions was unclear. The ideal formula proposed in this present contribution is derived from results of the crystal-structure analysis and to a greater extent, more clearly defines the content and roles of (OH) and H_2O in the mineral. In light of the obvious chemical variation that may exist in franconite, data from wavelength-dispersive spectrometry (WDS) were also collected on the crystal used for the single-crystal X-ray structure study. These were obtained using a Cameca SX-100 electron microprobe operated with an excitation voltage of 15 kV, 5 nA current, and a 15

μm beam width (chosen to reduce migration of Na). The following standards (X-ray lines) were used: albite (Na*K*α), olivine (Mg*K*α), diopside (Ca*K*α, Si*K*α), andalusite (Al*K*α), titanite (Ti*K*α), $Ba_2NaNb_5O_{15}$ (Nb*K*α), and $SrTiO_3$ (Sr*K*α). The compositions of two points taken from the crystal used for single crystal analysis are similar to those presented above, confirming the data obtained by energy-dispersive spectrometry. Data from the two data points obtained by WDS give the average composition of: Na_2O 7.60, CaO 0.35, Nb_2O_5 75.05, TiO_2 0.61, SiO_2 0.02, Al_2O_3 0.03, and H_2O (calc.) 16.31 total 100 %.

Other elements were sought but were not found to be present in statistically meaningful concentrations. In particular, data from EDS and WDS indicate franconite is devoid of Ta, an interesting observation considering the strong geochemical coupling behaviour between Nb and Ta (Babechuk & Kamber 2011). Both Nb and Ta have share crystal-chemical similarities such as identical charges (3+, 5+) as well as similar ionic radii (~ 0.64 Å for $^{[6]}Nb^{5+}$ and $^{[6]}Ta^{5+}$; Shannon et al. 1976), so would be predicted to substitute readily for one another in crystal structures. Niobium-bearing minerals such as vuonnemite $[Na_{11}Ti^{4+}Nb_2(Si_2O_7)_2(PO_4)_2O_3(F,OH)$; Ercit *et al*. 1998], epistolite $[Na_4Nb_2Ti^{4+}(Si_2O_7)_2O_2(OH)_2(H_2O)_4$; Sokolova & Hawthorne 2004], and laurentianite $\{[NbO(H_2O)]_3(Si_2O_7)_2[Na(H_2O)_2]_3$; Haring *et al*. 2012} from alkaline environments similar to those that fanconite forms in, also exhibit a virtual absence Ta. These observations may suggest a possible fractionation between Nb and Ta occurring prior to the formation of these minerals, which would also hold for franconite. The exact cause of the Nb-Ta decoupling mechanism remains unknown, but given that it is observed in Nb-bearing minerals from a number of agpaitic environments, the implication is that it must be related to the geochemical processes leading to the formation of these unusual lithologies.

4.5 Raman and Infrared Spectroscopy

Raman and infrared spectroscopy of franconite was carried out to investigate the presence of OH and H_2O. The Raman spectrum of franconite was collected using a Horiba Jobin Yvon XPLORA Raman spectrometer interfaced with an Olympus BX41 microscope over a range of 50 to 4000 cm^{-1}. The spectrum (Fig. 4-1) represents an average of three spectra, each collected with a 20 s acquisition cycles. An excitation radiation of λ = 638 nm was used, along with a 600 grating and 100 x magnification (producing a beam of diameter = 2 μm). The excitation radiation of λ = 638 nm was chosen to eliminate fluorescence peaks in the region of ~ 2000 to 2500 cm^{-1} which were observed when spectra were collected using λ = 532 nm. Calibration was made using the 521 cm^{-1} line of a silicon wafer. The Raman spectrum of franconite contains bands in two regions: at ~ 212 - 924, and 3416 cm^{-1} (Fig. 4-1). The first consists of sharp, moderate to high intensity peaks at 212, 297, 391, 461, 583, 661, 879, and 924 cm^{-1}. Those peaks occurring below 500 cm^{-1} are associated with Na-O/Ca-O bonding (Table 4-2). The remaining high intensity peaks are attributed to the two distinct distorted octahedral sites associated with Nb (see below). Those peaks attributed to Nb-O were assigned based on data on Nb-oxides presented by Jehng & Wachs (1990). Peaks at 583 and 661 cm^{-1} are attributed to symmetric stretching of the Nb-O-Nb linkages associated with two crystallographically independent $Nb(O,OH)_6$ octahedra (Fig. 5-1). The peaks at 879 and 924 cm^{-1} are attributed to symmetric stretching of possible Nb=O bonds present in the distorted $Nb(O,OH)_6$ sites (Jehng & Wachs 1990). The final Raman band is a single, broad, low intensity peak at 3416 cm^{-1} associated with O-H stretching (Williams 1995). The Raman spectra of the synthetic phases $HCa_2Nb_3O_{10}$ and $KCa_2Nb_3O_{10}$ (Jehng & Wachs 1990) as well as those of SOMS [Sandia Octahedral Molecular Sieves; $Na_2Nb_{2-x}M_xO_{6-x}(OH)_x \bullet H_2O$ with *M* = Ti, Zr, Hf; Nyman *et al*. 2001, Nyman *et al*. 2002,

Iliev *et al*. 2003], are similar to that of franconite. The spectra of the synthetic phases both have a single, moderately strong Raman band in the region of ~ 750 – 800 cm^{-1}, associated with symmetric stretching of Nb=O bonds, as well as two moderately strong Raman bands in the region of 450 – 650 cm^{-1}, associated with Nb-O-Nb linkages from two crystallographically independent NbO_6 sites (Jehng & Wachs 1990). In the region 1200 – 1700 cm^{-1}, bands associated with H-O-H stretching could not be detected using Raman spectroscopy probably because of the weak Raman scattering abilities of water.

To confirm the presence of water in franconite and in light of the fact that water is a weak Raman scatterer but a strong absorber of infrared radiation, an infrared (FTIR) spectrum over the range of 600 to 4000 cm^{-1} was collected using a Bruker Alpha spectrometer equipped with a KBr beam splitter and a DTGS detector. This spectrum, obtained by averaging 128 scans with a resolution of 4 cm^{-1}, reveals four distinct bands at ~ 677 cm^{-1}, 874 - 1028 cm^{-1}, 1658 cm^{-1}, and 3204 - 3422 cm^{-1}. Overall, the spectrum is similar to that reported by Jambor et al. (1984) and with the exception of an additional band in the region of 1658 cm^{-1}, the FTIR and Raman spectra of franconite are identical. The first two regions at ~ 677 cm^{-1} and 874 - 1028 cm^{-1} are similar to those in the Raman spectrum at 563, 646, 815, and 877 cm^{-1}; these are attributed to the symmetric stretching of Nb-O-Nb and vibrations of terminal Nb=O bonds, respectively (Table 4-3; Fielicke *et al*. 2002). The third region, centered at ~ 1658 cm^{-1}, consists of a strong band at ~ 1658 cm^{-1} with a shoulder at ~ 1617 cm^{-1} and is attributed to H-O-H bending (Williams 1995). The fourth region, at ~ 3204 - 3422 cm^{-1}, is consistent with the weak Raman band at 3303 cm^{-1} and consists of a strong band at ~3356 cm^{-1} with shoulders at ~3204 and ~ 3422 cm^{-1} and is associated with O-H bending. A similar FTIR spectrum is observed for ternovite

$(Mg,Ca)Nb_4O_{11}•nH_2O$ (Subbotin *et al*. 1997), implying the mineral has crystal-chemical properties similar to those of franconite.

4.6 X-ray Crystallography and Crystal-Structure Determination

X-ray powder diffraction data were collected using a 114.6 mm diameter Gandolfi camera, 0.3 mm collimator, and Fe-filtered Co*K*α radiation (λ = 1.7902 Å). Intensities were determined using a scanned image of the powder pattern and normalized to the measured intensity of d = 9.968 Å (I = 100). To determine how much an *hkl* plane contributed to a reflection, the measured intensities were compared to a pattern calculated using results from the crystal-structure analysis and the program CRYSCON (Dowty 2002). Overall, there is a good agreement between the measured and calculated powder patterns (Table 4-4). The XRPD data for franconite in this study are broadly similar those of Jambor et al. (1984); however, the highest intensity line in this study occurs at a *d*-spacing of ~ 10 Å rather than ~ 11 Å as observed by Jambor *et al*. (1984). X-ray powder diffraction data from desiccated franconite ($Na_2Nb_4O_{11}•3H_2O$) collected by Jambor et al. (1984) showed a strong line occurring at a *d*-spacing of ~10 Å, similar to franconite in this study. Subsequent re-runs of the desiccated franconite over a two-year resulted in XRPD data showing a doublet at a *d*-spacing of ~ 10-11 Å due to a gradual rehydration of franconite (Jambor *et al*. 1984). These differences in hydration state may explain why the highest intensity line for franconite from this study and that given by Jambor *et al*. (1984) have different *d*-spacings.

To obtain a crystal for the next stage of the study, individual crystals were separated from a coarse-grained, franconite-bearing globule. These were examined optically and one of dimensions 0.08 x 0.02 x 0.01 mm, exhibiting a simple extinction and no evidence for twinning,

was selected. X-ray intensity data were collected on a Bruker D8 three-circle diffractometer equipped with a rotating-anode generator, multi-layer optics incident beam path and an APEX-II CCD detector. X-ray diffraction data (28653 reflections) were collected to 60° 2θ using 20 s per 0.3° frame and with a crystal-to-detector distance of 5 cm. The unit-cell parameters for franconite, obtained by least-squares refinement of 19947 reflections ($I > 10\sigma I$), are a = 10.119(2) b = 6.436(1) c = 12.682(2) Å and β = 99.91(3) ° (Table 4-5). The original unit cell [a = 22.22(1), b = 12.857(5), c = 6.359(4) Å and β = 92.24(6) °] determined by Jambor et al. (1984) was obtained by electron diffraction and indexing of a XRPD pattern, as a result the weak reflections supporting the halving of the unit cell along the *a*-axis may have been missed. An empirical absorption correction (SADABS; Sheldrick, 1997) was applied and equivalent reflections merged to give 28634 unique reflections covering the entire Ewald sphere.

Solution and refinement of the crystal structure of franconite were done using SHELXL – 97 (Sheldrick 1997). The crystal structure was solved using direct methods, using the scattering curves of Cromer & Mann (1968) and the scattering factors of Cromer & Liberman (1970). Phasing of a set of normalised structure factors gave a mean value of $|E^2 - 1|$ value of 0.912, consistent with a centre of symmetry being present {$|E^2 - 1| = 0.968$ for centrosymmetric and $|E^2 - 1| = 0.736$ for non-centrosymmetric}. Based on this and the space-group choices available, $P2_1/c$ (#14) was chosen as the correct space group. Phase-normalised structure factors were used to give a Fourier difference map from which two *Nb*, and several *O* sites were located. The *Na* site and additional *O* sites were identified from subsequent Fourier difference maps. Refinement of the site-occupancy factors (SOF) indicated that all of the cation and anion sites were fully occupied (Table 4-6). Determination of which *O* sites were occupied by OH or H_2O

was based on bond-valence calculations and electroneutrality considerations (Table 4-7). During the later stages of refinement, seven *H* sites were located in the difference Fourier maps. These were inserted into the refinement with H-O distances being constrained to be close to 0.98 Å. Refinement of this model converged to R = 4.63 % and wR^2 = 11.95 %.

4.7 Description of Crystal Structure

The crystal structure of franconite has one five-coordinated *Na* site bonded to four H_2O groups and a single O atom, producing an $NaO(H_2O)_4$ polyhedron. This is unusual in rock forming minerals, in that Na typically occurs in [6] or higher. However, in rare instances it can occur in [5] as in zeravshanite [$Cs_4Na_2Zr_3(Si_{18}O_{45})(H_2O)_2$; Uvarova *et al*. 2004] and mejillonesite [$NaMg_2(PO_3OH)(PO_4)(OH)\bullet H_5O_2$; Atencio *et al*. 2012] and even as low as [4], as in vuonnemite [$(Na_{11}TiNb_2(Si_2O_7)_2(PO_4)_2O_3(F,OH)$; Ercit *et al*. 1998)]. Average Na-O bond lengths in zeravshanite and mejillonesite are 2.400 and 2.396 Å, respectively, with bond lengths for both minerals ranging from 2.275(5) to 2.615(4) Å. In franconite, Na-(O,H_2O) bond lengths range from 2.337(6) to 2.422(7) Å with an average bond length of 2.390 Å (Table 4-8), in good agreement with those observed for $^{[5]}$Na in zeravshanite and mejillonesite.

The crystal structure also contains two *Nb* sites in octahedral coordination with O atoms and OH groups: $Nb(1)O_5(OH)$ and $Nb(2)O_4(OH)_2$ (Fig. 4-3). Both are highly distorted with Nb-(O,OH) bond lengths ranging from 1.748(5) to 2.384(4) Å and 1.823(4) to 2.256(4) Å respectively (Table 4-8). The $Nb(1)O_5(OH)$ octahedron has four equatorial bond lengths of ~ 2 Å as well as two asymmetrical apical bonds: a short one of 1.746(5) Å and a long one of 2.383(4) Å, the former possibly representing a Nb-O double bond (Jehng & Wachs 1990). This type of octahedron is unusual in naturally occurring minerals; however, similar octahedra are known to occur in

nenadkevichite (Rastsvetaeva *et al*. 1994), vuonnemite (Ercit *et al.* 1998), epistolite (Sokolova & Hawthorne 2004), and laurentianite (Haring *et al.* 2012). The $Nb(2)O_4(OH)_2$ octahedron has three pairs of equivalent bonds: two short bonds with lengths of 1.823(4) and 1.829(4) Å, two long bonds with lengths of 2.217(4) and 2.256(4) Å, and two bonds of intermediate lengths of 1.988(4) and 1.990(4) Å. This second type of octahedra is very rare in naturally occurring minerals and has only been reported in nacareniobsite-(Ce) [$Na_3Ca_3REENb(Si_2O_7)_2OF_3$; Sokolova & Hawthorne 2008]. In both $Nb\varphi_6$ (φ = O, OH, H_2O) octahedra, the longest bond lengths correspond to Nb-OH bonds whereas the shortest bond lengths correspond to Nb-O bonds, the short distances likely reflecting the presence of double bonds. When in octahedral coordination, small highly charged cations such as Nb^{5+} often cause significant O-O repulsion which leads to strain on O-M-O bonds (Megaw 1968 a, b). To reduce this strain, the Nb^{5+} cation will undergo an off-center displacement resulting in distorted octahedra with large ranges in bond length. These large ranges in Nb-(O,OH) bond length are consistent with those observed in the $Nb(O,OH)_6$ present in the crystal structure of franconite.

The limited number of cation polyhedra present constrains the bond topology in franconite to being relatively simple. First, the $Nb(1)O_5(OH)$ and $Nb(2)O_4(OH)_2$ octahedra are linked through shared edges to form four-membered clusters consisting of two $Nb(1)O_5(OH)$ and two $Nb(2)O_4(OH)_2$ octahedra (Fig. 4-4). Each four-membered $Nb(O,OH)_6$ cluster is subsequently linked to six adjacent clusters through shared corners, thus forming infinite sheets parallel to [100] (Fig. 4-4). This strongly affects the morphology of the crystals, which are platy and flattened on {100}. The $Na(O,H_2O)_5$ polyhedra are linked through shared corners to form single chains parallel to [100] (Fig. 4-5). These chains of $NaO(H_2O)_4$ polyhedra form distinct layers

which alternate with layers of $Nb(O,OH)_6$ octahedra along [100]. Each $NaO(H_2O)_4$ polyhedral layer is weakly linked to sheets of $Nb(O,OH)_6$ octahedra through shared O(5) anions and more importantly H-bonds (Fig. 4-6), which are discussed below.

The crystal structure of franconite is quite interesting in light of the well-defined H-bonding that is essential to completing the crystal structure. There are three H_2O groups [OW(7), OW(8), and OW(9)] and one OH [OH(6)] group present in the crystal structure. The H-bonds associated with the OH and H_2O groups are separated into two groups: 1) those *within* Na-Nb polyhedral layers and 2) those *between* the Na-Nb polyhedral layers. The first group of H-bonds are restricted to the $NaO(H_2O)_4$ polyhedral layer. These involve H(4) and H(7) that are bonded to the OW(8) and OW(9) groups, respectively, and project towards adjacent chains of $NaO(H_2O)_4$ polyhedra (Fig. 4-7). Each H(4) is located ~ 1.94 Å from O(5) atoms while each H(7) is located ~ 1.91 Å from OW8 groups generating hydrogen bonds between adjacent $NaO(H_2O)_4$ polyhedral chains within the $NaO(H_2O)_4$ polyhedral layer.

The second group, which includes three sets of H-bonds, occur between layers of $NaO(H_2O)_4$ polyhedra and $Nb(O,OH)_6$ octahedra. The bonds in each set share similar orientations with respect to one another. The first set involves H(1) that is bonded to OH(6) [coordinated with $Nb(O,OH)_6$ octahedra]. Each H(1) projects towards the $NaO(H_2O)_4$ polyhedral layer and is located ~ 1.87 Å from OW7 [coordinated with $NaO(H_2O)_4$ polyhedra], forming a hydrogen bond between the $Nb(O,OH)_6$ octahedral layer and the $NaO(H_2O)_4$ polyhedral layer (Fig. 4-8a). The second set of H-bonds involves H(2) and H(3) that are bonded to OW(7), both projecting towards the $Nb(O,OH)_6$ octahedral layer. Each H(2) is located ~1.90 Å from O(1) atoms while

each H(3) is located ~ 1.93 Å from O2, generating additional hydrogen bonds between the $NaO(H_2O)_4$ and $Nb(O,OH)_6$ layers (Fig. 4-8b). The third set of interlayer hydrogen bonds involves H(5) and H(6) that are bonded to OW(8) and OW(9) groups, respectively. Both H(5) and H(6) project from the $NaO(H_2O)_4$ layers towards the $Nb(O,OH)_6$ layers. Each H(5) is located ~1.82 Å from O(2) atoms while H(6) is located ~1.92 Å from O(1), both generating the remaining H-bonds between the $NaO(H_2O)_4$ and $Nb(O,OH)_6$ layers (Fig. 4-8c). The second group of interlayer H-bonds involve H(1), H(2), H(3), H(5), and H(6) and these play a critical role in the crystal structure of franconite. The predominance of H-bonding serves to link the $Na(O,H_2O)_5$ and $Nb(O,OH)_6$ layers, thereby completing the crystal structure of the mineral, and also leads to the perfect [100] cleavage observed in franconite.

4.8 Related Structures

The crystal structure of franconite is broadly similar to those of the synthetic compounds $Na_2Nb_4O_{11}$ (Masó *et al*. 2011) and $KCa_2Nb_3O_{10}$ (Fukoka *et al*. 2000, Jehng & Wachs 1990) as well as SOMS (Nyman *et al*. 2001, 2002). Both $Na_2Nb_4O_{11}$ and $KCa_2Nb_3O_{10}$ have been synthesized at high *T* (~1100 – 1300 °C) and have distinct ferroelectric and dielectric properties, making them useful in constructing ferroelectric capacitors (Masó *et al.* 2011, Yim *et al*. 2013). From a crystal-structure perspective, both $Na_2Nb_4O_{11}$ and $KCa_2Nb_3O_{10}$ are constructed of alternating Nb polyhedral and (Na, K) polyhedral layers similar to those in franconite, but with bond topologies that differ from those of franconite. Synthetic $Na_2Nb_4O_{11,}$ like franconite, is monoclinic but it crystallizes in the space group *C*2/*c*. It has two unique *Nb* sites, but unlike those in franconite, one occurs as NbO_7 bipyramids, with <Nb-O> is 2.0570 Å and Nb-O bonds ranging from 1.9638(10) to 2.4136(21) Å (Masó *et al*. 2011). The second occurs as in NbO_6

octahedra with six identical Nb-O bonds of 1.9943(10) Å (Masó *et al*. 2011). As in franconite, the crystal structure of $Na_2Nb_4O_{11}$ is layered, with layers of edge-sharing NbO_7 bipyramids alternating along [001] with mixed layers containing both of NbO_6 octahedra and NaO_7 polyhedra (Masó *et al*. 2011). This differs from the crystal structure of franconite wherein the $Nb(O,OH)_6$ octahedra and $NaO(H_2O)_5$ polyhedra occupy distinct layers within the crystal structure. The crystal structure of $KCa_2Nb_3O_{10}$, unlike franconite, is orthorhombic with *Cmcm* space-group symmetry. This compound is described as having a layered perovskite structure with distinct layers of $^{[6]}$Nb. There are two *Nb* sites in the crystal structure, both being [6]-coordinated by O in NbO_6 octahedra, rather than the $Nb(O,OH)_6$ octahedra found in franconite. The *Nb* sites in $KCa_2Nb_3O_{10}$ have Nb-O bond lengths similar to those observed in franconite. The first is similar to the $Nb(2)O_4(OH)_2$ octahedron in franconite, with three pairs of equivalent bonds: two short bonds both with lengths of 1.989(3) Å, two long bonds both with lengths of 2.024(4) Å, and two bonds with an intermediate length of 1.905(7) Å (Fukoka *et al*. 2000). The second is similar to the $Nb(1)O_5(OH)$ octahedron in franconite, consisting of a short Nb-O bond of 1.748(6) Å, a long Nb-O bond of 2.389(7) Å, as well as four equatorial bonds (Fukoka *et al*. 2000). Furthermore, the NbO_6 octahedral layers in $KCa_2Nb_3O_{10}$ are the result of NbO_6 octahedra linked to adjacent NbO_6 octahedra through shared corners. These layers of NbO_6 layers contain interstitial Ca^{2+} cations and alternate with layers of KO_7 polyhedra (Fukoka *et al*. 2000).

SOMS, unlike $Na_2Nb_4O_{11}$ and $KCa_2Nb_3O_{10,}$ can be synthesized at low temperatures (T ~ 175 °C) under alkaline conditions (pH ~ 13.7; Xu *et al*. 2004). Franconite is expected to have formed under similar conditions based on its hydrous crystal structure (see discussion below) and association with carbonate minerals such as siderite and calcite (this study, Jambor *et al*. 1984).

SOMS exhibit a strong ion-exchange selectivity for divalent cations over monovalent cations making them useful in removing heavy metals such as Pb^{2+},Co^{2+} and Cd^{2+} from ground water and soils (Nyman *et al*. 2001). Nb-dominant SOMS [$Na_2Nb_2O_6 \bullet H_2O$; Nyman *et al*. 2001] are hydrated and have crystal structures with cation ratios similar to those of franconite. The crystal structure of Nb-dominant SOMS, like franconite, is monoclinic but it crystallizes in the space group *C*2/*c* (Nyman *et al*. 2001). It consists of sheets of edge-sharing $Na(O,H_2O)_6$ octahedra (Nyman *et al*. 2001) instead of chains of corner sharing $Na(O,H_2O)_5$ polyhedra, as is observed in franconite. These sheets of edge-sharing $Na(O,H_2O)_6$ octahedra alternate with layers containing double chains of NbO_6 octahedra with $Na(O,H_2O)_4$ polyhedra (Nyman *et al*. 2001) occurring between the double chains. The NbO_6 sites in SOMS, are similar to the $Nb(1)O_5(OH)$ sites in franconite, with a short apical bond of ~1.8 Å, a long one of ~ 2.4 Å as well as four equatorial bonds with distances of ~ 2 Å (Nyman *et al*. 2002).

Although their crystal structures have not yet been determined, those of ternovite and hochelagaite are expected to be related to that of franconite based on the similarity in their XRPD patterns and cationic ratios. This implies that despite differences in chemistry amongst the three minerals, the structure type that is common to all three must be considered to be highly flexible, at least in terms of alkalis and alkaline-earths that may be accommodated. Chemical data from franconite, hochelagaite and ternovite (Fig. 4-9) indicate that a nearly complete solid solution exists between franconite and hochelagaite; if one assumes similar stoichiometries for the two, it is presumable that the Ca-Na substitution involves generation of vacancies or the conversion of O to OH (e.g. $Ti^{4+} + OH^- \leftrightarrow Nb^{5+} + O^{2-}$ substitution in SOMS; Nyman *et al*. 2001) in order to maintain charge-balance. In the crystal-structure refinement of franconite, the *O* and

OH sites were found to be fully occupied. Furthermore, chemical data (n = 35) from five franconite-rich globules show a strong, inverse ~2:1 correlation between Na and Ca in terms of atoms per formula unit (APFU) (Fig. 4-10), while similar trends involving substitutions with other elements (*e.g.*, Nb, Ti, Al and Si) are not evident. As such, it is probable that the Na-Ca substitution is a coupled substitution linked to the creation of vacancies, *i.e.*, $2Na^{+} \leftrightarrow Ca^{2+} + \square$. From preliminary studies, it also appears that the unidentified mineral UK56 (Chao *et al*. 1990) $[(Ca_{0.5}\square_{0.5})Nb_2O_5(OH)\bullet 4H_2O]$ has a crystal structure and bond topology very similar to that of franconite. In this mineral, vacancies due to Ca-Na substitution are observed where the alkali-/alkali-earth site is only half-occupied by Ca instead of being fully occupied by Na as in franconite (*unpub*. *data*). An analysis of the chemical data available for minerals of the franconite-hochelagaite-ternovite ternary system indicates limited substitution of Mg^{2+} and Ca^{2+}. While the radii for $^{[6]}Ca^{2+}$ (1.00 Å) and $^{[6]}Mg^{2+}$ (0.72 Å) (Shannon 1976) suggest that any Ca ↔ Mg substitution should be limited on an ionic-radius basis, the true extent of this substitution is not known, primarily due to the paucity of data related to the chemistry of ternovite. Since the crystal structures of ternovite, hochelagaite and franconite are expected to be related, the presence of ternovite containing both Ca^{2+} and Mg^{2+} further supports the flexibility of the franconite structure. Given the difference in ionic radii between $^{[6]}Na^{+}$ (1.02 Å) and $^{[6]}Mg^{2+}$ (0.72 Å), as well as the charge difference, substitution between Na^{+} and Mg^{2+} would likely be very limited. Although such a substitution is indicated on the franconite-hochelagaite-ternovite ternary, it is only supported by a single data point representing a Na-Mg-Ca solid solution as such the true extent of Na ↔ Mg substitution in franconite remains uncertain. Considering the crystal-chemical flexibility of the structure type that is common to franconite, hochelagaite, and ternovite, it is more probable that the composition of the individual phase that crystallizes is most

dependent on the composition of the fluids from which it is crystallizing. As such, the potential for Fe^{2+}- as well as K^{+}-rich compositions of franconite must be considered high.

The crystal structure of franconite is also highly flexible with respect to water content. Electron microprobe data from franconite used in this study indicates a calculated water content of 16.31 wt. %, compared to the water content of ~ 10 to 14 wt. % for franconite determined by Jambor *et al*. (1984). Since water loss can occur under the vacuum conditions used for microprobe analysis, Jambor *et al*. (1984) also measured the water content of franconite using a thermal analyzer. The results indicate that franconite can accommodate from three H_2O groups under dry conditions and up to 26 H_2O groups under humid conditions (Jambor *et al*. 1984). This wide variation in H_2O content suggests that H_2O in franconite can either be structurally bound or loosely bound, possibly adhering to the large surface areas present in franconite, not unlike the situation with many clays (Salles *et al*. 2009, Barshad 1952). Results indicate that the loosely bound water is readily expelled under dry or vacuum conditions, whereas part of the structurally bound water is released upon heating to 110 °C with the remainder being released upon heating to 356 °C (Jambor *et al*. 1984). The loss of the structurally bound water in franconite leads to a collapse in the crystal structure, as evidenced by the degradation of XRPD data collected on materials heated at 150, 250, 350, and 500 °C (Jambor *et al*. 1984). The phases present in X-ray patterns collected at 150, 250, and 350 °C could not be identified, but may correspond to $Na_2Nb_4O_{11}(H_2O)_n$ (n = 1; Jambor *et al*. 1984). Upon heating samples of franconite to 500 °C, X-ray patterns were found to be consistent with $Na_2Nb_4O_{11}$ (Jambor *et al*. 1984). Hydrogen bonds involving structurally bound water are essential in stabilizing the crystal structure of franconite. The structural collapse of the crystal structure of franconite at T as low as 150 °C, can probably

be ascribed to the loss of hydrogen bonds resulting from the loss of structurally bound water. This structural collapse may possibly begin at temperatures as low as 110 °C, as the release of structurally bound water starts at such *T*. Given the essential role of water in the crystal structure of franconite, it is likely that this mineral precipitated from aqueous fluids at low temperatures less than 110 °C. This is consistent with fluid inclusion studies by Schilling et al. (2011) that indicate the presence of late-stage fluids at Mont-Saint Hilaire that were trapped at temperatures lower than 340 °C.

4.9 References

Atencio, D., Chukanov, N.V., Nestola, F., Witzke, T., Coutinho, J.M.V., Zadov, A.E., Filho, R.R.C. and Färber, G. (2012): Mejillonesite, a new acid sodium, magnesium phosphate mineral, from Mejillones Antofagasta, Chile. American Mineralogist, 97, 19-25.

Babechuk, M.G. and Kamber, B.S. (2011): An estimate of 1.9 Ga mantle depletion using the high-field-strength elements and Nd–Pb isotopes of ocean floor basalts, Flin Flon Belt, Canada. Precambrian Research, 189, 114-139.

Barshad, I. (1952): Adorptive and swelling properties of clay-water system. Clays and Clay Minerals, 1, 70-77.

Belovitskaya, Y.V., and Pekov, I.V. (2004): Genetic mineralogy of the burbankite group. New Data on Minerals, 39, 50-64.

Brese, N.E. and O'Keefe (1991): Bond-valence parameters for solids. Acta Crystallographica, B47, 192-197.

Brown, I.D. and Altermatt, D. (1985): Bond-valence parameters obtained from a systematic analysis of the inorganic crystal structure database. Acta Crystallographica, B41, 244-247.

Chao, G.Y., Conlon, R.P. and Velthuizen, J. (1990): Mont Saint-Hilaire Unknowns. The Mineralogical Record, 21, 363-368.

Cooper, M.A. and Hawthorne F.C. (2012): The crystal structure of kraisslite, $^{[4]}Zn_3(Mn,Mg)_{25}(Fe^{3+},Al)(As^{3+}O_3)_2[(Si,As^{5+})O_4]_{10}(OH)_{16}$, from Sterling Hill mine, Ogdensburg, Sussex County, New Jersey, USA. Mineralogical Magazine, 76, 2819-2836.

Cromer, D.T. and Mann, J.B. (1968): X-ray scattering factors computed from numerical Hartree-Frock wave functions. Acta Crystallographica, A24, 321-324. ces, 44: 1333-1346.

Cromer, D.T. and Liberman, D. (1970): Relativistic calculation of anomalous scattering factors for X rays. Journal of Physics and Chemistry, 53, 1891-1898.

Dowty, E. (2002): CRYSCON for Windows and Macintosh Version 1.1. Shape Software Kingsport, Tennessee, USA.

Ercit, T.S., Cooper, M.A. and Hawthorne, F.C. (1998): The crystal structure of vuonnemite, $Na_{11}Ti^{4+}Nb_2(Si_2O_7)_2(PO_4)_2O_3(F,OH)$, a phosphate-bearing sorosilicate of the lomonosovite group. Canadian Mineralogist, 36, 1311-1320.

Fielicke, A., Meijer, G. and Von Helden, G. (2003): Infrared spectroscopy of niobium oxide cluster cations in a molecular beam: identifying the cluster structures. Journal of the American Chemical Society, 125, 3659-3667.

Fukoka, H., Isami, T. and Yamanaka, S. (2000): Crystal structure of a layered perovskite niobate $KCa_2Nb_3O_{10}$. Journal of Solid State Chemistry, 151, 40-45.

Haring, M.M.M., McDonald, A.M., Cooper, M.A., and Poirier, G.A. (2012): Laurentianite, $[NbO(H_2O)]_3(Si_2O_7)_2[Na(H_2O)_2]_3$, a new minreral from Mont Saint-Hilaire, Québec: description, crystal-structure determination and paragenesis. Canadian Mineralogist, 50, 1265-1280.

Horváth, L. and Gault, R.A. (1990): The mineralogy of Mont Saint-Hilaire Québec. Mineralogical Record, 21, 284-359.

Horváth, L., Pfenninger-Horváth, E., Gault, R.A. and Tarassoff, P. (1998): Mineralogy of the Saint-Amable Sill, Varennes and Saint-Amable, Québec. Mineralogical Record, 29, 83-118.

Iliev, M., Phillips, M.L.F., Meen, J.K. and Nenoff, T.M. (2003): Raman spectroscopy Na2Nb2O6•H2O and Na2Nb2-xMxO6-x(OH)x•H2O (M = Ti, Hf) ion exchangers. Journal of Physical Chemistry, B 107, 14261-14264.

Jambor, J.L., Sabina, A.P., Roberts, A.C., Bonardi, M., Ramik, R.R. and Sturman B.D. (1984): Franconite, a new hydrated Na-Nb oxide mineral from Montreal Island, Québec. Canadian Mineralogist, 22, 239-243.

Jambor, J.L., Sabina, A.P., Roberts, A.C., Bonardi, M., Owens, D.R. and Sturman, B.D. (1986): Hochelagaite, a new calium-niobium oxide mineral from Montreal, Québec. Canadian Mineralogist, 24, 449-453.

Jehng, J.M. and Wachs I.E. (1990): Structural chemistry and Raman spectra of niobium oxides. Chemistry of Materials, 3, 101-107.

Masó, N., Woodward, D.I., Várez, A. and West, A.R. (2011): Polymorphism, structural characterization and electrical properties of $Na_2Nb_4O_{11}$. Journal of Material Chemistry, 21,12096-12102.

Megaw, H.D. (1968 a): A simple theory of the off center displacement of cation in octahedral environment. Acta Crystallographica, B24, 149-153.

Megaw, H.D. (1968 b): The thermal expansion of interatomic bonds, illustrated by experimental evidence from niobates. Acta Crystallographica, A24, 589-604.

Nikandrov, S.N. (1990): Franconite, first find in the USSR. Doklady Acad. Nauk SSSR, 305, 700-703.

Nyman, M., Tripathi, A., Parise, J.B., Maxwell, R.S., Harrison, W.T.A. and Nenoff, T.M. (2001): A new family of octahedral molecular sieves: Sodium Ti/Zr^{IV} niobates. Jounral of the American Chemical Society, 123, 1529-1530.

Nyman, M., Tripathi, A., Parise, J.B., Maxwell, R.S. and Nenoff, T.M. (2002): Sandia octahedral molecular sieves (SOMS): Structural and property effects of charge-balancing the M^{IV}-substituted (M = Ti, Zr) niobate framework. Journal of the American Chemical Society, 124, 1704-1713.

Pekov, I.V. and Podlesnyi, A.S. (2004): Kukisvumchorr deposit: Mineralogy of alkaline pegmatites and hydrothermalites. Mineralogical Almanac, 7, 60-65.

Rastsvetaeva, R.K., Tamazyan, R.A., Pushcharovsky, D.Y. and Nadezhina, T.N. (1994): Crystal structure and microtwinning of K-rich nenadkevichite. European Journal of Mineralogy, 6, 503-509.

Salles, F., Douillard, J., Denoyel, R., Bildstein, O., Jullien, M., Beurroies, I. and Damme, H. (2009): Hydration sequence of swelling clays: Evolutions of specific surface area and hydration energy. Journal of Colloid and Interface Science, 333, 510-522.

Schilling, J., Marks, M.A.W., Wenzel, T., Vennemann, T., Horváth, L., Tarassoff, P., Jacob, D.E. and Markl, G. (2011): Magmatic to hydrothermal evolution of the intrusive Mont Saint-Hilaire complex: insights into the late-stage evolution of peralkaline rocks. Journal of Petrology 52, 2147-2185.

Shannon, R.D. (1976): Revised effective ionic radii and systematic studies in interatomic distances in halides and chalogenides. Acta Crystallographica, A32, 751-767.

Sheldrick, G.M. (1997): SHELXL-97: A computer program for the Refinement of Crystal Structures. Univ. of Göttingen, Göttingen, Germany.

Sokolova, E. and Hawthorne, F.C. (2004): The crystal chemistry of epistolite. Canadian Mineralogist, 42, 797-806.

Sokolova, E. and Hawthorne, F.C. (2008): From structure topology to chemical composition. V. Titanium silicates: The crystal chemistry of nacareniobsite-(Ce). Canadian Mineralogist, 46, 1333-1342.

Subbotin, V.V., Voloshin, A.V., Pakhomovskii, Y.A., Men'shikov, Y.P. and Subbotina, G.F. (1997): Ternovite, $(Mg,Ca)Nb_4O_{11}•nH_2O$, a new mineral and other hydrous tetraniobates from carbonatites of the Vuoriyarvi massif, Kola Peninsula, Russia. Neues Jahrbuch für Mineralogie, 2, 49-60.

Uvarova, Y.A., Sokolova, E., Hawthorne, F.C., Pautov, L.A. and Agakhanov, A.A. (2004): A novel $[Si_{18}O_{45}]^{18-}$ sheet in the crystal structure of zeravshanite, $Cs_4Na_2Zr_3[Si_{18}O_{45}](H_2O)_2$. Canadian Mineralogist, 42, 125-134.

Williams, Q. (1995): Infrared, Raman and optical spectroscopy of Earth materials. American Geophysical Union, 291- 302.

Xu, H., Nyman, M., Nenoff, T.M. and Navrotsky, A. (2004): Prototype sandia octahedral molecular sieve (SOMS) $Na_2Nb_2O_6 \bullet H_2O$: Synthesis, structure and thermodynamic stability. Chemistry of Materials, 16, 2034-2040.

Yim, H., Yoo, S., Nahm, S., Hwang, S., Yoon, S. and Choi, J. (2013): Synthesis and dielectric properties of layered $HCa_2Nb_3O_{10}$ structure ceramics. Ceramics International, 39, 611-614.

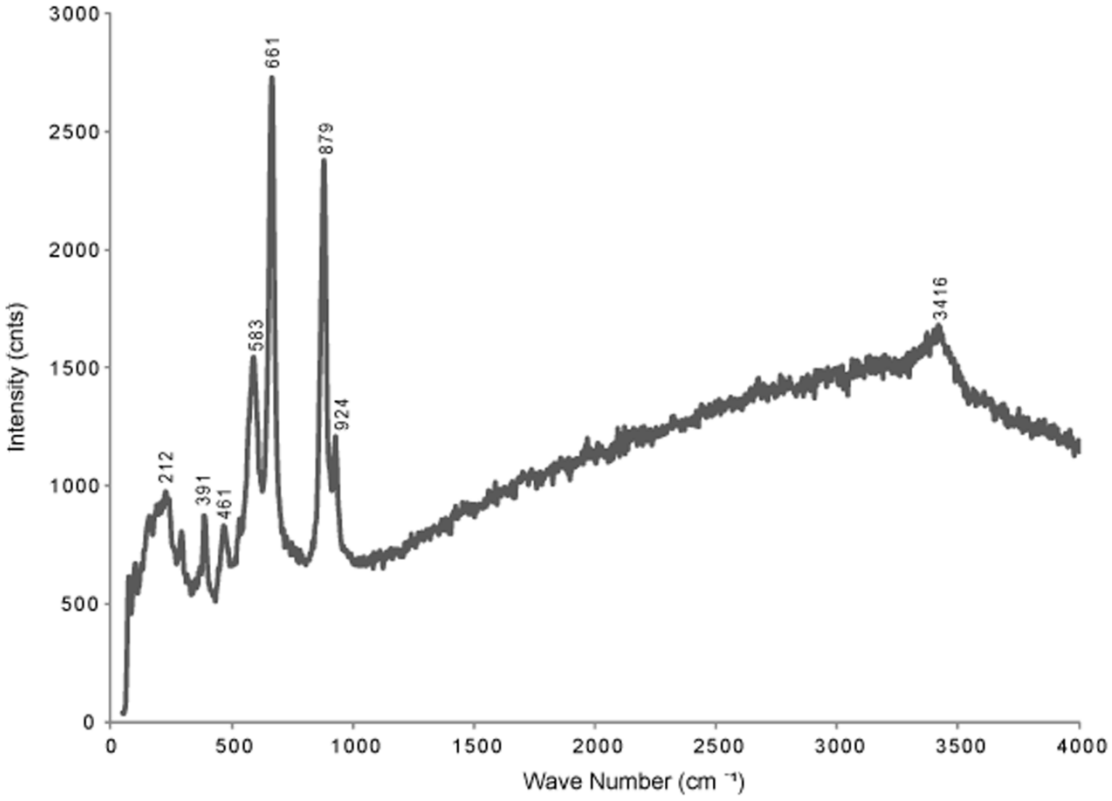

Figure 4-1. Raman spectrum for franconite.

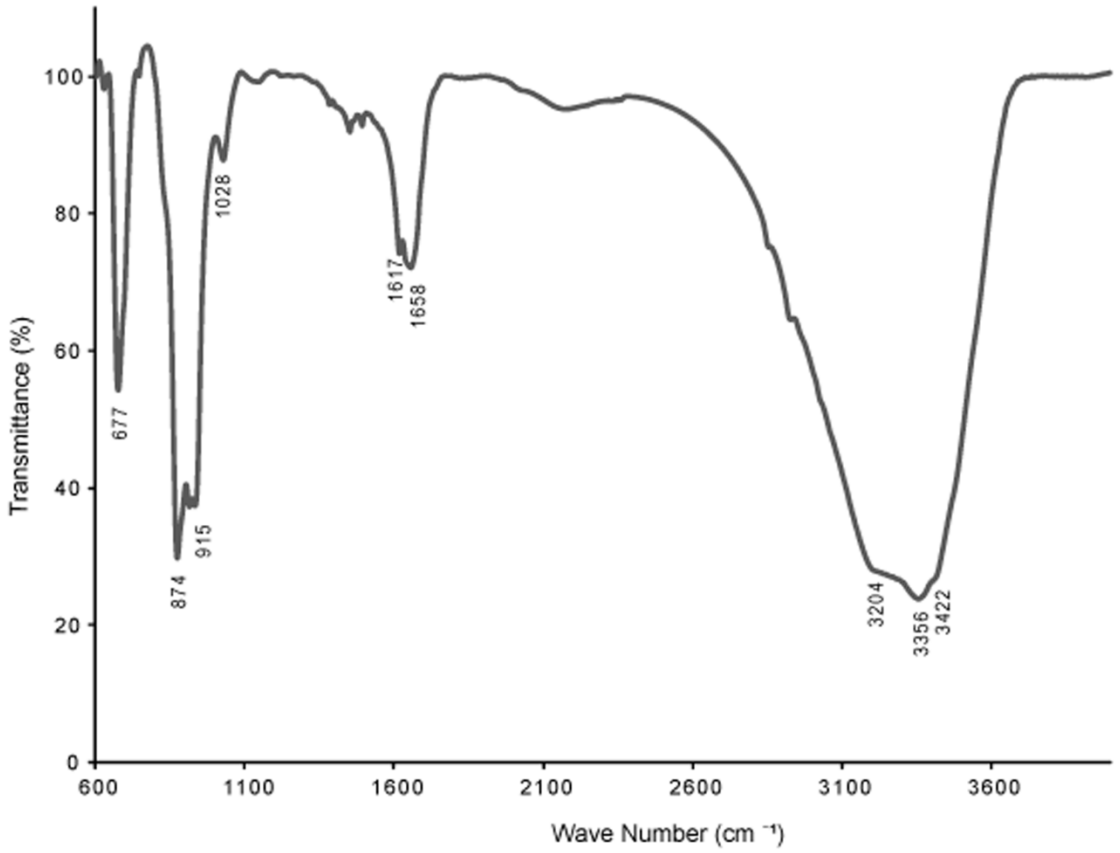

Figure 4-2. FTIR spectrum for franconite with transmittance peaks indicated.

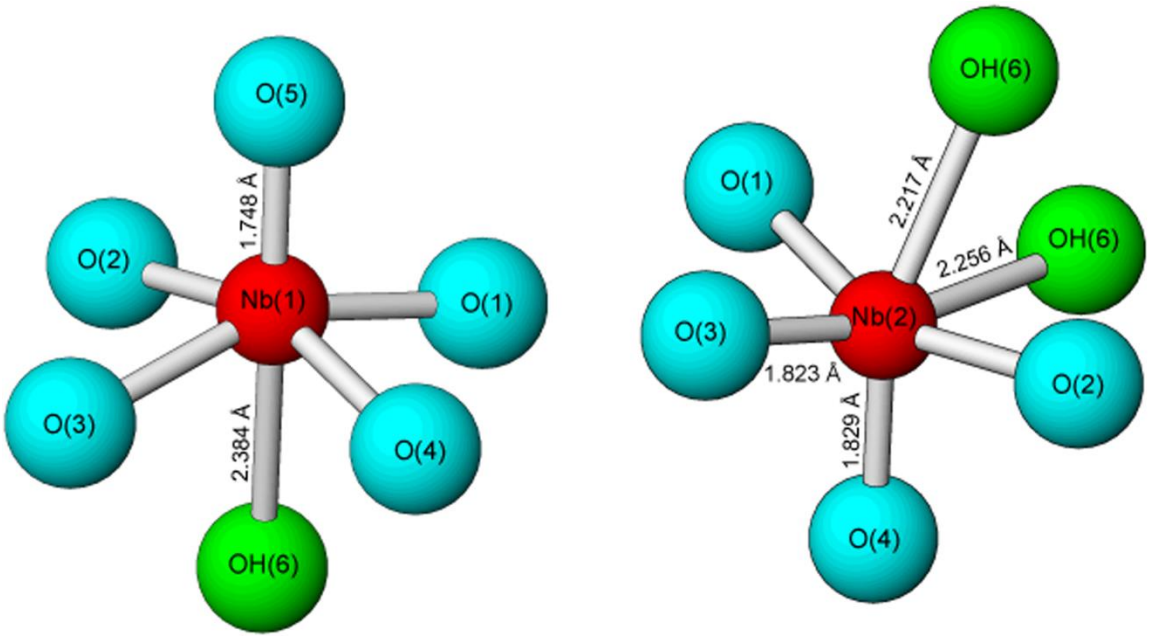

Figure 4-3. The two distorted octahedral Nb sites in franconite.

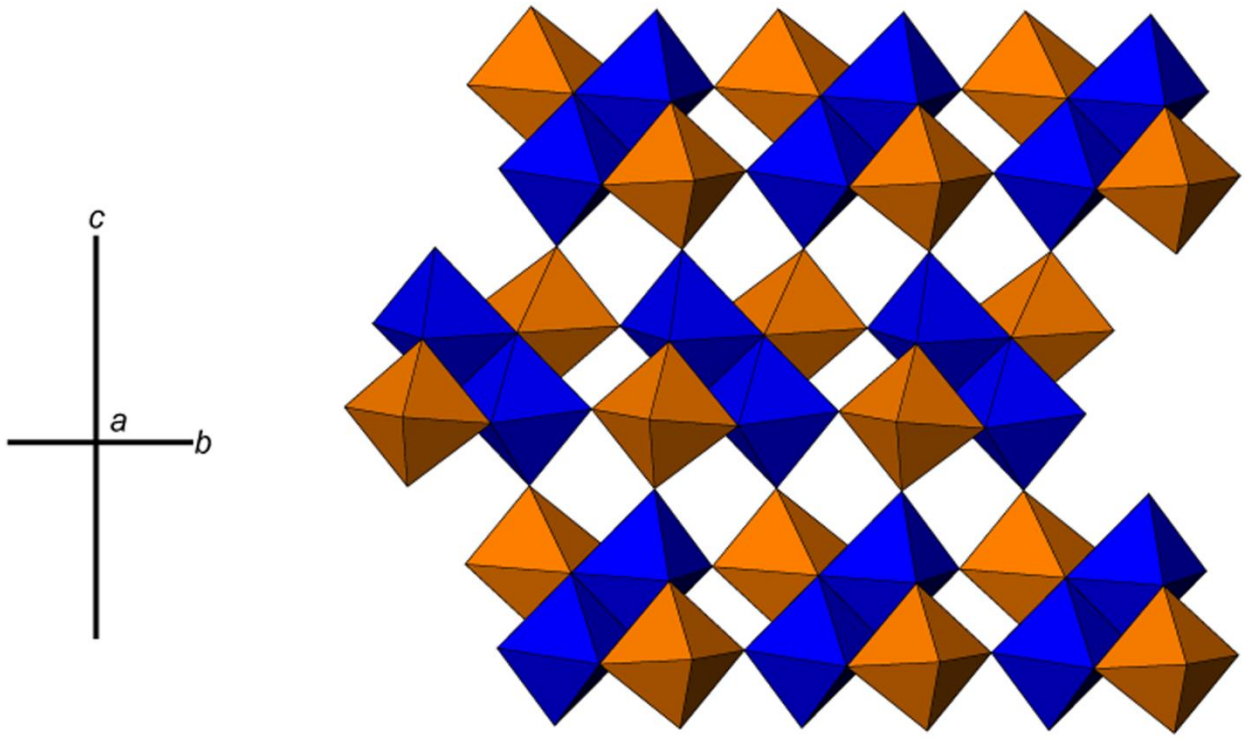

Figure 4-4. Octahedral layer in franconite consisting of $Nb(1)O_5(OH)$ octahedra (dark blue) and $Nb(2)O_4(OH)_2$ octahedra (orange).

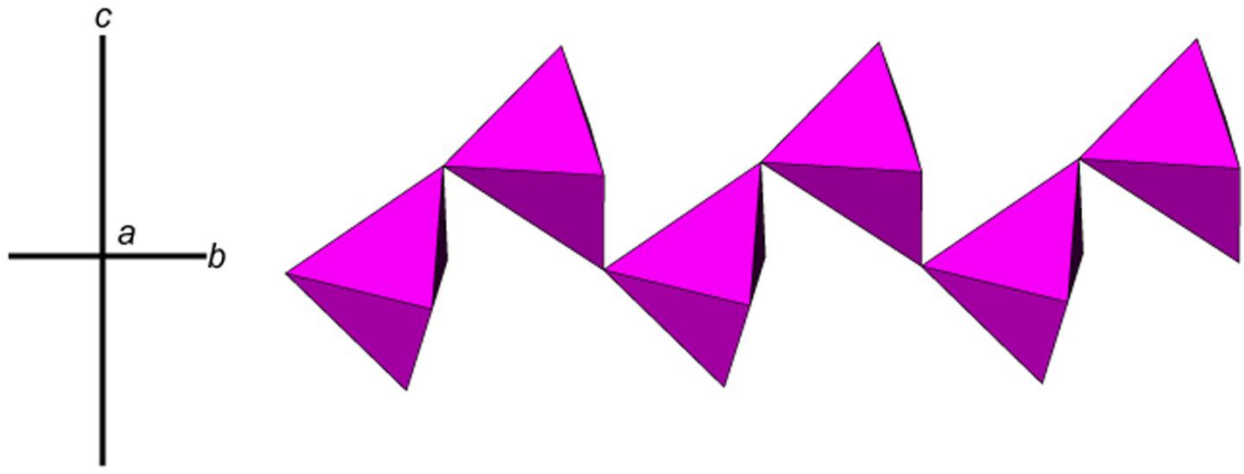

Figure 4-5. Chains of edge-sharing $NaO(H_2O)_4$ polyhedra parallel to [100]

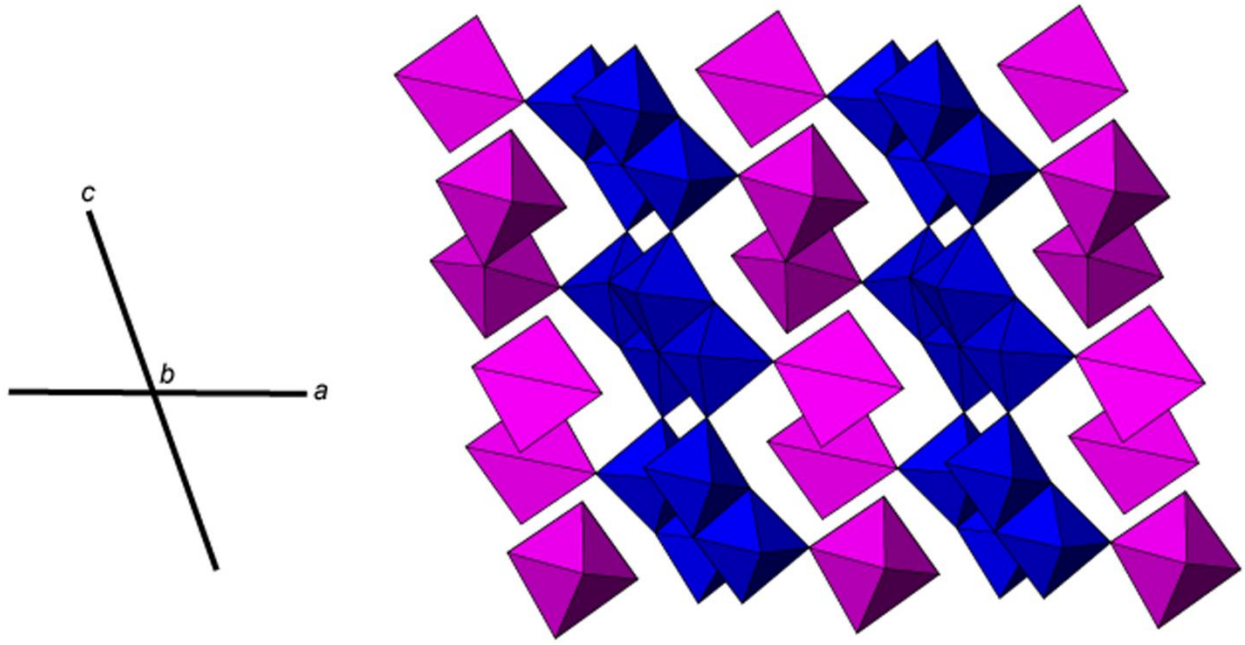

Figure 4-6. The crystal structure of franconite projected onto [010] showing layers of NbO_6 octahedra (dark blue) alternating with layers containing $NaO(H_2O)_4$ polyhedra (pink).

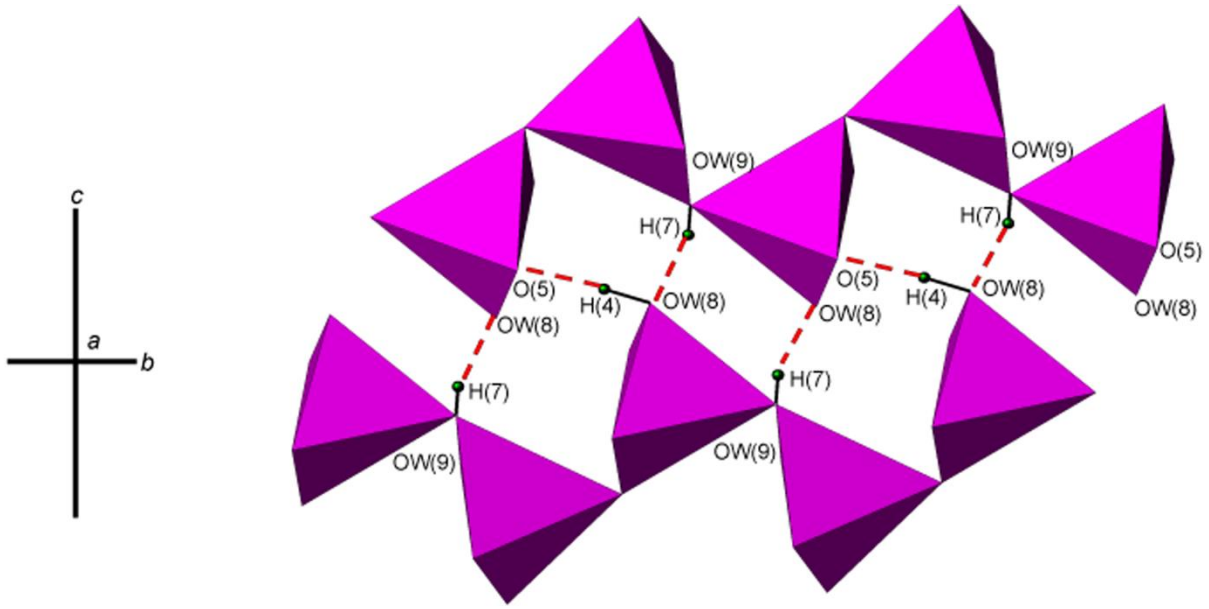

Figure 4-7. The local environment of group 1 hydrogen bonds. These hydrogen bonds only occur within the $Na(O,H_2O)_5$ polyhedral layer and link together adjacent chains of $NaO(H_2O)_4$ polyhedra.

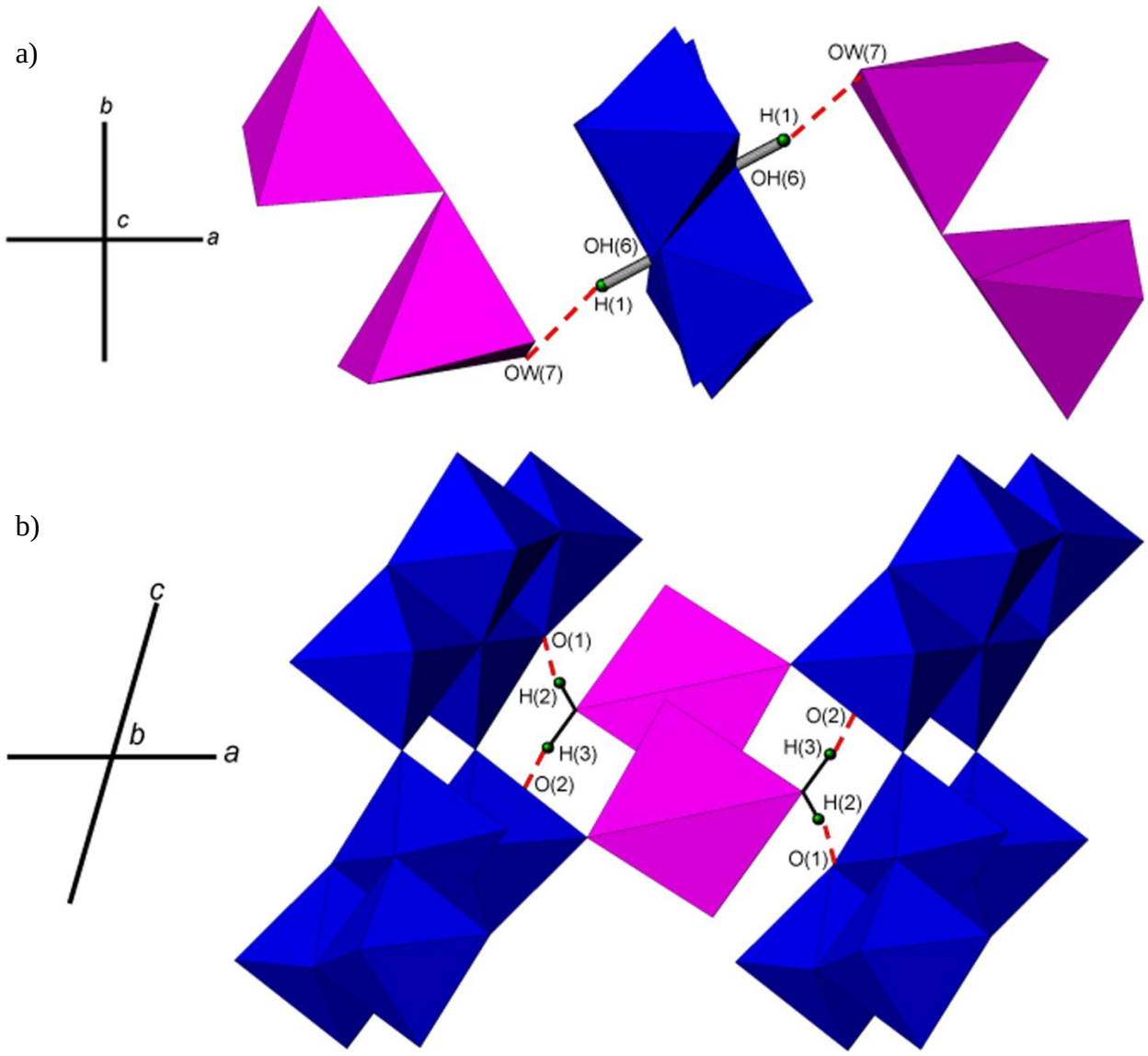

Figure 4-8. The local environment of group 2 interlayer hydrogen bonds. These hydrogen bonds link together the $Na(O,H_2O)_5$ polyhedral layer and $Nb(O,OH)_6$ octahedral layers. Group 1 hydrogen bonds occur in three sets including a) Set1 involving H(1) atoms b) Set 2 involving H(2) and H(3) atoms, and c) Set 3 atoms involving H(5) and H(6) atoms.

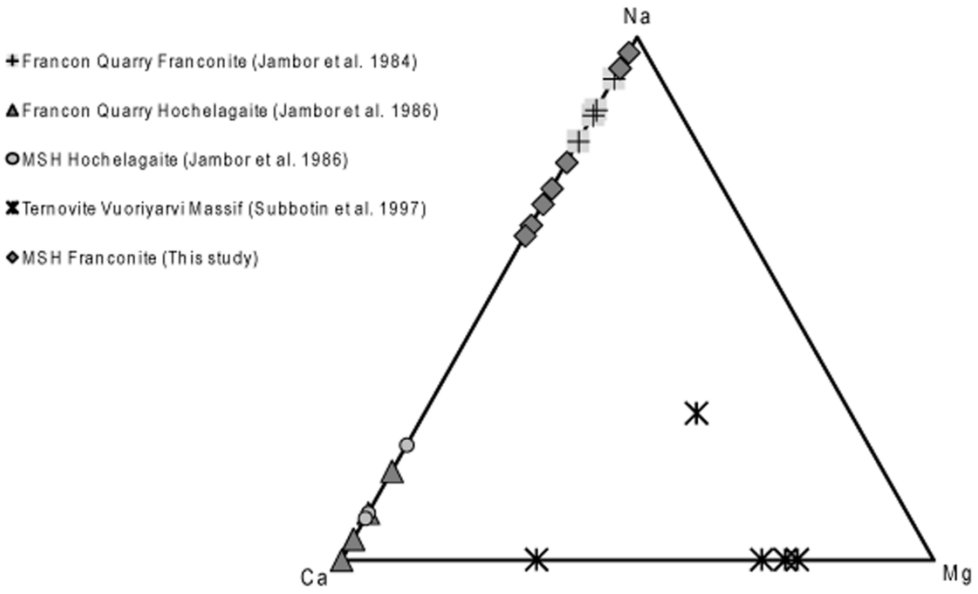

Figure 4-9. Na-Ca-Mg ternary system for franconite, hochelagaite and ternovite.

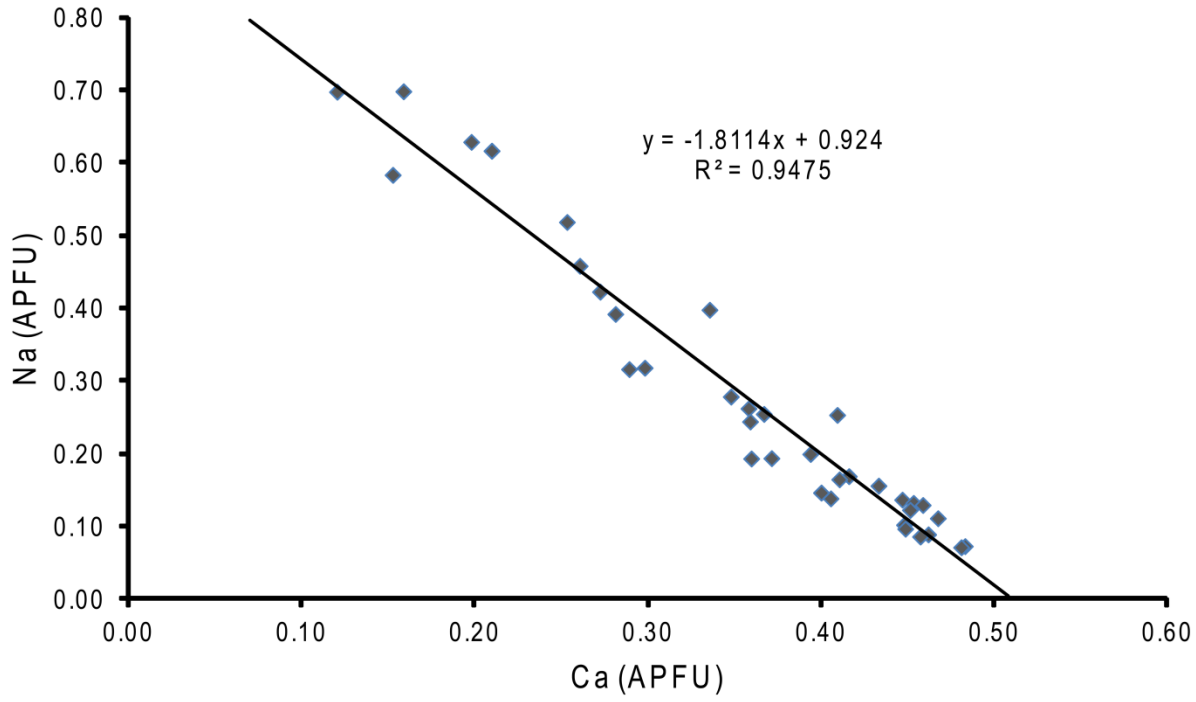

Figure 4-10. Na vs. Ca content in the crystal structure of franconite. Values of Na and Ca are expressed as atoms per formula unit (APFU).

Table 4-1. Modal abundances and descriptions of minerals associated with franconite.

Mineral	Modal Abundance (%)	Description
Microcline ($KAlSi_3O_8$)	~ 45	Light grey subhedral crystals ranging from ~ 2 to 5 mm in diameter.
Analcime $Na_2(Al_2Si_4O_{12})•2H_2O$	~ 25	Translucent, anhedral to subhedral crystals ranging from 2 to 3 mm in diameter.
Sodalite $Na_8(Al_6Si_6O_{24})Cl_2$	~ 15	Light blue anhedral crystals ranging from 1-3 mm in diameter.
Siderite $FeCO_3$	~ 10	Light brown to tan euhedral crystals exhibiting the form rhombohedron $\{10\bar{1}1\}$and ranging from 3 to 5 mm in diameter
Pyrite FeS_2	~ 5	Anhedral crystals ranging from 1-3 mm in diameter

Table 4-2. Observed absorption bands and band assignments for the Raman Spectrum of franconite.

Raman Absorption Band (cm-1)	Suggested Assignment
3416	O-H Stretching
924	symmetric stretching of Nb=O double bond
879	symmetric stretching of Nb=O double bond
661	Nb-O-Nb linkages - symmetric stretching
583	Nb-O-Nb linkages - symmetric stretching
461	Na-O/Ca-O
391	Na-O/Ca-O
297	Na-O/Ca-O
212	Na-O/Ca-O

Table 4-3. Observed transmittance bands and band assignments for the FTIR spectrum of franconite.

FTIR Transmittance band (cm^{-1})	Suggested Assignment
3422	O-H Stretching
3356	O-H Stretching
3204	O-H Stretching
1658	H-O-H stretching
1617	H-O-H stretching
1028	Nb=O double bond
915	Nb=O double bond
874	Nb=O double bond
677	Nb-O-Nb linkages - symmetric stretching

Table 4-4.Franconite X-ray powder diffraction data.

I_{meas}	I_{calc}	d_{meas} Å	d_{calc} Å	h	k	l	I_{meas}	I_{calc}	d_{meas} Å	d_{calc} Å	h	k	l
100	100	10.211	9.968	1	0	0	5	1	2.114	2.112	1	0	-6
3	7	6.261	6.246	0	0	-2		2		2.097	1	3	0
23	16	5.479	5.407	1	1	0	5	1	2.044	2.029	0	3	-2
21	6	5.050	4.984	2	0	0	9	3	2.007	2.002	5	0	-2
	16		4.925	1	0	2		1		1.998	3	1	4
6	5	4.265	4.271	2	0	-2		1		1.994	5	0	0
15	11	3.989	3.941	2	1	0	5	5	1.985	1.971	1	0	6
	2		3.914	2	1	-1	4	2	1.918	1.911	5	1	-2
	7		3.911	1	1	2	2	2	1.903	1.904	5	1	0
3	2	3.693	3.619	2	1	1	6	2	1.779	1.776	3	3	-2
	3		3.605	2	0	2	2	1	1.764	1.766	1	2	-6
6	6	3.560	3.556	2	1	-2		1		1.761	3	3	1
21	15	3.213	3.218	0	2	0	2	1	1.730	1.736	2	3	3
32	14	3.157	3.145	2	1	2		2		1.736	4	1	4
	12		3.138	1	0	-4	5	1	1.708	1.713	1	3	4
	13		3.123	0	0	-4		2		1.7	5	2	-2
9	6	3.097	3.116	0	2	-1		1		1.695	5	2	0
16	19	2.843	2.843	3	1	-2	3	3	1.683	1.692	4	1	-6
3	1	2.725	2.704	2	2	0		2		1.69	3	3	2
3	2	2.629	2.628	2	1	-4		2		1.681	1	2	6
6	1	2.578	2.57	2	2	-2	5	1	1.597	1.596	0	4	-1
2	4	2.520	2.524	3	1	2	2	1	1.567	1.569	2	0	-8
4	6	2.303	2.302	4	1	-2	1	1	1.527	1.525	2	1	-8
6	2	2.262	2.247	1	2	-4							
	2		2.241	0	2	-4							

Table 4-5. Miscellaneous data for franconite.

a (Å)	10.119(2)	Monochromator	Graphite
b	6.436(1)	Intensity-data collection	θ:2θ
c	12.682(2)	Criterion for observed reflections	$F_o>4\sigma(F_o)$
β (°)	99.91(3)	GooF	1.022
V(Å^3)	813.6	total No. of reflections	28653
Space Group	$P2_1/c$ (#14)	No. Unique reflections	2380
Z	4	*R* (merge %)	5.93
Radiation	Mo*K*α (50 kV, 40 mA)	*R* %	4.63
		wR^2 %	11.95

Table 4-6. Atomic Positions and displacement parameters ($Å^2$) for franconite.

ATOM	*x*	*y*	*z*	U_{11}	U_{22}	U_{33}	U_{23}	U_{13}	U_{12}	U_{eq}
Na(1)	0.5288(3)	0.2454(5)	0.3395(3)	0.032(2)	0.030(2)	0.030(2)	0.001(1)	0.008(1)	0.002(1)	0.0304(6)
Nb(1)	0.16333(5)	0.2742(8)	0.40382(4)	0.0198(3)	0.0071(2)	0.0099(2)	0.0003(2)	0.0043(2)	0.0001(2)	0.0120(1)
Nb(2)	-0.00108(5)	0.18674(7)	0.60733(4)	0.0228(3)	0.0057(2)	0.0076(2)	-0.0006(2)	0.0045(2)	0.0001(2)	0.0119(1)
O(1)	0.1710(4)	0.2516(6)	0.5586(3)	0.021(2)	0.011(2)	0.012(2)	0.001(1)	0.003(2)	0.000(2)	0.0147(8)
O(2)	-0.1673(4)	0.0287(7)	0.6170(3)	0.025(2)	0.011(2)	0.014(2)	0.000(1)	0.007(2)	0.001(2)	0.0160(8)
O(3)	0.0729(5)	0.1963(7)	0.7489(3)	0.035(3)	0.014(2)	0.009(2)	0.000(1)	0.004(2)	-0.001(2)	0.0191(9)
O(4)	-0.0845(5)	0.4391(6)	0.5862(3)	0.032(2)	0.006(2)	0.016(2)	0.000(1)	0.007(2)	0.003(2)	0.0179(9)
O(5)	0.3290(5)	0.3395(8)	0.3959(4)	0.024(2)	0.022(2)	0.022(2)	-0.003(2)	0.010(2)	-0.001(2)	0.0223(9)
OH(6)	0.0483(4)	-0.1383(6)	0.5714(3)	0.021(2)	0.008(2)	0.011(2)	-0.003(1)	0.002(1)	0.001(1)	0.0134(8)
OW(7)	0.7421(6)	0.3854(8)	0.3178(4)	0.035(3)	0.026(3)	0.024(2)	0.001(2)	0.009(2)	-0.008(2)	0.028(1)
OW(8)	0.6084(6)	0.2536(9)	0.5286(5)	0.031(3)	0.030(3)	0.031(3)	-0.001(2)	0.001(2)	0.002(2)	0.031(1)
OW(9)	0.4335(6)	0.378(1)	0.1641(5)	0.035(3)	0.037(3)	0.037(3)	0.003(3)	0.002(2)	-0.006(2)	0.037(1)
H(1)	0.124(5)	-0.20(1)	0.619(5)							0.01(2)
H(2)	0.78(1)	0.50(1)	0.364(8)							0.07(4)
H(3)	0.78(1)	0.41(2)	0.254(5)							0.07(4)
H(4)	0.60(1)	0.395(7)	0.553(9)							0.06(3)
H(5)	0.68(1)	0.17(2)	0.57(1)							0.11(6)
H(6)	0.347(4)	0.32(1)	0.133(6)							0.02(2)
H(7)	0.511(8)	0.37(2)	0.128(9)							0.08(4)

Table 4-7. Bond-valence table (*v.u.*) for franconite.

	Na	Nb(1)	Nb(2)	∑	H(1)	H(2)	H(3)	H(4)	H(5)	H(6)	H(7)	∑
O(1)		$0.806^{\downarrow\rightarrow}$	$0.893^{\downarrow\rightarrow}$	1.699		$0.15^{\downarrow\rightarrow}$				$0.15^{\downarrow\rightarrow}$		1.999
O(2)		$0.812^{\downarrow\rightarrow}$	$0.857^{\downarrow\rightarrow}$	1.669			$0.15^{\downarrow\rightarrow}$		$0.17^{\downarrow\rightarrow}$			1.989
O(3)		$1.269^{\downarrow\rightarrow}$	$0.727^{\downarrow\rightarrow}$	1.996								1.996
O(4)		$1.251^{\downarrow\rightarrow}$	$0.739^{\downarrow\rightarrow}$	1.990								1.990
O(5)	$0.233^{\downarrow\rightarrow}$		$1.558^{\downarrow\rightarrow}$	1.791				$0.15^{\downarrow\rightarrow}$				1.941
OH(6)		$0.832^{\downarrow\rightarrow}$	$0.279^{\downarrow\rightarrow}$	1.111	$0.84^{\downarrow\rightarrow}$							1.951
OW(7)	$0.198^{\downarrow\rightarrow}$			0.198	$0.16^{\downarrow\rightarrow}$	$0.85^{\downarrow\rightarrow}$	$0.85^{\downarrow\rightarrow}$					2.058
OW(8)	$0.198^{\downarrow\rightarrow}$			0.198				$0.85^{\downarrow\rightarrow}$	$0.83^{\downarrow\rightarrow}$		$0.15^{\downarrow\rightarrow}$	2.028
OW(9)	$0.380^{\downarrow\rightarrow}$			0.380						$0.85^{\downarrow\rightarrow}$	$0.85^{\downarrow\rightarrow}$	2.080
∑	1.009	4.970	5.053		1.00	1.00	1.00	1.00	1.00	1.00	1.00	

* Bond valences for H sites determined using parameters from Brown and Altermatt (1985). Bond valences for other sites determined using parameters from Brese and O'Keeffe (1991).

Table 4-8. Interatomic distances (Å) in franconite.

*Na*O$(H_2O)_4$ Polyhedron			*Nb*(2)$O_4(OH)_2$ Octahedron		
Na	-O5	2.337(6)	*Nb*2	-O3	1.823(4)
	-OW8	2.396(7)		-O4	1.829(4)
	-OW7	2.398(6)		-O2	1.988(4)
	-OW9	2.399(7)		-O1	1.990(4)
	-OW9	2.422(7)		-OH6	2.217(4)
<*Na*	-O>	2.390		-OH6	2.256(4)
			<*Nb*2	-O>	2.017

Nb(1)O_5(OH) Octahedron		
*Nb*1	-O5	1.748(5)
	-O1	1.956(4)
	-O2	1.969(4)
	-O4	2.023(4)
	-O3	2.029(4)
	-OH6	2.384(4)
<*Nb*1	-O>	2.018

Hydrogen Bonding

Donor-H	*d*(D-H; Å)	*d*(H..A; Å)	<DHA (°)	*d*(D..A; Å)	Acceptor
OH6-H1	0.980	1.868	164.48	2.824	OW7
OW7-H2	0.980	1.901	167.63	2.866	O1
OW7-H3	0.980	1.934	170.30	2.905	O2
OW8-H4	0.980	1.938	149.20	2.823	O5
OW8-H5	0.980	1.816	159.84	2.762	O2
OW9-H6	0.980	1.918	168.04	2.884	O1
OW9-H7	0.980	1.909	151.41	2.800	OW8

Chapter 5

Charleshatchettite, $CaNb_4O_{10}(OH)_2 \cdot 8H_2O$, a new mineral from Mont Saint-Hilaire, Québec, Canada: Description, Crystal-Structure Determination and Origin

5.1 Abstract

Charleshatchettite, $CaNb_4O_{10}(OH)_2 \cdot 8H_2O$, is a new mineral related to franconite and hochelagaite, discovered on a fracture surface of a nepheline syenite at Mont Saint-Hilaire, Québec, Canada. The mineral occurs in white globules (~ 0.15 to 0.20 mm in diameter) composed of radiating crystals with individual crystals having average dimensions of ~ 0.002 x 0.010 x 0.040 mm. Crystals are euhedral, bladed (flattened on [100]) and are transparent to translucent. The mineral is associated with albite, quartz, muscovite, pyrrhotite, pyrite, ancylite-(Ce), and siderite. Charleshatchettite is inferred to be biaxial (-) with α' = ~1.72(2) and γ' = ~1.82(2). Data from chemical analyses (SEM-EDS, n = 8): CaO 7.96 (7.04 – 8.63), MgO 0.24 (0.08 – 0.78), Al_2O_3 0.13 (*b.d.* – 0.49), SiO_2 1.04 (0.49 – 1.88), TiO_2 3.64 (2.45-5.05), Nb_2O_5 68.07 (64.83 – 71.01), and H_2O (calc.) 22.96, total 104.04 wt. % gives the average empirical formula: $(Ca_{1.00}Mg_{0.04})_{\Sigma=1.04}(Nb_{3.62}Ti_{0.32}Si_{0.12}Al_{0.02})_{\Sigma=4.08}O_{10}(OH)_2 \bullet 8H_2O$ (based on 20 anions). This is similar to that of hochelagaite ($CaNb_4O_{11} \bullet nH_2O$), although the two are readily distinguished by their powder X-ray diffraction patterns. Results from single-crystal X-ray diffraction analysis give a = 21.151(4) b = 6.496(2) c = 12.714(3) Å and β = 103.958(3) °, space group $C2/c$ (#15). The crystal structure, refined to R = 5.64 %, contains one *Ca* site, two distorted octahedral *Nb* sites, and ten *O* sites. It consists of clusters of four edge-sharing $Nb(O,OH)_6$ octahedra, linked through shared corners to adjacent clusters, forming layers of $Nb(O,OH)_6$ octahedra. These alternate along [100] with layers composed of $Ca(H_2O)_8$

polyhedra, the two being linked together by H-bonding. Charleshatchettite is a late-stage mineral, interpreted to have developed through the interaction of low *T* (< 150 °C) aqueous fluids with an alkali-, Nb-rich precursor under slightly reducing conditions and a highly alkaline pH. The precursor mineral(s) is unknown but is considered to have been Nb-dominant, relatively unstable under slightly reducing as well as alkaline conditions, and likely itself would have been a product of near-complete Nb/Ta fractionation due to the paucity of Ta in charleshatchettite. Charleshatchettite is crystallochemically related to SOMS [Sandia Octahedral Molecular Sieves; $Na_2Nb_{2-x}M_xO_{6-x}(OH)_x \bullet H_2O$ with *M* = Ti, Zr, Hf], a group of synthetic compounds with strong ion exchange capabilities.

5.2 Introduction

Franconite-group minerals (FGM) are alkali-niobate hydrates that develop as late-stage, low-*T* minerals in agpaitic environments including Mont-Saint Hilaire (Horváth & Gault 1990), the Saint-Amable sill (Horváth *et al*. 1998), the Khibiny massif (Pekov & Podlesnyi 2004), the Vuoriyarvi alkaline-ultrabasic massif (Belovitskaya & Pekov 2004) and the Vishnevogorsk alkali complex (Nikandrov, 1990). Current members of the FGM include franconite [$Na(Nb_2O_5)(OH) \bullet 3H_2O$], hochelagaite ($CaNb_4O_{11} \bullet nH_2O$; Jambor *et al*. 1986), and ternovite [$MgNb_4O_{11} \bullet nH_2O$; Subbotin *et al*. 1997]. The crystal structures and chemical formulas of these minerals are in general, difficult to resolve, primarily owing to their occurrence in thin (<5 μm) blades, but also because these typically develop into more complex, radiating spheres wherein more than one species may be present. Despite obvious challenges, progress has been made in unravelling the crystal-chemical structures of the FGM, mainly due to advances having been made in single-crystal X-ray diffraction methods. For example, the crystal structure of

franconite was solved by Haring & McDonald (2014) who showed the mineral is strongly layered with sheets of $Nb(O,OH)_6$ polyhedra alternating with sheets $Na(O,H_2O)_5$ polyhedra, these being joined by weak H-bonds along [100], and provided a refined chemical formula $Na(Nb_2O_5)(OH)\bullet 3H_2O$. The crystal structures of hochelagaite and ternovite still remain unsolved but a combination of data from PXRD and Raman/FTIR spectroscopy suggest they are all closely related.

As part of a broader study aimed at better understanding the development of late-stage niobate minerals from agpaitic environments, an investigation of a previously undescribed species believed to be related to minerals of the FGM, was undertaken. This mineral, which serves as the subject of this report, was likely first observed in specimens (n = 5) collected by Elsy and Les Horvath in 1978. It was not recognized as a potentially new species until 1985, based on material (n = 2) collected in the Poudrette Quarry at Mont Saint-Hilaire, QC by the late Mr. Ron Wadell. The material was found to be a Ca-niobate hydrate, chemically similar to hochelagaite, but with a PXRD pattern distinct from that of the former; it was thus considered as potentially being a new mineral species and given the temporary designation UK56. The very thin nature of its crystals (~0.002 mm on average) and evidence for stacking disorder (*e.g.*, X-ray precession images) precluded a complete analysis by single-crystal methods available and so it remained an unidentified mineral for a considerable period of time. However, the advent of extremely bright X-ray sources arising from a combination of rotating-anode generators coupled with multi-layer optics, incident-beam paths, and highly sensitive detectors, has proved invaluable in solving the crystal structures of minerals whose crystal structures would have formerly been challenging if not impossible to solve (Cooper & Hawthorne 2012). An example of just how critical this

technology has become is shown in this study of UK56, which is now recognized as the new species, charleshatchettite, $CaNb_4O_{10}(OH)_2 \bullet 8H_2O$.

In this contribution we present and discuss data pertaining to the crystal chemistry of charleshatchettite, elucidate the relationship of the mineral to other members of the FMG, describe the geological conditions under which it is thought to have developed and compare it to synthetic niobate compounds such as Sandia Octahedral Molecular Sieves (SOMS). The mineral is named in recognition of Charles Hatchett (b.1765 – d.1847), an English chemist who discovered niobium, a dominant element in charleshatchettite. Both the mineral and mineral name have been approved by the Commission on New Minerals, Nomenclature and Classification of the International Mineralogical (2015 – 048). The holotype material is housed in the collections of the Canadian Museum of Nature, Gatineau, Québec, under catalogue number CMNMC 86894.

5.3 Occurrence

Charleshatchettite was discovered on a fracture surface on a fine-grained nepheline syenite at the Poudrette quarry, La Vallée-du-Richelieu, Montérégie (formerly Rouville County), Québec, Canada (45°33′8″N, 73°9′3″W). Associated minerals include (in order of decreasing modal abundance) albite, quartz, muscovite, pyrrhotite, pyrite, ancylite-(Ce), and siderite. The mineral has only been found on two samples to date. Owing to the similarity in appearance and physical properties of charleshatchettite to other FGM, the mineral may be present other specimens labelled as hochelagaite or franconite. The fracture surface upon which charleshatchettite occurs is dominated by translucent, white, subhedral, blocky crystals of albite (average dimensions: 0.7 x 1.5 x 2 mm). These are intergrown with transparent crystals of euhedral

quartz displaying the forms prism {120} and dipyramid {112} (average dimensions: 0.9 x 0.8 x 1.5 mm). Both the quartz and the albite are overgrown by euhedral, colourless, platy crystals of muscovite, which can also be found intergrown with anhedral crystals of pyrrhotite. The pyrrhotite is strongly magnetic, suggesting that it is likely the monoclinic 4*C* polytype, possibly suggesting a T of formation < 230° C (Kontny et al. 2000). The pyrrhotite is overgrown by euhedral crystals of pyrite displaying the cube {100} and octahedron {111}. Siderite overgrows both the pyrrhotite and the pyrite and can show rusty staining. It develops as euhedral rhombohedra {111} that are tan to light brown (average dimensions 1.0 x 0.8 x 1.2 mm). Rare, euhedral, light pink crystals ancylite-(Ce) (average dimensions: 0.4 x 0.5 x 0.8 mm) overgrow muscovite and pyrrhotite. The associated ancylite-(Ce) is characterized by a bluish-grey fluorescence when exposed to long-, medium, and short-wave radiation. Charleshatchettite is paragentically the last mineral to develop and can be found overgrowing all the other associated minerals. The general paragenetic sequence involving charleshatchettite is given in Fig. 5-1.

5.4 Physical Properties

Charleshatchettite occurs in white globules ~ 0.15 to 0.20 mm in diameter, composed of radiating crystals (Fig. 5-2). Individual crystals have average dimensions of ~ 0.07 x 0.02 x 0.01 mm and are euhedral, bladed with a perfect [100] cleavage. They are white, transparent to translucent, with a silky lustre, and are flattened on [100] and elongated along [001]. Charleshatchettite, like hochelagaite, does not exhibit fluorescence under long-, medium-, or short-wave radiation; this is in contrast with franconite that typically exhibits a distinctive bright yellow-white fluorescence under short-wave and a dull yellow-white fluorescence under long-wave radiation (Horvath & Gault 1990). The Moh's hardness could not be determined due to the small sizes of the crystals. Hochelagaite was estimated to have a Moh's hardness of ~ 4 and

given the crystal-chemical similarities between hochelagaite and charleshatchettite, charleshatchettite, likely has a similar hardness. A density of 2.878 g/cm^3 was calculated using the empirical chemical formula and unit-cell parameters derived from the crystal-structure analysis.

A complete set of optical data as well as an interference figure could not be measured due to the thinness (~ 1 μm) of the crystals the *b*-axis. The mineral is assumed to be biaxial due to the fact it is monoclinic. It has α' = ~1.72(2) perpendicular to the plane of the blades and γ' = ~1.82(2) along the length of the crystals. These values are similar to those of other FGM including hochelagaite [n_{min} =1.72(2) and n_{max} = 1.82(2), Jambor et al. 1986], franconite [n_{min} = 1.72(2) and n_{max} = 1.79(2), Jambor et al. 1984], and ternovite [n_{min} = 1.72(2) and n_{max} = 1.85(2), Subbotin 1997]. The mineral is assumed to be optically negative as it has unit cell parameters and refractive indices similar to other FGM which are optically negative. Charleshatchettite is colourless under plane-polarized light with no observed pleochroism. The compatibility index, calculated using the empirical formula and unit-cell parameters derived from the crystal-structure analysis, is 0.055 which is considered good (Mandarino 1981). A combination of the instability of the mineral under the electron beam (leading to elemental loss) and that only two refractive indices could be measured likely influence the less-than-ideal compatibility index.

5.5 Chemistry

Chemical analyses of charleshatchettite were made by energy-dispersive spectrometry with a JEOL JSM 6400 scanning electron microscope operated at a voltage of 20 kV, a beam current of ~1 nA, and a beam width of 1 μm. The following standards (X-ray lines) were employed: $CaTiO_3$ (Ca*K*α, Ti*K*α), diopside (Mg*K*α, Si*K*α), albite (Al*K*α), and synthetic $MnNb_2O_6$ (Nb*K*α). Four charleshatchettite-bearing globules were examined in this study and all were found to be a

single-phase, *i.e.*, free of other potential Na-dominant phases, including franconite. From the globules, five crystals of charleshatchettite were selected for analysis. Chemical analyses (n = 8) of these gave the average (range) compositions: CaO 7.96 (7.04 – 8.63), MgO 0.24 (0.08 – 0.78), Al_2O_3 0.13 (*b.d.* – 0.49), SiO_2 1.04 (0.49 – 1.88), TiO_2 3.64 (2.45-5.05), Nb_2O_5 68.07 (64.83 – 71.01), and H_2O (calc.) 22.96, total 104.04 wt. % corresponding to the empirical formula: $(Ca_{1.00}Mg_{0.04})_{\Sigma=1.04}(Nb_{3.62}Ti_{0.32}Si_{0.12}Al_{0.02})_{\Sigma=4.08}O_{10}(OH)_2 \bullet 8H_2O$ (based on 20 anions) or ideally $CaNb_4O_{10}(OH)_2 \bullet 8H_2O$. There was insufficient material for direct analysis of H_2O, so the calculated H_2O is based on results from the crystal structure. The mineral was found to be highly unstable under the electron beam, so the high analytical total may be attributed to water-loss during analysis. Additional elements, including Na, Ta and F, were also sought, but not detected. The strongest EDS peak associated with Ta is located at *L*α 8.145 KeV was absent in the EDS spectrum of charleshatchettite confirming the absence of Ta. Although there is some overlap between peaks in the EDS spectra of Si and Ta, there is a large difference in energy between the strongest peaks of each element (strongest peaks: Ta = *L*α 8.145 KeV, Si = *K*α 1.739 KeV). The notable absence of Ta, despite the crystal-chemical similarity of Ta and Nb, is consistent with analyses made of other Nb-dominant mineral from agpaitic environments, including those of the FGM (Haring & McDonald 2014).

5.6 Raman and Infrared Spectroscopy

The Raman spectrum of charleshatchettite was collected with a Horiba Jobin Yvon XPLORA Raman spectrometer interfaced with an Olympus BX41 microscope using a crystal mounted on a spindle stage and oriented such that the laser was perpendicular to {100}. The spectrum (Fig. 5-3a) represents an average of three 20 s acquisition cycles, each collected over a range of 50 to 4000 cm^{-1}. The mineral was first analysed using an excitation radiation of λ = 532 nm but this

was found to produce fluorescence peaks in the region of ~2500 cm^{-1}, a region that does not typically contain bands attributable to any chemical groups in most minerals. To evaluate this further, the mineral was instead analysed using an excitation radiation of λ = 638 nm; this eliminated all peaks in the region, suggesting they were indeed products of fluorescence. A grating of 1200 lines/cm and a 40x long working distance objective were also used, producing a beam of diameter ~ 2 μm. Calibration was made using the 521 cm^{-1} line of a silicon wafer. The Raman spectrum of charleshatchettite shows bands in the regions of 2900 – 3600, 1400 – 1500, 1000 - 850, 670 - 475 and 470 - 50 cm^{-1} (Table 1) (Fig. 5-2a). The first region at 2900 – 3600 cm^{-1} contains three moderately sharp to broad, weak to moderate intensity peaks at 3314, 3046, and 2939 cm^{-1} that are attributed to O-H bending (Williams 1995). In the region of 1400 – 1500 cm^{-1}, a weak low-intensity peak occurs at 1459 cm^{-1}, ascribed to H-O-H bending. The region of 1000 to 850 cm^{-1} contains two strong, sharp peaks at 930 - 878 cm^{-1} that can be attributed to the symmetric stretching of Nb=O double bonds (Jehng & Wachs 1990; Haring & McDonald 2014). The region between 670 - 475 cm^{-1} contains two strong sharp bands at 658 and 599 cm^{-1} that are attributed to symmetric stretching of Nb-O-Nb bonds (Jehng & Wachs 1990; Haring & McDonald 2014). Finally, the region at 470 - 50 cm^{-1} contains seven low to moderate intensity peaks at 489, 378, 234, 215, 205, 150, and 115 cm^{-1} attributed to Ca-O bonds (Williams 1995). To confirm these band assignments, a Raman spectrum was calculated using results from the refined crystal structure (described below) along with the programs GAUSSIAN (Frisch *et al*. 2013) to calculate force constants for each bond, and VIBRATZ (Dowty 2009) to determine and refine the calculated Raman spectrum (Table 5-1). Results show an overall good agreement between the experimental and calculated Raman spectra in terms of both band position and intensity (Table 5-1). As a note, those peaks associated with O-H and H-O-H bending could not

be determined for the calculated Raman spectrum owing to the fact that the site(s) occupied by H could not be reliably determined from the refined crystal structure. The Raman spectra for charleshatchettite and hochelagaite are compared in Figure 5-3b. These show that the spectra of the two minerals are virtually indistinguishable from one another; this is predictable, owing to strong chemical and crystal-structure similarities between the two. However, it does indicate that Raman spectroscopy cannot be used to reliably distinguish between them.

The presence of water in charleshatchettite was further investigated by infrared spectroscopy, given that water is a weak Raman scatterer but a strong absorber of infrared radiation. An infrared (FTIR) spectrum (Fig. 5-4) over the range of 600 to 4000 cm^{-1} was collected using a Bruker Alpha spectrometer equipped with a KBr beam splitter and a DTGS detector. This spectrum, obtained by averaging 128 scans with a resolution of 4 cm^{-1}, reveals three distinct bands in the regions of ~3700 – 2800, 1700 – 1300, and 1200 – 650 cm^{-1} (Table 5-2). The region at ~3700 – 2800 cm^{-1} consists of broad, high intensity peak at 3362 cm^{-1} as well as two sharp, moderate intensity peaks at 2923 and 2852 cm^{-1} associated with O-H bending (Williams 1995). The second region at ~1700 – 1300 cm^{-1} consists of a sharp peak at 1654 and 1450 cm^{-1} as well as a sharp lower intensity peak at and 1384 cm^{-1} associated with H-O-H bending and atmospheric CO_2, respectively. The third region at 1200 – 650 cm^{-1} consists of two sharp, high intensity peaks at 934 and 874 cm^{-1}, as well as lower intensity peaks at 1100, 1025, 755, and 697 cm^{-1}. The bands in this region are similar to those in the IR spectra of franconite $[Na(Nb_2O_5)(OH)\cdot 3H_2O]$ with peaks at 1025, 934 and 874 cm^{-1} associated with possible Nb=O double bonds and the peaks at 755 and 697 cm^{-1} associated with Nb-O-Nb single bonds (Fielicke *et al*. 2003, Haring & McDonald 2014). The weak peak at 1100 cm^{-1}, attributed to a Si-O asymmetric stretch, is considered to be due to trace amounts of silicates such as quartz or albite,

both of which are associated with charleshatchettite. There is overall good agreement between the complimentary Raman and FTIR spectra collected for charleshatchettite. The low-intensity peak observed at 1459 cm^{-1} in the Raman spectrum of charleshatchettite, attributed to H-O-H bending, corresponds to the peak at 1450 cm^{-1} in the FTIR spectrum. Other bands observed in the Raman spectrum of charleshatchettite that correspond to those present in the FTIR spectrum include those in the regions of 2900 – 3600 cm^{-1} (O-H bending) as well as 1000 – 850 (Nb=O bonds). However, given the chemical and structural similarities among FGM, the Raman spectra of these minerals are virtually identical, all with two sharp, strong peaks in the regions of 1000 - 850 and 670 - 475 cm^{-1}(Nb-O bonds) as well as a broad peak in the region of 2900 - 3600 cm^{-1}.

5.7 X-ray Crystallography and Crystal-Structure Determination

X-ray powder diffraction data were collected using a 114.6 mm diameter Gandolfi camera, a 0.3 mm collimator, and Fe-filtered Co*K*α radiation (λ = 1.7902 Å). Intensities were determined using a scanned image of the pattern and normalized to the measured intensity of d = 10.308 Å (I = 100). The measured intensities were compared to a pattern calculated using results from the crystal-structure analysis and the program CRYSCON (Dowty 2002) and overall, there is a good agreement between the two (Table 5-3). It is worth noting that charleshatchettite and hochelagaite have significantly different PXRD patterns (Table 5-3), making distinguishing between them straightforward and supporting them as being distinct species.

To obtain a crystal suitable for single-crystal XRD, individual crystals were separated from a coarse-grained, charleshattchetite-bearing globule and examined optically with a polarizing-light microscope. From these, a crystal with the dimensions 0.09 x 0.03 x 0.01 mm, exhibiting a simple extinction and no evidence for twinning was selected. X-ray intensity data were collected

on a Bruker D8 three-circle diffractometer equipped with a rotating-anode generator, multi-layer optics incident beam path and an APEX-II CCD detector. X-ray diffraction data were collected to 60° 2θ using 20 s per 0.3° frame and with a crystal-to-detector distance of 5 cm. The unit-cell parameters for charleshatchettite, obtained by least-squares refinement of 4160 reflections ($I > 10\sigma I$), are a = 21.151(4) b = 6.496(2) c = 12.714(3) Å and β = 103.96(3) ° (Table 5-4), are very similar to those of hochelagaite (Table 5-5). An empirical absorption correction (SADABS; Sheldrick, 1997) was applied and equivalent reflections merged to give 1106 unique reflections covering the entire Ewald sphere.

Solution and refinement of the crystal structure of charleshatchettite were done using SHELXL–97 (Sheldrick 1997). The crystal structure was solved using direct methods, using the scattering curves of Cromer & Mann (1968) and the scattering factors of Cromer & Liberman (1970). Phasing of a set of normalised structure factors gave a mean value of $|E^2 - 1|$ value of 0.908, consistent with a center of symmetry being present {$|E^2 - 1|$ = 0.968 for centrosymmetric, $|E^2 - 1|$ = 0.736 for non-centrosymmetric}. Based on this and the space-group choices available, *C*2/*c* (#15) was chosen as the correct space group. Phase-normalised structure factors were used to give a Fourier difference map from which two *Nb*, and several *O* sites were located. The *Ca* site and additional *O* sites were identified from subsequent Fourier difference maps. Refinement of the site-occupancy factors (SOF) indicated that all of the cation and anion sites were fully occupied (Table 5-6). Determination of which *O* sites were occupied by OH or H_2O was based on a bond-valence analysis (Table 5-7). Some of the *O* sites were found to have low bond-valence sums (*i.e.*, BVS = 1.500 – 1.800 *v.u.*) probably due to the presence of OH at these sites. Hydrogen sites were located for OH as well as the OW7, OW8, and OW10 groups however, the

H atom sites could not be located for the OW9 site. This is due to the positional disorder of the oxygen associated with OW9. Refinement of this final model converged to R = 5.39 % and wR^2 = 13.89 %.

5.8 Description of Crystal Structure

The crystal structure of charleshatchettite contains one unique *Ca* site and two *Nb* sites. Results from the refined-crystal structure and EMPA data indicate that both the *Ca* and *Nb* sites are fully occupied. The *Ca* site is [8]-coordinated by four crystallographically distinct H_2O groups, forming $Ca(H_2O)_8$ polyhedron. Of the H_2O groups, one in particular, OW9, showed a pronounced electron density spread of 0.64 Å along [010]; it was subsequently modelled as a split site, OW9a and OW9b (Table 5-6). Refinement of this model gave SOFs of 0.63(2) and 0.37(3) for the two split sites, suggesting a relatively high degree of disorder for the OW9 site. There are two *Nb* sites both in octahedral coordination with O atoms and OH groups: $Nb(1)O_5(OH)$ and $Nb(2)O_4(OH)_2$. The two Nb polyhedra are highly distorted with Nb-(O,OH) bond lengths ranging from 1.749(2) to 2.352(9) Å and 1.823(9) to 2.281(9) Å, respectively (Table 6-8); this range is consistent with the range in Nb-O bond distances previously observed in franconite (Haring & McDonald 2014) and in other Nb-bearing minerals. These distorted octahedra are likely the result of edge sharing Nb octahedra (see discussion below) which contain a highly charged cation. In both Nb polyhedra, the longest bonds are associated with Nb-OH bonds whereas the shortest bonds are associated with Nb-O bonds.

The Nb polyhedra are linked through shared edges to form four-membered clusters composed of two $Nb(1)O_5(OH)$ and two $Nb(2)O_4(OH)_2$ octahedra (Fig. 5-5). Each cluster is subsequently linked to six adjacent clusters through shared corners generating 4 x 4 Å pore spaces and forming

infinite sheets parallel to [100]. The sheets parallel to [100] correlate with the flattened aspect of crystals and the perfect cleavage in that direction. The layers of $Nb(O,OH)_6$ octahedra alternate with those containing $Ca(H_2O)_8$ polyhedra along [100] with an interlayer spacing of ~ 4 Å (Fig. 5-6).

5.9 Related Structures

The crystal structure of charleshatchettite is topologically similar to that of franconite (Haring & McDonald 2014). Both minerals are hydrous with an $[Nb_2O_5(OH)]^{-1}$ group, the two differing by the type of interlayer cation between the $[Nb_2O_5(OH)]^{-1}$ sheets: charleshatchettite having $Ca(H_2O)_8$ polyhedra and franconite with $NaO(H_2O)_4$ polyhedra (Haring & McDonald 2014). The presence of $Ca(H_2O)_8$ polyhedra in charleshatchettite and the flipping in the octahedral layers correlates with a doubling of the *a* dimension to 21.151 Å compared to franconite where *a* = 10.119 Å as there are additional H_2O groups coordinated with Ca compared with Na in $NaO(H_2O)_4$. Both charleshatchettite and franconite possess crystal structures with layers of $A(H_2O)_{5\text{-}8}$ (*A* = Na,Ca) linked to layers of $Nb(O,OH)_6$octahedra through H-bonds along [100], the latter producing the perfect [100] cleavage observed in these minerals. Chemically, charleshatchettite $[CaNb_4O_{10}(OH)_2 \cdot 8H_2O]$ most closely resembles hochelagaite ($CaNb_4O_{11} \bullet nH_2O$), but as mentioned above, the two have unique PXRD patterns (Table 6-3). The crystal structure of hochelagaite is unknown but is presumed to be similar to those of franconite and chaleshatchettite. It is however noteworthy that the PXRD pattern for hochelagaite has systematic extinctions that support the mineral having a *P*-lattice, which is different from the *C*-lattice in charleshatchettite. The difference in lattice types between the two

may be attributed to the higher proportion of H_2O groups in charleshatchettite relative to hochelagaite.

The crystal structure of charleshatchettite is broadly similar to those of the synthetic compounds $Na_2Nb_4O_{11}$ (Masó *et al*. 2011) and $KCa_2Nb_3O_{10}$ (Fukoka *et al*. 2000, Jehng & Wachs 1990) and Sandia Octahedral Molecular Sieves (SOMS) [$Na_2Nb_{2-x}Ti_xO_{6-x}(OH)_x \bullet H_2O$ (x = 0.04 to 0.40); Nyman *et al*. 2001]. These compounds have strongly layered structures where layers of $Nb(O,OH)_x$ (X = 6 or 7) polyhedra alternate with layers of MO_x (X = 6 or 7; M = Na, K, and Ca) polyhedra. Both SOMS and $Na_2Nb_4O_{11}$, like charleshatchettite, are monoclinic in symmetry and crystallize in the space group $C2/c$ (Nyman *et al*. 2001; Masó *et al*. 2011), whereas $KCa_2Nb_3O_{10}$ is orthorhombic, crystallizing in the space group *Cmcm* (Fukoka *et al*. 2000). Unlike the structures of SOMS and charleshachettite, $KCa_2Nb_3O_{10}$ is considered to have a layered perovskite-type structure where slabs of corner-sharing NbO_6 octahedra and Ca ions alternate along [010] with layers of K ions (Fukoka *et al*. 2000). In the case of $Na_2Nb_4O_{11,}$ layers of edge-sharing $(Nb,Ta)O_7$ polyhedra alternate with layers composed of edge-sharing NaO_7 and $(Nb,Ta)O_6$ polyhedra (Masó *et al*. 2011). Of the synthetic compounds, charleshatchettite is most crystallochemically similar to SOMS. The crystal structures of SOMS contain NbO_6 polyhedra consisting of a short bond of ~1.8 Å, a long bond of ~ 2.4 Å as well as four equatorial bonds with distances of ~ 2 Å (Nyman et al. 2002), similar to the $Nb(1)O_5(OH)$ polyhedra in charleshatchettite. These NbO_6 octahedra, like those in charleshatchettite, form four-membered clusters through shared edges. Adjacent four-membered NbO_6 clusters do not link to form infinite NbO_6 sheets as in charleshatchettite, but are instead linked to double chains of NaO_6 octahedra through shared edges. The four-membered NbO_6 clusters and NaO_6 double chains occur in discreet layers which alternate with one another along [001] (Xu *et al*. 2004). As in

charleshatchettite, the crystal structures of SOMS are linked together in part by H-bonds and are able to adsorb extra water into its structure. The amount of H-bonding in the structures of SOMS increase with increasing Ti substitution for Nb due to the substitution reaction $Ti^{4+} + OH^{-} \leftrightarrow Nb^{5+} + O^{2-}$, whereby more OH groups are added with the addition of Ti into the structure (Nyman et al. 2002). The compounds $Na_2Nb_4O_{11}$ and $KCa_2Nb_3O_{10}$ have been synthesized at high temperatures (~1100 – 1300 °C) while SOMS have been hydrothermally synthesized under conditions of at low *T* (~ 175 °C) and high alkalinity (pH ~ 13.7) (Xu *et al*. 2004). However, increasing the Ti content in SOMS increases the range in *T* over which the structures are stable: a 20% Ti substitution for Nb results in the structures being stabilized up to 576 °C (Nyman *et al*. 2002). The compounds $Na_2Nb_4O_{11}$ and $KCa_2Nb_3O_{10}$ have distinct ferroelectric and dielectric properties (Masó *et al.* 2011, Yim *et al*. 2013). On the other hand SOMS, exhibit a strong ion-exchange selectivity for R^{2+} cations over R^{+} cations, making them useful in removing heavy metals such as Pb^{2+}, Co^{2+} and Cd^{2+} from ground water and soils (Nyman *et al*. 2001), these being trapped in pores of the Nb clusters. Due to the strong crystallochemical similarities between charlreshatchettite and SOMS, charleshatchetttite is expected to have similar cation exchange properties. Such cation exchange properties are supported by the range of chemistries observed for FGM [*i.e*., incorporation of Na, Ca, Mg, +/- Sr, +/- Fe^{2+} into FGM structures; Jambor *et al*. 1984, Jambor *et al*. 1986, Subbotin *et al*. 1997, Haring & McDonald 2014].

5.10 Origin and Conditions of Formation

Paragenetically, charleshatchettite is a late-stage phase found overgrowing earlier formed phases including, albite, quartz, siderite, muscovite, pyrrhotite and ancylite-(Ce). The mineral, due its hydrous composition, is inferred to have precipitated from aqueous fluids. Previous studies of

franconite and hochelagaite, using results from microprobe and mass spectrometry, have shown that the water content can be variable in these minerals, with the number of H_2O groups (*apfu*) ranging from 3 - 26 for franconite and 3 – 9 for hochelagaite (Jambor *et al*. 1984, 1986). Previous heating experiments of Jambor *et al*. (1984) on franconite to temperatures of 150, 250, 350, and 500 °C coupled with PXRD data, reveal a gradual collapse of the structure up to 500 °C at which point the material was found to give a PXRD consistent with that of $Na_2Nb_4O_{11}$. The collapse of the franconite structure is attributed to the loss of H_2O groups: the removal of H_2O groups would result in the loss of H-bonding that bind layers of $Nb(O,OH)_6$ octahedra to layers of $Na(O,H_2O)_5$ polyhedra, thus leading to structural collapse. As H-bonds are essential in stabilizing the crystal structure of franconite, they are also inferred to be equally important in stabilizing the crystal structure of charleshatchettite. It follows, therefore, that heating of charleshatchettite should also lead to a collapse in the crystal structure similar to that observed to in franconite. Given the ease with which franconite loses its structurally bound H_2O and the fact that charleshatchettite shows a greater degree of hydration (H_2O_{calc} = 22.96 wt. %) relative to hochelagaite (H_2O_{calc} = 13.20 wt. %), it is possible that charleshatchettite formed at either a lower *T* (< 150 °C) or under conditions of higher aH_2O, relative to hochelagaite. The presence of coexisting siderite and pyrrhotite suggest that the fluids were slightly reducing (Eh = 0.0 to -0.4) with a neutral to slightly basic pH (pH = 7 to 8) [at a *T* of 25 °C] (Vaughan 2005; Faure 1991). Due to the crystallochemical similarities between charleshatchettite and SOMS and the fact that SOMS are synthesized at a very high pH, it is probable that the fluids from which charleshatchettite precipitated were also highly alkaline.

5.11 Genetic Implications

Charleshatchettite has strong crystallochemical similarities to other FGM and as such should be considered a new member. This broadens the number of related minerals and demonstrates the crystal-chemical flexibility of FGM crystal structure. Although the crystal structures of the FGM are flexible, no Ti- or Zr-dominant members of the FGM have been found to date, despite Ti and Zr having valences and atomic radii ($^{[6]}Ti^{4+}$ = 0.61 Å, $^{[6]}Zr^{4+}$ = 0.72 Å) similar to those of Nb ($^{[6]}Nb^{5+}$ = 0.64 Å) [Shannon 1976]. The SOMS can incorporate other high-field strength elements like Ti and Zr through the substitution: Ti^{4+} (or Zr^{4+}) + OH^{-} ↔ Nb^{5+} + O^{2-} (Nyman *et al*. 2002, Xu *et al*. 2004). In light of the crystal-chemical similarities between SOMS and charleshatchettite, the occurrence of Ti- or Zr-dominant FMG would seem plausible; however such phases have yet to be discovered. It is noteworthy that the crystal structure of SOMS can only incorporate up to 20% Ti or Zr after which the octahedral sites become increasingly distorted and disordered as observed in the broadening of octahedral peaks in the infrared spectrum of SOMS (Nyman *et al*. 2002). The degree of Ti/Nb substitution in FGM varies from 0.25 to 8.00 %, suggesting that a similar distortion and disordering of the octahedral sites may occur in charleshatchettite; this may thus preclude the crystallization of Ti- and Zr-rich members of the FGM. Incorporation of Ti may also proceed through the substitution Ti^{4+} + OH^{-} ↔ Nb^{5+} + O^{2-}; such a substitution in charleshatchettite is supported by the fact that some of the O sites are have low bond-valence sums (i.e., BVS ~ 1.5 – 1.8 *v.u*), suggesting the presence of mixed O/OH sites.

Charleshatchettite is a late-stage mineral that probably developed from a Nb-rich precursor that would have been unstable in the presence of highly alkaline, slightly reducing, aqueous fluids. Presumably, the precursor mineral itself would have been both Nb-dominant and virtually devoid

of Ta, similar to the chemistry of charleshatchettite. A similar paucity of Ta is observed in other Nb-rich minerals such as vuonnemite [$Na_{11}Ti^{4+}Nb_2(Si_2O_7)_2(PO_4)_2O_3(F,OH)$; Ercit *et al*. 1998], epistolite [$Na_4Nb_2Ti^{4+}(Si_2O_7)_2O_2(OH)_2(H_2O)_4$; Sokolova & Hawthorne 2004], laurentianite {$[NbO(H_2O)]_3(Si_2O_7)_2[Na(H_2O)_2]_3$; Haring *et al*. 2012}, and franconite [$NaNb_2O_5(OH)\bullet 3H_2O$; Haring & McDonald 2014], laurentianite (from agpaitic environments, suggesting that Ta and Nb must undergo significant fractionation prior to late-stage crystallization in agpaitic environments. Possible precursor minerals to charleshatchettite include pyrochlore- or eudialyte-group minerals or possibly vuonnemite. Interactions of fluids with these precursor minerals, especially vuonnemite which is highly susceptible to weathering (Khomyakov *et al*. 1975b, Bussen *et al*. 1978), would have led to an Nb-enrichment of these the fluids. Evidence for the mobility of Nb in agpaitic environments can be seen in the paragenetic relationship between the Nb minerals laurentianite ($[NbO(H_2O)]_3(Si_2O_7)_2[Na(H_2O)_2]_3$) and franconite, whereby laurentianite overgrows the latter (Haring & McDonald 2012). In addition to Nb-enrichment, these fluids could have also been enriched in Ca possibly due to interaction with the carbonate rocks into which the Mont Saint-Hilaire syenites intruded.

5.12 References

Brese, N.E. & O'Keeffe, M. (1991): Bond-valence parameters for solids. Acta Crystallographica, B47, 192-197.

Bussen, I.V., Es'kova, E.M., Men'shikov, Yu.P., *et al*. (1978): The mineralogy of hyperalkaline pegmatites. Problems of Geology of Rare Elements, M., 251-271.

Chao, G.Y., Conlon, R.P. & VanVelthuizen, J. (1990): Mont Saint-Hilaire unknowns. Mineralogical Record, 21, 363-368.

Cromer, D.T. & Liberman, D. (1970): Relativistic calculation of anomalous scattering factors for X rays. Journal of Physical Chemistry, 53, 1891-1898.

Cromer, D.T. & Mann, J.B. (1968): X-ray scattering factors computed from numerical Hartree-Frock wave functions. Acta Crystallographica, A24, 321-324. ces, 44: 1333-1346.

Dowty, E. (2009): *VIBRATZ for Windows and Macintosh Version 2.2*. Shape Software Kingsport, Tennessee, USA.

Dowty, E. (2002): *CRYSCON for Windows and Macintosh Version 1.1*. Shape Software Kingsport, Tennessee, USA.

Ercit, T.S., Cooper, M.A. & Hawthorne, F.C. (1998): The crystal structure of vuonnemite, $Na_{11}Ti^{4+}Nb_2(Si_2O_7)_2(PO_4)_2O_3(F,OH)$, a phosphate-bearing sorosilicate of the lomonosovite group. Canadian Mineralogist, 36, 1311-1320.

Faure, G. (1991): Principles and applications of geochemistry 2nd ed. Prentice Hall. pp 243.

Frisch,M. J., Trucks, G. W. Schlegel, H. B., *et al*. (2013): *Gaussian 09, Revision D.01*. Gaussian, Inc., Wallingford CT.

Haring, M.M. & McDonald A.M. (2014): Franconite, $NaNb_2O_5(OH)\cdot 3H_2O$: structure determination and the role of H bonding, with comments on the crystal chemistry of franconite-related minerals. Mineralogical Magazine, 78, 591-607.

Haring, M.M.M., McDonald, A.M., Cooper, M.A. & Poirier, G.A. (2012): Laurentianite, $[NbO(H_2O)]_3(Si_2O_7)_2[Na(H_2O)_2]_3$, a new mineral from Mont Saint-Hilaire, Québec: description, crystal-structure determination and paragenesis. The Canadian Mineralogist, 50, 1265-1280.

Horváth, L. & Gault, R.A. (1990): The mineralogy of Mont Saint-Hilaire Québec. Mineralogical Record, 21, 284-359.

Jambor, J.L., Sabina, A.P., Roberts, A.C., Bonardi, M., Owens, D.R. & Sturman, B.D. (1986): Hochelagaite, a new calium-niobium oxide mineral from Montreal, Québec. Canadian Mineralogist, 24, 449-453.

Jehng, J.M. & Wachs I.E. (1990): Structural chemistry and Raman spectra of niobium oxides. Chemistry of Materials., 3, 101-107.

Khomyakov, A.P., Semenov, E.I., Es'kova, E.M., *et al*. (1975b): Vuonnemite from Lovovzero. Iz.AN,ser.geol, 8, 78-87.

Kontny, A., de Wall, H., Sharp, T.G., & Posfai, M. (2000): Mineralogy and magnetic behavior of pyrrhotite from a 260°C section at the KTB drilling site, Germany. American Mineralogist, 85, 1416 – 1427.

Mandarino J. A. (1981): The Gladstone–Dale relationship. IV. The compatibility concept and its application. Canadian Mineralogist, 19,441-450.

Masó, N., Woodward, D.I., Várez, A. & West, A.R. (2011): Polymorphism, structural characterization and electrical properties of $Na_2Nb_4O_{11}$. Journal of Material Chemistry, 21, 12096-12102.

Nyman, M., Tripathi, A., Parise, J.B., Maxwell, R.S., Harrison, W.T.A. & Nenoff, T.M. (2001): A new family of octahedral molecular sieves: Sodium Ti/Zr^{IV} niobates. Journal of the American Chemical Society, 123, 1529-1530.

Shannon, R.D. (1976): Revised effective ionic radii and systematic studies in interatomic distances in halides and chalogenides. Acta Crystallographica, A32, 751-767.

Sokolova, E. & Hawthorne, F.C. (2004): The crystal chemistry of epistolite. Canadian Mineralogist, 42, 797-806.

Subbotin, V.V., Voloshin, A.V., Pakhomovskii, Y.A., Men'shikov, Y.P. & Subbotina, G.F. (1997): Ternovite, (Mg,Ca)Nb_4O_{11}•nH_2O, a new mineral and other hydrous tetraniobates from carbonatites of the Vuoriyarvi massif, Kola Peninsula, Russia. Neues Jahrbuch für Mineralogie, 2, 49-60.

Vaughan, D. J., (2005): Minerals/Sulphides. In Encyclopedia of geology. Amsterdam: Elsevier, 574–586.

Williams, Q. (1995): Infrared, Raman and opticalspectroscopy of Earth materials. Pp. 291 -302 in: Mineral Physics and Crystallography: a Handbook of Physical Constants (T.J. Ahrens, editor), AGU Reference Shelf Vol 2. American Geophysical Union, Washington, D.C.

Xu, H., Nyman, M., Nenoff, T.M. & Navrotsky, A. (2004): Prototype sandia octahedral molecular sieve (SOMS) $Na_2Nb_2O_6$•H_2O: Synthesis, structure and thermodynamic stability. Chemistry of Materials, 16, 2034-2040.

Yim, H., Yoo, S., Nahm, S., Hwang, S., Yoon, S. & Choi, J. (2013): Synthesis and dielectric properties of layered $HCa_2Nb_3O_{10}$ structure ceramics. Ceramics International, 39, 611-614.

Mineral	Time →
Albite	
Quartz	
Siderite	
Muscovite	
Pyrrhotite	
Pyrite	
Ancylite–(Ce)	
Charleshatchettite	

Figure 5-1. Mineral paragenesis for charleshatchettite.

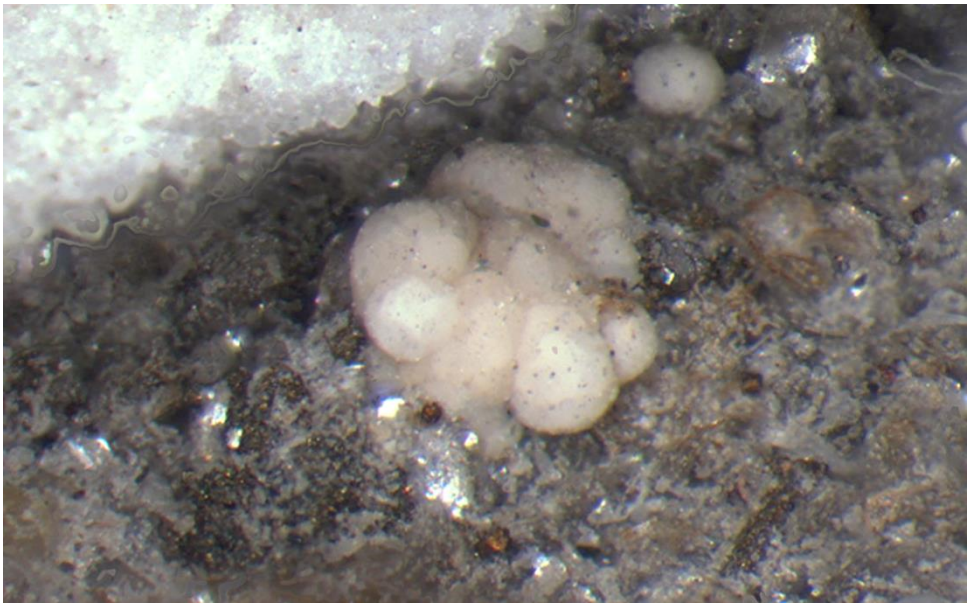

Figure 5-2. Globules of charleshatchettite with muscovite, siderite, and pyrrhotite.

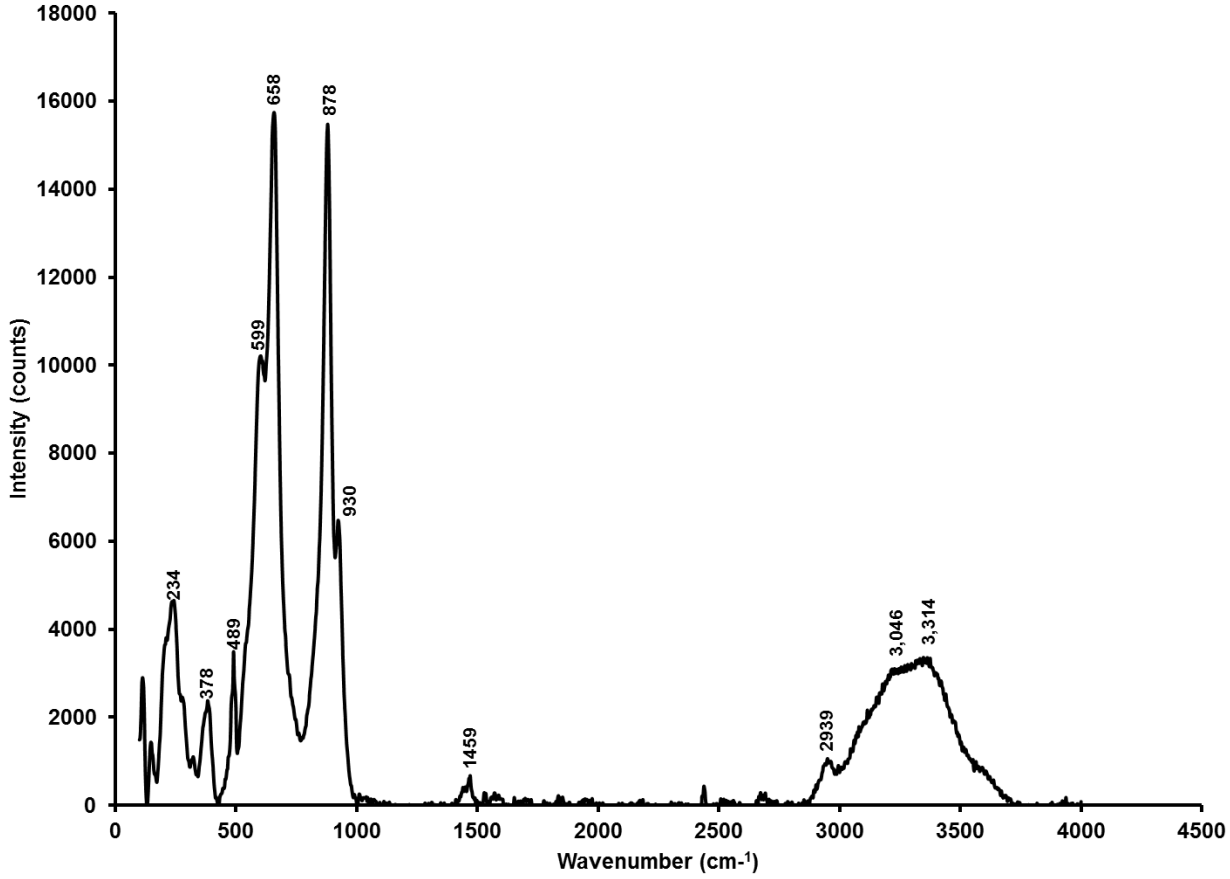

Figure 5-3a. Raman spectrum for charleshatchettite perpendicular to [100].

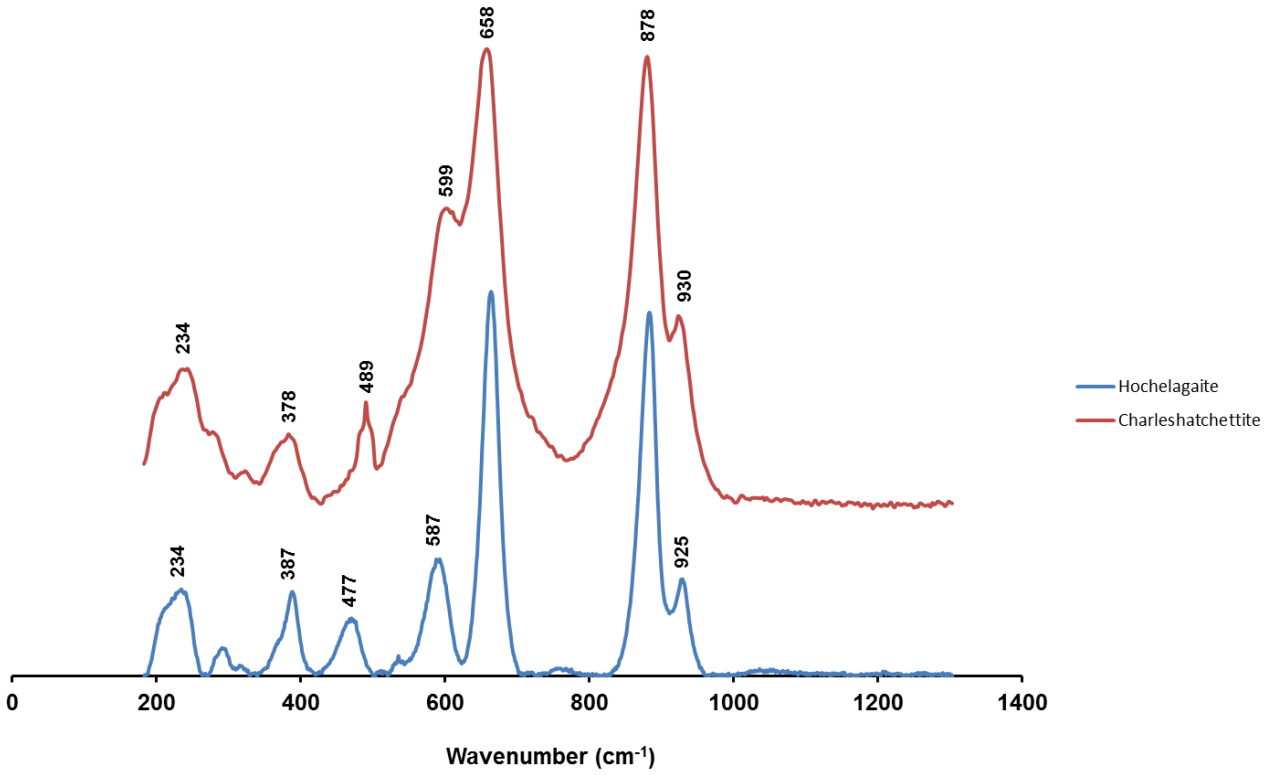

Figure 5-3b. Raman spectra for charleshatchettite and hochelagaite.

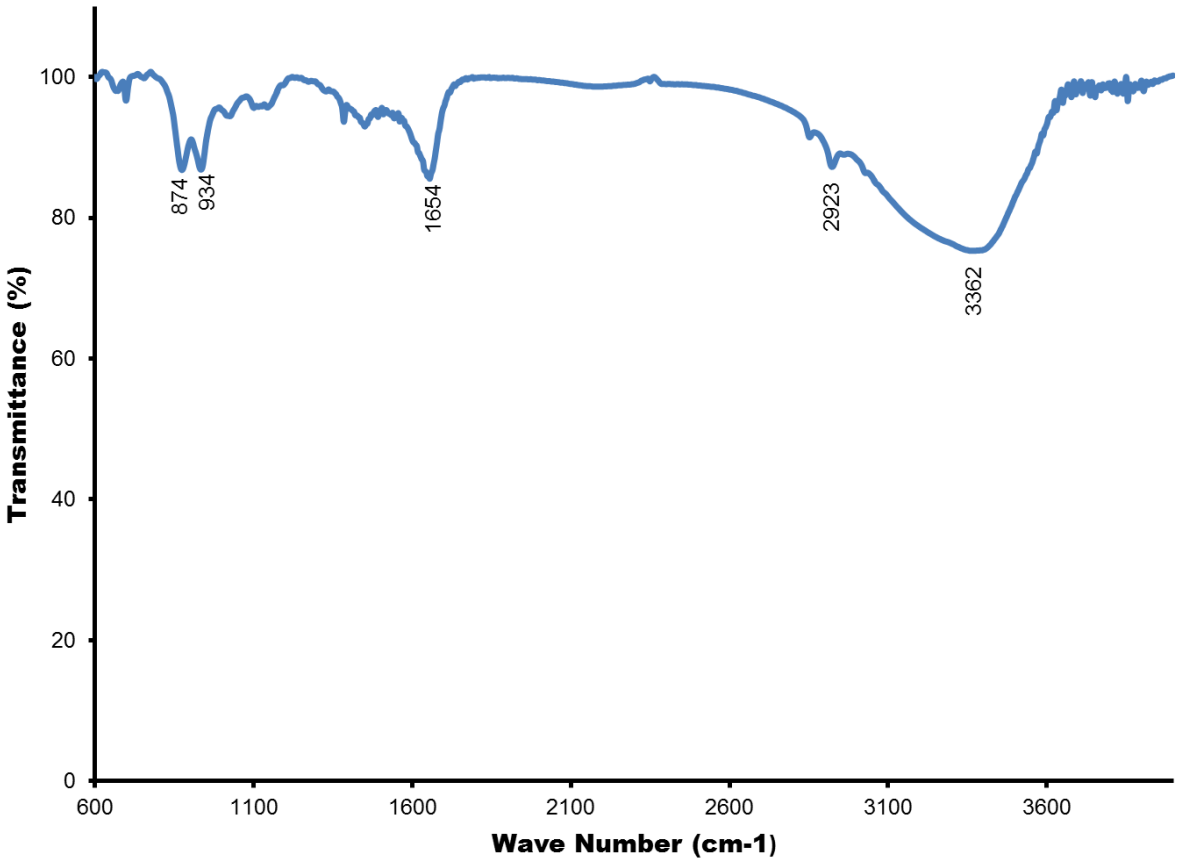

Figure 5-4. FTIR spectrum for charleshatchettite.

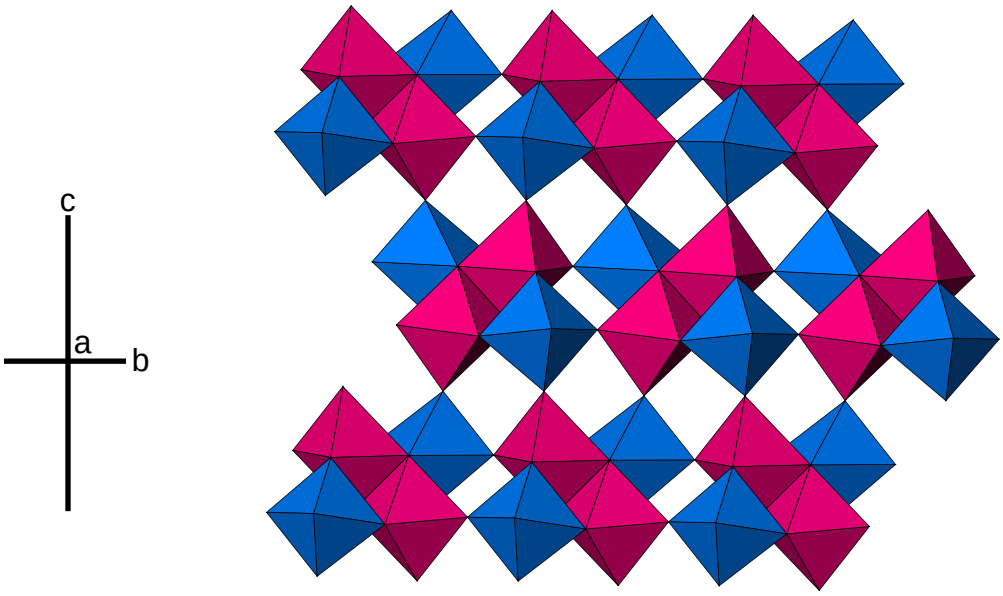

Figure 5-5. The crystal structure of charleshatchettite viewed along [100]. The $Nb(1)O_5(OH)$ (blue) and $Nb(2)O_4(OH)_2$(pink) octahedra are linked through shared edges to form four-membered clusters. The clusters are then joined through shared corners to adjacent ones, leading to development of infinite sheets in the *b*-*c* plane.

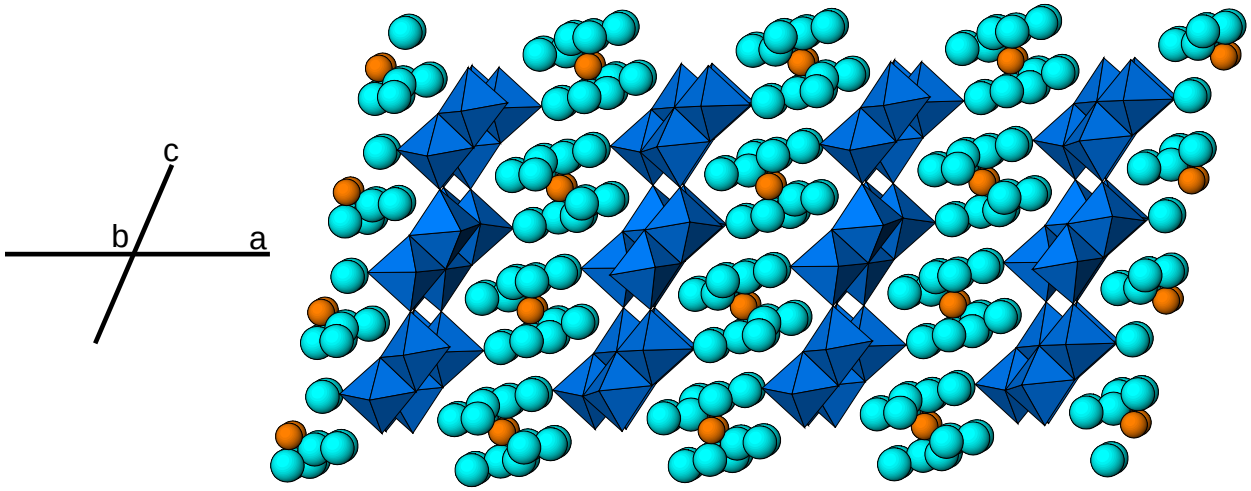

Figure 5-6. The crystal structure of charleshatchettite viwed along [010]. Layers composed of $Nb(O,OH)_6$ octahedra alternate along [100] with layers composed of Ca atoms (orange) and H_2O (light blue). Weak H-bonding between the layers results in the perfect {100} cleavage observed in the mineral.

Table 5-1. Observed Raman absorption bands for charleshatchettite and hochelagaite.

Hochelagaite*	Charleshatchettite				
Peak Position (cm^{-1})	Peak Position (cm^{-1})	Peak Position calc. (cm^{-1})	Width	Intensity	Assignment
	3314		Broad	Mod.Strong	O-H bending
	3046		Broad	Mod. Strong	O-H bending
	2939		Mod. Sharp	Weak	O-H bending
	1459		Mod. Sharp	Weak	H-O-H bending
925	930	946	Sharp	Mod. strong	Symmetric stretching of Nb=O double bond
878	878	855	Sharp	Very strong	Symmetric stretching of Nb=O double bond
663	658	678	Sharp	Very strong	Nb-O-Nb linkages – symmetric stretching
587	599	607	Sharp	Mod. strong	Nb-O-Nb linkages – symmetric stretching
477	489	455	Mod. Sharp	Weak	Ca-O
387	378	355	Mod. Sharp	Weak	Ca-O
325	234	288	Sharp	Weak	Ca-O
300	215	-	Sharp	Mod. strong	Ca-O
234	205	183	Sharp	Weak	Ca-O
196	150	-	Mod. Sharp	Weak	Ca-O
-	115	-	Sharp	Mod. strong	Ca-O

* Raman data for hochelagaite from this study.

Table 5-2. FTIR peaks and peak assignments for charleshatchettite

FTIR Transmittance band (cm^{-1})	Suggested Assignment
3362	O-H Bending
2923	O-H Bending
2852	O-H Bending
1654	H-O-H Bending
1450	H-O-H Bending
1384	Atmospheric CO_2
1100	asymmetric Si-O stretching
1025	Symmetric stretching of Nb=O double bond
934	Symmetric stretching of Nb=O double bond
874	Symmetric stretching of Nb=O double bond
755	Nb-O-Nb linkages - symmetric stretching
697	Nb-O-Nb linkages - symmetric stretching
666	Nb-O-Nb linkages - symmetric stretching

Table 5-3. X-ray powder diffraction data for charleshatchettite and hochelagaite.

Charleshattchetite							Hochelagaite[1]						Charleshattchetite							Hochelagaite[1]				
I_{obs}	I_{calc}	d_{obs}(Å)	d_{calc} (Å)	h	k	l	I_{obs}	d_{obs}(Å)[1]	h	k	l		I_{obs}	I_{calc}	d_{obs}(Å)	d_{calc} (Å)	h	k	l	I_{obs}	d_{obs}(Å)[1]	h	k	l
100	**100**	**10.308**	**10.263**	**2**	**0**	**0**	**100**	**10.00**	**2**	**0**	**0**		20	4	2.697	2.69	2	2	2	5	2.693	4	4	0
																						-5	3	1
12	3	6.199	6.193	1	1	0	20	6.18	-1	0	1			1		2.684	1	1	4					
							<5	5.61	-1	1	1			13		2.676	7	1	-2					
							50	**5.39**	**2**	**2**	**0**		6	5	2.593	2.582	5	1	-4	5	2.606	3	4	1
14	12	5.165	5.132	4	0	0	**50**	**4.96**	**4**	**0**	**0**									20	2.541	7	0	1
																						-4	2	2
38	**24**	**4.832**	**4.801**	**2**	**0**	**2**														<5	2.492	5	4	0
39	**30**	**4.731**	**4.711**	**3**	**1**	**0**																7	1	1
							<5	4.61	3	2	0		5	1	2.283	2.277	7	1	2	10	2.276	5	2	2
16	2	4.556	4.539	1	1	-2								3		2.27	2	2	-4					
	12		4.517	4	0	-2														20	2.232	-2	4	2
							10	4.48	3	0	1		7	1	2.207	2.196	4	2	-4	<5	2.197	-6	4	1
5	5	4.244	4.22	1	1	2	20	4.24	3	1	1			6		2.193	9	1	-2			2	4	2
3	3	4.106	4.086	3	1	-2							2	2	2.166	2.152	9	1	0					
							20	3.93	2	3	0		4	1	2.12	2.117	2	0	-6					
									4	2	0			1		2.112	1	3	1					
							5	3.61	3	3	0		**27**	**4**	**2.071**	**2.064**	**3**	**3**	**0**	20	2.085	9	2	0

6	4	3.56	3.547	4	0	2							**6**		**2.061**	**3**	**3**	**-1**				
	1		3.534	5	1	-1							**6**		**2.056**	**0**	**0**	**-6**				
12	9	3.492	3.476	3	1	2	10	3.5	1	3	1	3	1	2.017	2.011	3	1	-6	20	2.02	-8	0	2
	2		3.47	5	1	0							2		2.002	2	2	-5					
15	1	3.352	3.355	6	0	-2													30	1.979	-2	5	2
	13		3.329	5	1	-2						7	3	1.934	1.929	2	0	6					
25	**10**	**3.262**	**3.248**	**0**	**2**	**0**													20	1.89	-4	6	1
25	**2**	**3.193**	**3.176**	**5**	**1**	**1**	**70**	**3.208**	**0**	**4**	**0**	4	2	1.846	1.84	11	1	-2					
	16		**3.173**	**2**	**0**	**-4**							1		1.837	7	1	-6					
9	4	3.155	3.141	0	2	-1	5	3.161	1	4	0		1		1.837	11	1	-1					
24	10	3.108	3.097	2	2	0	**80**	**3.115**	**0**	**1**	**2**								5	1.81			
	11		3.085	0	0	-4						7	4	1.785	1.779	3	1	6					
7	5	3.068	3.057	2	2	-1	20	3.059	1	1	2		1		1.776	3	3	-4					
							<5	2.936	-4	3	1								20	1.755			
4	2	2.888	2.874	0	2	-2													10	1.708			
							<5	2.854	4	3	1	5	1	1.702	1.694	7	3	-3	10	1.69			
13	1	2.806	2.803	3	1	-4	**40**	**2.799**	**-2**	**2**	**2**		1		1.692	7	3	1					
	12		2.791	5	1	2							3		1.691	9	1	-6					
8	1	2.755	2.755	4	2	-1																	
	2		2.745	4	2	0																	
	4		2.74	7	1	-1																	

Table 5-4. Miscellaneous single crystal data for charleshatchettite.

a (Å)	21.151(4)	Monochromator	Graphite
b	6.496(2)	Intensity-data collection	θ:2θ
c	12.714(3)	Criterion for observed	
β (º)	103.96(3)	reflections	$F_o > 4\sigma(F_o)$
V (Å^3)	1695.3(6)	GoOF	1.188
Space group	*C*2/*c* (#2)	total No. of reflections	4160
Z	4	No. Unique reflections	1106
D_{calc} (g/cm^3)	2.878	*R* (merge %)	7.85
Radiation	Mo*K*α (50 kV, 40 mA)	*R* %	5.39
		wR^2 %	13.89

Table 5-5. Crystallographic parameters for members of the franconite group.

	Charleshatchettite	Hochelagaite[1]	Franconite[2]	Ternovite[3]
a (Å)	21.151(4)	19.88(1)	10.119(2)	20.656
b (Å)	6.496(1)	12.83(1)	6.436(1)	13.062
c (Å)	12.714(3)	6.44(1)	12.682(2)	6.388
β (°)	103.958(3)	93.20(3)	99.91(3)	90.917
V(Å^3)	1695.28(1)	1655.89(1)	813.6(1)	1709.83
Z	4	4	4	4
Space Group	*C*2/*c* (#15)	unknown	$P2_1/c$	*P*2/*m*, *P*2, *Pm*

1) Jambor *et al*. 1986
2) Haring & McDonald 2014
3) Subbotin *et al*. 1997

Table 5-6. Positional and displacement parameters for charleshatchettite.

ATOM	*x*	*y*	*z*	SOF	U_{11}	U_{22}	U_{33}	U_{23}	U_{13}	U_{12}	U_{eq}
Ca	0	0.0718(6)	3/4	1	0.037(3)	0.010(2)	0.027(3)	0	0.002(2)	0	0.025(1)
Nb(1)	0.32608(6)	0.0272(2)	0.9119(2)	1	0.032(9)	0.0063(8)	0.0136(8)	0.0003(5)	0.0080(6)	0	0.0218(6)
Nb(2)	0.25153(7)	-0.4368(2)	0.8934(2)	1	0.040(2)	0.0086(9)	0.0175(9)	0.0001(5)	0.0088(7)	-0.0002(6)	0.0252 (2)
O(1)	0.4076(5)	0.082(2)	0.9162(8)	1	0.040(7)	0.013(5)	0.025(6)	0.001 (4)	0.004(5)	0.005(5)	0.027(2)
O(2)	0.3304(4)	0.0002(2)	1.0651(7)	1	0.030(6)	0.004(5)	0.013(5)	0.004(4)	0.001(4)	-0.001(4)	0.017(2)
O(3)	0.2844(5)	0.054(2)	0.7526(7)	1	0.045(6)	0.008(5)	0.012(5)	0.002(4)	0.010(5)	0.004(4)	0.021(2)
O(4)	0.3302(4)	-0.275(2)	0.8927(7)	1	0.035(6)	0.003(5)	0.018(5)	0.001(4)	0.007(5)	-0.003(4)	0.019(2)
O(5)	0.2916(5)	0.313(2)	0.9176(7)	1	0.043(7)	0.002(5)	0.019(5)	0.001(4)	0.010(5)	-0.004(4)	0.021(2)
OH(6)	0.2252(5)	-0.111(2)	0.9236(7)	1	0.045(7)	0.015(5)	0.024(6)	-0.004(4)	0.022(5)	-0.005(4)	0.026(2)
OW(7)	0.0499(7)	-0.021(2)	0.598(2)	1	0.089(1)	0.035(7)	0.038(8)	-0.015(6)	-0.001(7)	0.015(7)	0.056(4)
OW(8)	0.0103(5)	0.373(2)	0.8725(8)	1	0.049(7)	0.19(6)	0.031(6)	-0.003(5)	0.017(5)	0.002(5)	0.032(3)
OW(9a)	-0.063(2)	-0.229(5)	0.685(3)	0.63(2)	0.07(2)	0.03(2)	0.08(3)	-0.05(2)	0	0.01(2)	0.06(1)
OW(9b)	-0.058(4)	-0.253(2)	0.640(6)	0.37(3)	0.06(3)	0.10(4)	0.11(5)	-0.11(4)	0.03(3)	-0.01(3)	0.09(2)
OW(10)	0.1212(5)	0.165(2)	0.803(8)	1	0.046(7)	0.026(6)	0.032(6)	-0.006(5)	0.014(5)	-0.013(5)	0.034(3)

Table 5-7. Bond-valence table (*v.u.*) for charleshatchettite.

	Ca	Nb1	Nb2	∑
O1		$1.537^{\downarrow\rightarrow}$		1.537
O2		$0.930^{\downarrow\rightarrow}$	$0.841^{\downarrow\rightarrow}$	1.771
O3		$0.763^{\downarrow\rightarrow}$	$1.245^{\downarrow\rightarrow}$	2.008
O4		$0.817^{\downarrow\rightarrow}$	$0.853^{\downarrow\rightarrow}$	1.670
O5		$0.780^{\downarrow\rightarrow}$	$1.265^{\downarrow\rightarrow}$	2.045
OH6		$0.312^{\downarrow\rightarrow}$	$0.784^{\downarrow\rightarrow}$	1.096
OW7	$0.480^{\downarrow\rightarrow}$			0.480
OW8	$0.498^{\downarrow\rightarrow}$			0.498
OW9*a*	$0.328^{\downarrow\rightarrow}$			0.328
OW9*b*	$0.178^{\downarrow\rightarrow}$			0.178
OW10	$0.408^{\downarrow\rightarrow}$			0.408
∑	1.891	5.139	4.988	

Table 5-8. Interatomic distances (Å) in charleshatchettite

Ca$(H_2O)_8$ Polyhedron			*Nb*(2)$O_4(OH)_2$ Octahedron		
Ca	-OW9*b* x2	2.66(7)	*Nb*2	-O3	1.828(9)
	-OW9*a* x2	2.40(4)		-O5	1.823(9)
	-OW7 x2	2.49(2)		-O4	1.969(9)
	-OW8 x2	2.48(2)		-O2	1.972(9)
	-OW10 x2	2.56(2)		-OH6	2.248(9)
<*Ca*	-O>	2.518		-OH6	2.281(9)
			<*Nb*2	-O>	2.020

Nb(1)O_5(OH) Octahedron		
*Nb*1	-O1	1.749(2)
	-O2	1.936(9)
	-O5	2.004(8)
	-O4	1.985(8)
	-O3	2.012(9)
	-OH6	2.352(9)
<*Nb*1	-O>	2.006

Chapter 6

Quantitative analysis of major concentrations of Li, Be and B in silicate, borosilicate, and borate minerals using LA-ICP-MS

6.1 Abstract

The application of laser ablation ICP-MS (LA-ICP-MS) as a potential alternative to SIMS and other techniques (e.g. SIMS) for quantitative analysis of major concentrations of Li, Be and B has been evaluated. Twelve Li, Be and B bearing minerals; including silicates, borosilicates and borates, representing a range of Li, Be and B compositions were analyzed by quadrupole LA-ICP-MS to test the efficacy of this technique for quantifying the concentration of these light elements. Standards used included the NIST610 and 612 glasses as well as lithium metaborate and natural beryl from Fisher Quarry, Topsham, Maine. The analyses were made using a variety of beam widths (6 to 30 μm) and standards (NIST610 & 612, natural beryl, and lithium metaborate) and were processed using a novel standard-independent approach. Results indicate that the measured Li, Be and B concentrations derived using the NIST610, NIST612, lithium metaborate and beryl standards were in good agreement (i.e., within ± 10 %) with the ideal Li, Be and B compositions for most of the minerals, regardless of beam width used. The measured Li compositions of both polylithionite and tainiolite however, were found to deviate by ~ ± 20 - 30 % of the expected ideal values. Although NIST610 gave measured compositions similar to NIST612, lithium metaborate and beryl, NIST610 was found to be a more suitable standard as the associated errors (1σ error: ± 0.05 to ± 1.68 ppm) were smaller than those of NIST612 (1σ error: ± 0.57 to ±2.47), lithium metaborate (1σ error: ± 0.49 to ± 1.76 ppm) and beryl (1σ error: ± 0.29 to ± 3.65 ppm) for the minerals analyzed. Therefore, this study indicates that NIST610 is a

suitable standard for measuring major concentrations of Li, Be and B. Laser ablation appears to be a suitable method for measuring Be and B in major concentrations. This technique also works for most Li minerals with the exception of Li-rich (Li_2O = 6 wt.%) micas where the discrepancy between ideal and measured Li concentrations can be as high 25%. Such discrepancies are not observed in other Li minerals with Li_2O > 6 wt.%.

6.2 Introduction

Light lithiophile elements (LLE), (i.e., those including to include Li, Be, and B) are characterized by their low atomic masses. They are also highly volatile and readily partition into hydrous fluids making them sensitive tracers of magmatic fluids and thus, helpful in understanding the evolution of magmas and geochemical cycling at subduction zones (Chaussidon & Libourel 1993, Domanik et al. 1993, Leeman & Sisson, 1996, Ryan et al. 1996, Kent & Rossman 2002, Scambelluri et al. 2004). However, the combination of their low atomic masses and general occurrence in low concentrations (ppm to ppb levels) in most lithologies means that the chemical analysis of LLEs and therefore the study of these elements can be challenging (Kent & Ungerer 2006).

Most studies of the LLE in minerals have focused on low-level (ppm) and isotopic concentrations. The number of studies focusing on the LA-ICP-MS analysis of LLE in minerals is relatively limited and includes studies by Tiepolo *et al*. (2005, 2006), Kent & Ungerer (2006). In these studies however, LLE occur only in trace amounts in the minerals analyzed. Tiepolo *et al*. (2005) conducted a comparative study of trace element concentrations of Li, Be, and B in amphiboles using both LA-ICP-MS and SIMS. Their study found that the detection limits for Be and B were ~ 100 ppb and ~200 ppb for Li when using LA-ICP-MS. The data produced in that

study for the LLE were found to be precise, generally falling within 10, 20 and 15% of predicted values respectively, at the 2σ level and overall, the agreement between the LA-ICP-MS and SIMS data were found to be within 10% and 20% relative for Li, Be and B. Kent and Ungerer (2006) also showed that LA-ICP-MS is capable of measuring LLE down to the low ppm to ppb range similar to SIMS but without the significant matrix effects of the latter method.

There are few studies in which LLEs in major concentrations are measured by LA-ICP-MS. These include work on Li-rich micas by Breiter *et al*. 2017, Lichtervelde *et al*. 2008, and Armbruster *et al.* 2007, where Li was measured by LA-ICP-MS using NIST610 as a standard. These studies gave measured Li values that were within ± 5% of expected ideal values provided Li_2O concentrations were ~ 2 wt. %. Although studies on measuring LLE in trace and major concentrations have been conducted, these studies have not evaluated the efficacy of the laser ablation technique in terms of standards and beam widths employed. Both NIST610 and NIST612 glasses were used as standards in these studies however, they contain LLEs in ppm levels, so their efficacy in measuring major concentrations of LLE is unknown. In this study, we will test the effectiveness of LA-ICP-MS at measuring Li, Be, and B that are present as major elements in a variety of minerals including hydrated and anhydrous silicates, borosilicates and borates. It investigates the effect of differing beam sizes (6 to 30 μm) on the obtained data and compares and examines the data produced using different standards, including NIST610, NIST612, scintered Li-metaborate glass ($LiBO_2$) and natural beryl. It also tests the application of a standardless (standard-independent) approach to data reduction (Liu et al. 2008) to hydrated minerals.

6.3 Background

Elements such as Li, Be and B can be analyzed numerous ways including: secondary ion mass spectrometry (SIMS), electron microprobe analysis (EMPA), single-crystal structure refinement (SREF), and laser ablation ICP-MS (LA-ICP-MS). Secondary ion mass spectrometery can be used to measure all elements on the periodic table, including LLEs, and has detection limits down to the ppb range with a precision and accuracy that are better that 2σ at the ppm level (Tiepolo *et al*. 2005). In addition to low-detection limits, SIMS has a very high spatial resolution (i.e., down to 10 μm) which makes it possible to accurately analyze trace elements in very small aliquots (Hervig *et al.* 2006). However, analysis of LLEs in silicate samples by SIMS may be hindered by matrix effects whereby the secondary-ion-intensity and element concentration are not proportional to one another. These can therefore impact on both the accuracy and precision of the results obtained. The specifics of these matrix effects are not understood but both composition and orientation are thought to play roles (Ottolini *et al*. 1993; Ottolini *et al*. 2000). It has also been noted that the LLE are not necessarily affected to the same degree by these matrix effects. For example, Ottolini *et al.* (2002) examined and compared the variations in the concentrations of Li, Be and B in silicate minerals (*e.g*. phenacite, kornerupine, danburite, axinite, spodumene, tourmaline-group minerals, and phengite) through various techniques including SIMS, EMPA and SREF. Results indicated that Be was the least affected, with SIMS derived concentrations in good agreement (≤ 14 % relative) with those derived from EMPA and SREF. At the same time, a greater discrepancy between concentrations of Li (~ 16 – 34 % relative) and B (~ 19 – 23 % relative) measured from SIMS and those measured from EMPA and SREF was noted (Ottolini *et al*. 2002). The discrepancies in Li and B concentrations, measured by the three methods were found also found to correlate with increasing Mn and Fe content in

the samples. Another issue with employing SIMS is that samples must be carefully cleaned by sputtering (for as long as 30 min.) to reduce surface contamination of B derived from polishing compounds as well as water and solvents used for cleaning (*i.e.*, sample preparation is not simplistic; Kent & Ungerer 2006). Finally, SIMS is a relatively expensive technique that is generally difficult to access, as few labs have SIMS instrumentation, both of which can negatively impact the number of analyses that can be made using this technique.

The most commonly employed technique for major, minor and to a certain extent, trace-elements, in minerals is EMPA, this including both wavelength- and energy-dispersive spectrometries. While being able to analyze most elements of the periodic table up to U (Z = 92), it cannot be used to analyze Li and there are severe limitations when attempting to analyze Be (Raudsepp 1995). Analysis by EMPA can be somewhat routinely used to analyze for B, albeit to a limit of detection of 0.3 wt.% B_2O_3 with count times of 3 to 5 min (Raudsepp 1995). The analysis of B by EMPA was first made possible by the introduction of synthetic organic multilayer detection crystals such as lead stearate. These have since been replaced by synthetic inorganic multilayer crystals such as W/Si and Mo/B_4C crystals (Hawthorne *et al*. 1995). Synthetic inorganic multilayer crystals result in much greater peak intensities compared to lead stearate (as much as 2 to 15 times), but they have poorer resolution leading to peak overlap problems (Bastin & Heijligers 1992). The B*K*α peak in borate as well as silicate minerals is broad and it interferes with ClL_i and ClL_n peaks as well as second-order CaL_α and L_β, third-order O*K*α, and fourth-order FeL_α and L_β lines (McGee *et al*. 1991).

The crystal-structure refinement of single-crystal X-ray diffraction (SXRD) is an electron-counting methodology whereby variations in relative scattering power, combined with its spatial resolution, are measured over the average unit-cell of a mineral. During refinement, an absolute X-ray scattering power is assigned to a relatively heavy element, which then correctly scales the scattering power of the other elements in the mineral. This allows the elemental components of the mineral to be identified (Hawthorne *et al*. 1995). The general application, of SXRD to determine the presence of light elements as essential elements in minerals was first discussed by Hawthorne & Grice (1990). This technique is non-destructive and requires a very small amount of sample (i.e. a single crystal). By its very nature, very small quantities of material are required (typically < 200 μm^3), although the material should be single, untwinned and chemically homogenous. For these minerals, it can be time consuming to find true single crystals that are free of twinning.

Another technique useful in the analysis of LLE is laser ablation-ICP-MS (LA-ICP-MS), which is quickly becoming a standard analytical tool in many labs. This technique is capable of measuring most elements on the periodic table including the LLEs with detection limits approaching the ppb level and involves the analysis of small amounts of sample (μg quantities) for which minimal preparation is needed (Jenner & Arevalo, Jr. 2016). Furthermore, this technique both is generally less destructive than other techniques and allows for *in situ* chemical analysis and mapping of minerals (Jenner & Arevalo Jr 2016). Improvements to the overall accuracy of LA-ICP-MS in the analysis of minerals have been recognized through the introduction of short wavelength ultraviolet lasers (i.e. 213 nm Nd:YAG and 193 nm ArF Excimer). These lasers improve the ablation efficiency of minerals resulting in fewer particles too large to be vaporized by ICP (Guillong & Günther 2002). Finally, LA-ICP-MS has a fairly

high spatial resolution (down to tens of μm) making it useful for mapping the spatial distribution of elements in minerals (Jenner & Arevalo Jr 2016). Despite these advantages, LA-ICP-MS does have some disadvantages, such as laser-induced elemental fractionation (LIEF) and elemental interferences (Jenner & Arevalo Jr 2016, Eggins et al. 1998). During ablation of a sample, the signal intensity of the elements analyzed gradually decreases with time however, due to LIEF, the rate of decrease is faster for some elements (e.g., Ca) than others (e.g., Si; Eggins et al. 1998). As a result, measured signal intensities may not be representative of the sample. The effects of LIEF increase with longer ablation times and a decreasing laser pit aspect ratio (Eggins et al. 1998). Elemental interferences result when elements and molecular species share the same mass to charge ratio as the element being analyzed (e.g. oxides, argides or doubly charged ions). If it is known that a certain element has interferences they can be corrected for or in some cases (i.e. with sector field laser ablation systems), mass resolution of the LA-ICP-MS can be increased (Jenner & Arevalo Jr 2016).

6.4 Methods

This study was conducted using twelve Li-, Be- and B-bearing minerals representing a range of Li, Be and B compositions (Table 6-1). The range of minerals analyzed includes borates, boro-silicates and silicates. The LAM system used for analysis was an Australian Scientific Instruments RESOlution M-50 LA-ICP-MS system equipped with a Coherent CompexPro ArF excimer laser with $\lambda = 193$ nm and an output energy of 6 J/cm^2. For analysis, the minerals were mounted and polished in an epoxy puck. Each mineral was analyzed using laser-beam widths of 6, 9, 12, 16, 22, and 30 μm. For each beam width, a total of seven analysis points were collected to ensure that the measured LLE concentrations were consistent. Each of the spot sizes had a

repetition rate of 6 Hz**.** Both the NIST610 and 612 glasses as well as lithium metaborate ($LiBO_2$) and natural beryl (Fisher Quarry, Topsham, Maine) were used as standards. The NIST610 and 612 glasses contain LLE in ppm levels whereas $LiBO_2$ and beryl contain LLE at wt. % levels, similar to the minerals to be analyzed in this study. The $LiBO_2$ standard was created using $LiBO_2$ powder (Sigma-Aldrich) sintered at 150 °C for 24 hours. This produced well-formed, large (~ 3 x 7 x 8 mm) white, translucent crystals which were then mounted in epoxy. The $LiBO_2$ standard was then analyzed by Raman spectroscopy to confirm that it was lithium metaborate. The beryl from Fisher Quarry was chosen because it appeared to be relatively free of alteration. Additionally, preliminary tests using LA-ICP-MS line analyses of this beryl showed no variation Be signal intensity, suggesting Be is homogenously distributed. Lithium metaborate and beryl were selected as standards because they contain LLE in stoichiometric amounts (i.e. no evidence of Be zonation in beryl) and in concentrations similar in magnitude to those minerals being analyzed. The ablated material was analyzed using a Thermo X-Series II quadrupole ICP-MS with Ar as the carrier gas. Data were processed using the standard-independent procedure described below. The most recent Li, Be and B compositions for the NIST610 and NIST612 standards, given by Jochum *et al.* (2011), were used in this study (Table 6-2).

6.5 Data Processing

The reduction of laser ablation data to elemental concentrations normally involves the use of an internal standard where the concentration of the analytes in question (e.g. Si, Mg, Ca, etc.) have been determined by an independent methodology (e.g., EMPA). With LA-ICP-MS analysis, the absolute amount of material ablated varies from material to material due to differences in matrix and wavelength absorption and as such, the variations in the ablated material are corrected for

using an internal standard (Longerich et al. 1996). An alternative, standard-independent approach has been proposed by Liu et al. 2008, wherein the sum of metal oxides in the sample are normalized to 100% and an ablation yield correction factor (AYCF) is applied to correct for differences in the absolute amount of ablated material. The AYCF is calculated with the formula: AYCF = 100/ $\sum_{J-1}^{n}(cps_{sam}^{J} \times I^{J})$, $I^{J} = C_{rm}^{J}/cps_{rm}^{J}$, where cps_{rm}^{J} and cps_{sam}^{J} are the net count rates in the standard and the sample and C_{rm}^{J} is the concentration of the element in the standard (Liu et al. 2008). This method was only applied to anhydrous minerals (e.g., clinopyroxene, orthopyroxene, olivine, plagioclase, garnet and spinel) and not to hydrous ones. Our study thus provides an opportunity to test the limits to which this approach can be applied to hydrous minerals. For this study, it has been assumed that the H_2O content in the minerals being studied is present in stoichiometric concentrations. The approach used is identical to Liu et al. 2008, except that for the hydrous minerals, an amount equal to the stoichiometric concentration of water has been subtracted from the analytical total, with the remainder then being renormalized on an anhydrous basis.

6.6 Results

6.6.1 Lithium

The ideal, calculated, and measured Li concentrations, determined in this study using NIST610, 612, and $LiBO_2$, are presented in Table 6-1. Before discussing these in detail, it must be noted that as Li can be present as both ^{6}Li and ^{7}Li, the question of isotopic fractionation must be addressed. From this study, data for both Li isotopes are presented in Fig. 6-2; these show a strong 1:1, positive correlation (R^2 ~ 0.90), regardless of beam size used, indicating that isotopic fractionation does not occur to any significant degree and so is not expected to be a major source of error in this study. As such, the data presented in Table 1 are given only for ^{7}Li. From Table

1 it is clear that for most minerals, there is a good agreement between the measured Li and ideal Li concentrations (i.e., all agree to within ± 10% of the expected ideal values). The two exceptions are polylithionite and tainiolite, whose compositions deviate significantly (~ 20 - 30 % of the expected ideal values). Results from this study indicate that Li concentrations in polylithionite are generally over estimated (measured Li ~ 3.5 wt.% vs. ideal Li ~ 3.0 wt.%) whereas those for tainiolite are underestimated (measured Li ~ 1.4 wt.% vs. ideal Li 1.71 wt.%). The deviations from ideal and differences between the two phyllosilicates appear to be independent of the beam width that was used (Fig. 6-1).

The measured Li compositions, derived from NIST610 and 612, for the minerals analyzed appear to be internally consistent with each other (*i.e.*, within ± 10%). The Li compositions derived from the NIST glasses however show a greater deviation from the measured values determined using $LiBO_2$ (from within ± 10 % to ± 30%). This is especially true for tainiolite where the Li concentrations derived from the NIST glasses are ~ 1.4 wt.% compared to ~ 2 wt.% Li from $LiBO_2$, a 30% difference. It is noteworthy that for the Li compositions derived from NIST610, the associated errors are relatively small (error: ± 0.05 to ± 0.39 wt. %) relative to those obtained using $LiBO_2$ (error: ± 0.24 to ± 0.49 wt. %) and NIST612 (error: ± 0.05 to ± 1.76 wt. %). The results also indicate that NIST610 might be considered as the preferred standard, given its slightly lower associated error relative to those of NIST612 and $LiBO_2$.

6.6.2 Beryllium

The ideal and calculated Be contents for the minerals examined in this study are given in Table 6-1 and compared with the ideal concentrations in Fig. 6-2. In addition to the use of NIST610 and 612, a natural beryl from Fisher Quarry, Topsham, Maine, was also used. Overall, there is a good agreement between the measured and ideal Be compositions for most of the minerals

examined (i.e., chrysoberyl, beryl, tugtupite), these falling within ± 10% of the expected values, regardless of beam width used. The exception is phenakite, where the obtained values are highly variable (ranging from ~ 24 – 15 wt. % Be) and in general, higher than expected ideal Be composition (16.37 wt. %). It is also noted that there appears to be a weak negative correlation (R^2 ~ 0.60) between the obtained composition and the beam width (Fig. 6-2). In addition to good agreement with the ideal Be composition, the values derived from the three standards also agree well with each other (i.e., the standards are internally consistent). Figure 6-2 shows that the Be values from NIST610 and 612 along with beryl agree to within 10% relative of each other.

6.6.3 Boron

The comparisons between the ideal wt. % and calculated wt. % values for B for the minerals are given in Table 6-1. As with Li, there are two isotopes of B: ^{10}B and ^{11}B, with relative abundances of 20 and 80 %, respectively (Palmer & Swihart 1996). To evaluate isotopic fractionation, B compositions were measured for the isotopes ^{11}B and ^{10}B and plotted against one another in figure 6-3. A correlation of ~ 1:1 (R^2 ~ 0.90) is observed between the ^{10}B and ^{11}B compositions for most minerals, the exception being inyoite. This mineral however, was observed to be highly unstable under the laser beam (*i.e.,* inyoite was observed to fragment into large μm scale pieces) thus the poor correlation between ^{10}B and ^{11}B observed for inyoite can be explained by this instability. Given the lack of any significant fractionation between the B isotopes and that ^{11}B is the more common of the two, the values plotted in figure 5 are for the latter. A comparison of the measured B compositions determined from the standards show that NIST610 and lithium metaborate agree to within 5% of each other whereas the NIST612 values are more variable, agreeing to within 10 % of the NIST610 and $LiBO_2$ standards.

6.7 Discussion

6.7.1 Standards

Measured Li, Be and B compositions were calculated using the NIST610 and 612 glasses as well as $LiBO_2$ and natural beryl. Of these standards, NIST610, $LiBO_2$, and beryl consistently gave compositions that are close (i.e., within ± 5 %) to the ideal values, while NIST612 gave compositions that deviate by ~± 5 to 10 %. The minerals analyzed in this study contained Li, Be, or B in wt. % levels similar to the Li and B composition of $LiBO_2$ and Be composition of beryl. The NIST612 and NIST610 glasses contain Li, Be and B in ppm levels however, NIST610 contains these elements in higher concentrations (Table 6-2; Jochum *et al*. 2011). For this reason, NIST610 likely gives light element compositions that are closer to the ideal values compared to NIST612. Although the NIST610, NIST612, $LiBO_2$, and beryl standards all give similar results, the compositions derived from NIST610 have smaller errors (1σ error: ± 0.05 to ± 1.68 wt.%) associated with them compared to those derived from the NIST 612 (1σ error: ± 0.57 to ±2.47), $LiBO_2$ (1σ error: ± 0.49 to ± 1.76 wt.%) and beryl (1σ error: ± 0.29 to ± 3.65 wt.%). For these reasons NIST610 should be considered as the most suitable standard for analysis of light elements at wt.% levels. Given that the measured compositions of the light elements derived from the NIST610 values generally agree to within ± 5 % of the ideal light element compositions of the minerals regardless of beam width used, LA-ICP-MS is a suitable alternative method for measuring light elements at the wt.% level.

6.7.2 Measured compositions of Li-minerals

Tainiolite and polylithionite (Table 6-1) are both members of the mica group and are thus expected to have similar matrices. Our study finds, however that measured Li values are underestimated for tainiolite but overestimated for polylithionite. Tainiolite, like other members

of the mica group has flexible crystal structure and thus other elements such as Ti, Fe, Al, Mg, and in some cases Na may substitute for Li in the crystal structure (Tichendorf *et al*. 2007). Such substitutions reduce the overall amount of Li in the structure of tainiolite thus resulting in measured Li concentrations that are lower than expected.

Elemental substitutions also occur in polylithionite, however they cannot explain the overestimated measured Li concentrations for this mineral. Lithium has a low atomic mass and as a result there are virtually no interferences with this element. In their trace element study of micas from the Tanco pegmatite, Lichtervelde *et al*. (2008) noted that for micas with up to 2 wt.% Li_2O, the Li concentrations determined by LA-ICP-MS deviated by 5 % from the expected ideal values. For micas, such as polylithionite, with 6 wt.% Li_2O, measured Li concentrations from LA-ICP-MS can deviate by as much as 25% from expected ideal values (Lichtervelde *et al*. 2008). In this study, measured Li values are ~ 17% higher than the expected ideal values. The reasons for these discrepancies are unknown however, it shows that caution must be used when using LA-ICP-MS to measure Li in Li-rich micas. Very few studies by LA-ICP-MS have been conducted on other Li-rich minerals to determine whether major differences occur between measured and ideal Li concentrations. In our study, we find that the measured Li concentration of spodumene (~7.64 wt. % Li_2O) deviates by ± 5 % from the expected ideal value (8.03 wt. % Li_2O). Spodumene, unlike mica, is a chain silicate which could explain the good agreement between laser ablation derived Li concentrations and expected ideal values despite spodumene having Li_2O > 6 wt. %

6.7.3 Effect of Beam Width

One of the important aspects of this study was to evaluate the impact of varying beam diameters on the obtained concentrations for LLE examined in this study. To this end, the LA-ICP-MS

analyses were made with beam diameters ranging from 6 to 30 μm. Results (Fig. 2-1, 2-3 & 2-5) demonstrate that beam width has little effect on the final calculated LLE concentrations for all minerals, regardless of type and LLE concentration. The exception to this is the mineral eucryptite (ideal Li = 5.51 wt. %) where the Li concentrations vary from ~4 - 7 wt. % Li (Fig. 6-1). Eucryptite is a secondary mineral after spodumene and is often strongly intergrown with albite and as such the sample analyzed in this study may have contained inclusions of spodumene or albite. The presence of such inclusions is inferred from the large (Li ranges from ~ 4 to 7 wt. %) range in measured compositions and the fact that these Li compositions show no correlation with beam width. During analysis, it was not possible to collect data at the same point using the different beam widths and as such the beam may have analyzed areas containing inclusions. Although beam width had little effect on the final LLE concentrations, increasing beam width increases the count rate as well as lowers the calculated detection limit (Kent & Ungerer 2006).

6.8 Conclusions

- Beam width has very little effect on final measured LLE concentrations however increasing beam width will lower detection limits. The compositions of most minerals, regardless of beam width, fall to within ± 10% of the ideal LLE composition.
- Of the NIST glasses, NIST610 is most suitable for measuring LLE's at wt.% levels. The NIST610 standard gave LLE compositions that were within ± 5% of the ideal composition compared to ± 5 – 10% for NIST 612.
- Natural minerals such as beryl may also be suitable standards for LLE's at wt.% levels provided that they are relatively uniform and free of zonation. The beryl standard used in

this study gave LLE compositions that were within ± 5% of the ideal composition, similar to NIST610

- Lithium metaborate, natural beryl, and NIST610 all gave LLE compositions within ± 5% of the ideal composition for the minerals. Out of these standards NIST610 had the smallest associated errors (± 0.05 to ± 1.68 wt.%) compared to NIST612 (error ± 0.57 to ±2.47) $LiBO_2$ (error: ± 0.49 to ± 1.76 wt.%) and natural beryl (error: ± 0.29 to ± 3.65 wt.%) and is thus considered to be the more suitable standard.
- LA-ICP-MS is a suitable method for measuring LLE at wt.% levels, for most minerals, based on the above conclusions. This technique, however, may not be suitable for micas with Li_2O = 6 wt.%.

6.9 References

Andreozzi, G.B., Lucchesi, S., Graziani, G. & Russo, U. (2004): Site distribution of Fe2+ and Fe3+ in the axinite mineral group: new crystal-chemical formula. American Mineralogist, 89, 1763-1771.

Armbruster, T., Richards, R.P., Gnos, E., Pettke, T., & Herwegh, M. (2007): Unusual fibrous sodian tainiolite epitactic on phlogopite from marble xenoliths of Mont Saint-Hilaire, Quebec, Canada. Canadian Mineralogist, 45, 541-549.

Bastin, G.F., & Heijligers, H.J.M. (1992): Quantitative EPMA of the ultra-light elements boron through oxygen. Mikrochimica Acta, 12, 19-36.

Breiter, K., Vaňkova, M., Galiová, M.V., Korbelova, Z., & Kanicky V., (2017): Lithium and trace-element concentrations in trioctahedral micas from granites of different

geochemical types measured via laser ablation ICP-MS. Mineralogical Magazine, 81, 15-33.

Brigatti, M. F., Caprilli, E., Malferrari, D., Medici, L., & Poppi, L. (2005): Crystal structure and chemistry of trilithionite-2M2 and polylithionite-2M2. European Journal of Mineralogy, 17, 475-481.

Chaussidon, M. & Libourel, G. (1993): Boron partitioning in the upper mantle: An experimental and ion probe study. Geochimica et Cosmochimica Acta, 57, 5053-5062.

Domanik, K.J., Hervig, R.L., & Peacock, S.M. (1993): Beryllium and boron in subduction zone minerals: An ion microprobe study. Geochimica et Cosmochimica Acta, 57, 4997-5010.

Eggins SM, Kinsley LPJ, & Shelley JMG (1998): Deposition and element fractionation processes during atmospheric pressure laser sampling for analysis by ICP-MS. Applied Surface Science, 127-129, 278-286.

Elmi, C., Brigatti, M.F., Guggenheim, S., Pasquali, L., Montecchi, M., & Nannarone, S. (2014): Crystal chemistry and surface configurations of two polylithionite-1M crystals. American Mineralogist, 99, 2049-2059.

Guillong M, & Günther D (2002): Effect of particle size distribution on ICP-induced elemental fractionation in laser-ablation-inductively coupled plasma-mass spectrometry. Journal of Analytical Atomic Spectrometry, 17, 831-837.

Hawthorne, F.C., Cooper, M., Bottazzi, P., Ottolini, L., Ercit, S.T., & Grew E.S. (1995): Micro-analysis of minerals for boron by SREF, SIMS, and EMPA: A comparative study. Canadian Mineralogist, 33, 389-397.

Hawthorne, F.C., & Grice, J.D. (1990): Crystal-structure analysis as a chemical analytical method: application to light elements. Canadian Mineralogist, 28, 693-702.

Hervig, R.L., Mazdab, F.K., Williams, P., Guan, Y., Huss, G.R., & Leshin, L.A. (2006): Useful ion yields for Cameca IMS 3f and 6f SIMS: Limits on quantitative analysis. Chemical Geology, 227, 83 – 99.

Jenner, F.E. & Arevalo Jr. R.D. (2016): Major and trace element analysis of natural and experimental igneous systems using LA-ICP-MS. Elements, 12, 311-316.

Jochum, K.P., Weis, U., Stoll, B., Kuzmin, D., Yang, Q., Raczek, I., Jacob, D.E., Stracke, A., Birbaum, K., Frick, D.A., Gunther, D., & Enzweiler, J. (2011): Determination of reference values for NIST SRM 610 – 617 glasses following ISO guidelines. Geostandards and Geoanalytical Research. 35, 397-429.

Kent, A.J.R. & Rossman, G.R. (2002): Hydrogen, lithium, and boron in mantle-derived olivine: the role of coupled substitutions. American Mineralogist, 87, 1432-1436.

Kent, A.J.R. & Ungerer, C.A. (2006): Analysis of light lithophile elements (Li, Be, B) by laser ablation ICP-MS: comparison between magnetic sector and quadrupole ICP-MS. American Mineralogist, 91, 1401-1411.

Kusachi, I., Kobayashi, S., Tanabe, M., Kishi, S., & Yamakawa, J. (2004): Inyoite from Fuka, Okayama Prefecture, Japan. Journal of Mineralogical and Petrological Sciences, 99, 67-71.

Leeman, W.P. & Sisson, V.B. (1996): Geochemistry of Boron and its implications for crustal and mantle processes. In E.S. Grew, and L.M. Anovitz, Eds., Boron mineralogy, petrology

and geochemistry, 33, p. 645–707. Reviews in Mineralogy, Mineralogical Society of America, Chantilly, Virginia.

Lichtervelde, M., Gregoire, M., Linnen, R.L., Beziat, D., & Salvi, S. (2008): Trace element geochemistry by laser ablation ICP-MS of micas associated with Ta mineralization in the Tanco pegmatite, Manitoba, Canada. Contributions to Mineralogy and Petrology, 155, 791-806.

Liu, Y., Hu, Z., Gao, S., Gunther, D., Xu, J., Gao, C., & Chen, H. (2008): In situ analysis of major and trace elements of anhydrous minerals by LA-ICP-MS without applying an internal standard. Chemical Geology, 257, 34-43.

McGee, J.J., Slack, J.F., & Herrington, C.R. (1991): Boron analysis by electron microprobe using MoB_4C layered synthetic crystals. American Mineralogist, 76, 681-684.

Ottolini, L., Camara, F., Hawthorne, F.C., & Stirling, J. (2002): SIMS matrix effects in the analysis of light elements in silicate minerals: Comparison with SREF and EPMA data. American Mineralogist. 87, 1477-1485.

Ottolini, L., Camara, F., & Bigi, S. (2000): An investigation of matrix effects in the analysis of fluorine in humite-group minerals my EPMA, SIMS, and SREF. American Mineralogist. 85, 89-102.

Ottolini, L., Bottazzi, P., & Vannucci, R. (1993): Quantification of lithium, beryllium, and boron in silicates by secondary ion mass spectrometry using conventional energy filtering. Analytical Chemistry. 65, 1960-1968.

Palmer, M.R. & Swihart, G.H. (1996): Boron isotope geochemistry: An overview. In E.S. Grew, and L.M. Anovitz, Eds., Boron mineralogy, petrology and geochemistry, 33, p. 709–744. Reviews in Mineralogy, Mineralogical Society of America, Chantilly, Virginia.

Raudsepp M. (1995): Recent advances in the electron-probe micro-analysis of minerals for the light elements. Canadian Mineralogist, 33, 203-218.

Rinaldi, R., Gatta, D., & Angel, R.J., (2010): Crystal chemistry and low-temperature behavior of datolite: A single crystal X-ray diffraction study. American Mineralogist, 95, 1413-1421.

Ryan, J.G., Leeman, W.P., Morris, J.D., & Langmuir, C.H. (1996): The boron systematics of intraplate lavas: implications for crust and mantle evolution. Geochemica et Cosmochimica Acta, 60, 415-422.

Sardi, F., & Heimann, A. (2014): Pegmatitic beryl as indicator of melt evolution: example from the Velasco district, Pampeana Pegmatite Province, Argentina, and review of worldwide occurrences. Canadian Mineralogist, 52, 809-836.

Scambelluri, M., Muntener, O., Ottolini, L., Pettke, T.T., & Vannucci, R. (2004): The fate of B, Cl, and Li in the subducted oceanic mantle and in the antigorite breakdown fluids. Earth and Planetary Science Letters, 222, 217-234.

Tiepolo, M., Bouman, C., Vannucci, R. & Schwieters, J. (2006): Laser ablation multicollector ICP-MS determination of δ11B in geological samples. Applied Geochemistry, 21, 788-801.

Tiepolo, M., Zanetti, A., & Vannucci, R.(2005): Determination of Li, Be and B at trace level with Laser Ablation – Inductively Coupled Plasma – Sector Field Mass Spectrometry. Geostandards and Geoanalytical Research, 29, 211-224.

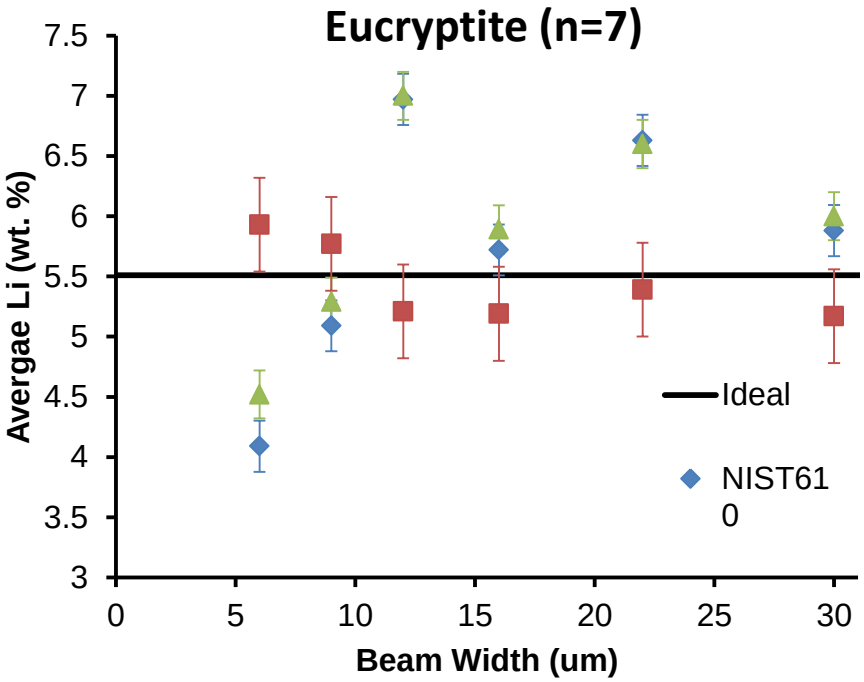
Eucryptite (n=7)
Avergae Li (wt. %)
7.5
7
6.5
6
5.5
5
4.5
4
3.5
3
0
5
10
15
20
25
30
Beam Width (um)
Ideal
NIST61
0

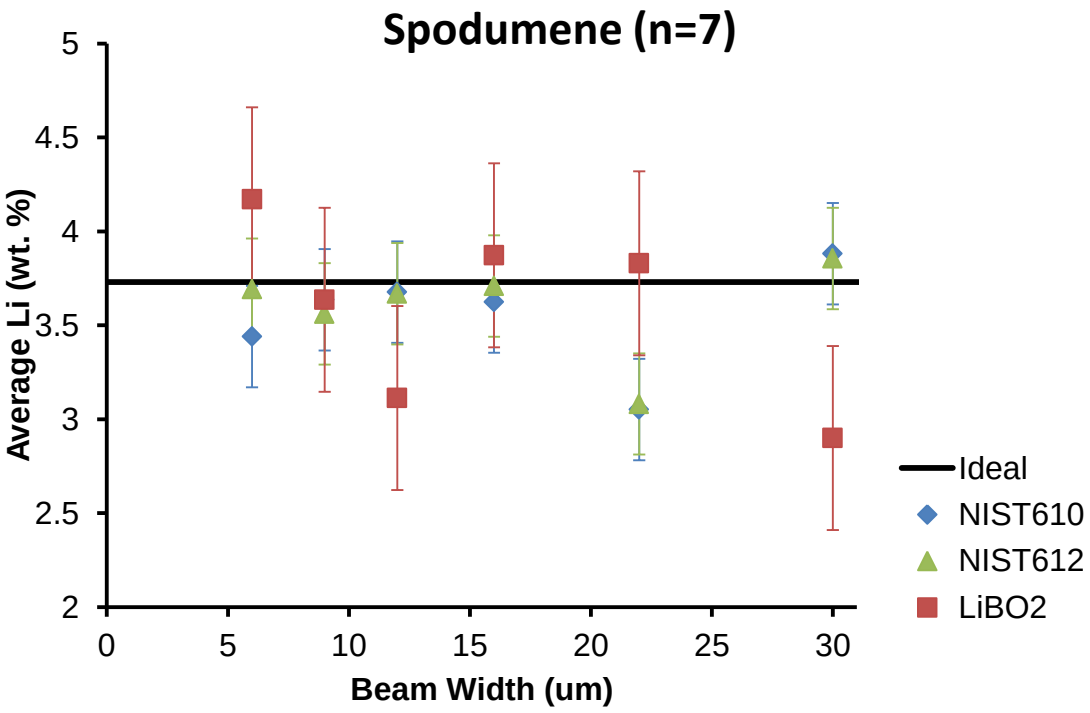
Spodumene (n=7)
Average Li (wt. %)
5
4.5
4
3.5
3
2.5
2
0
5
10
15
20
25
30
Beam Width (um)
Ideal
NIST610
NIST612
LiBO2

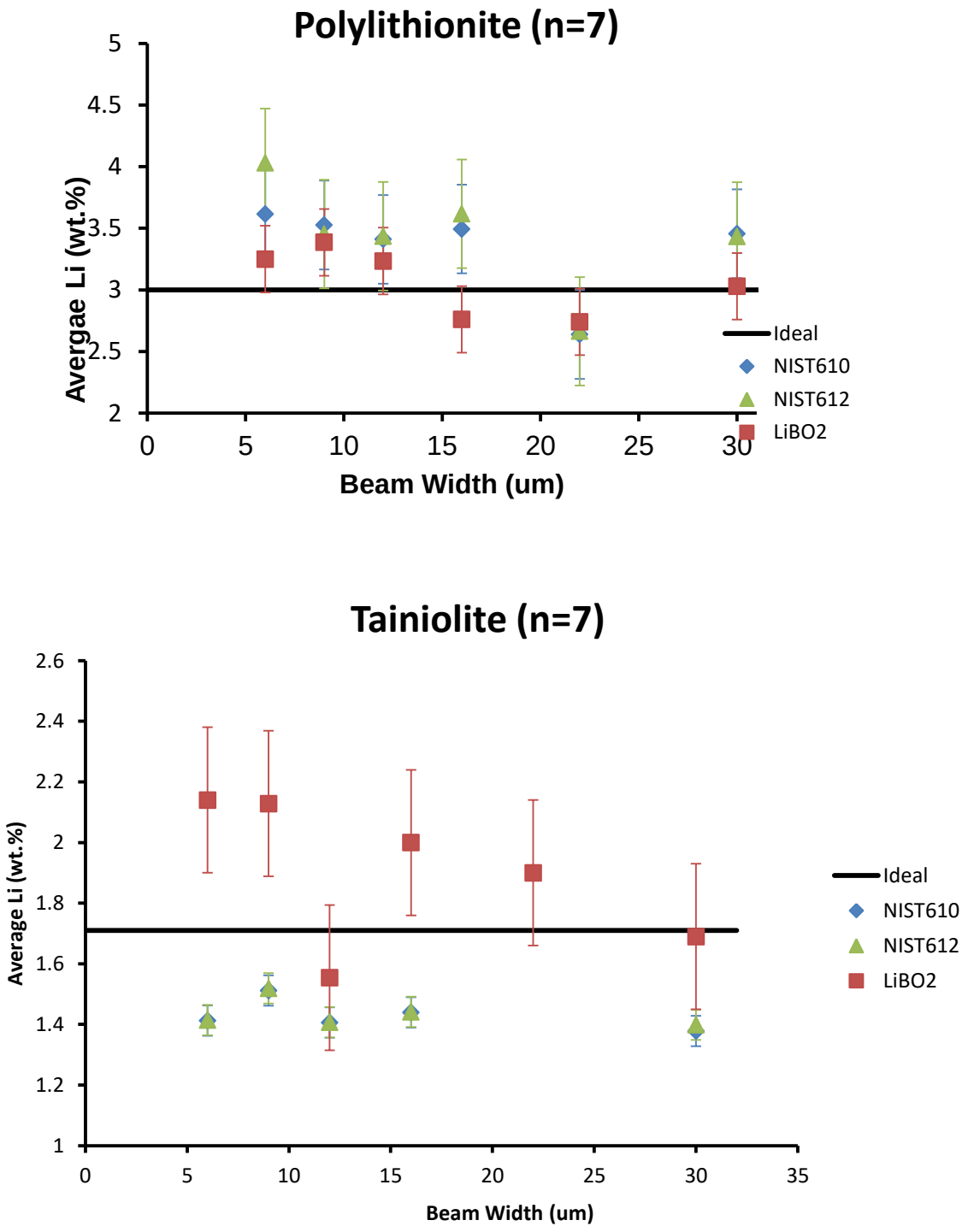

Figure 6-1. Measured and ideal Li compositions for eucryptite, spodumene, polylithionite, and tainiolite (error bars represent 1 SD).

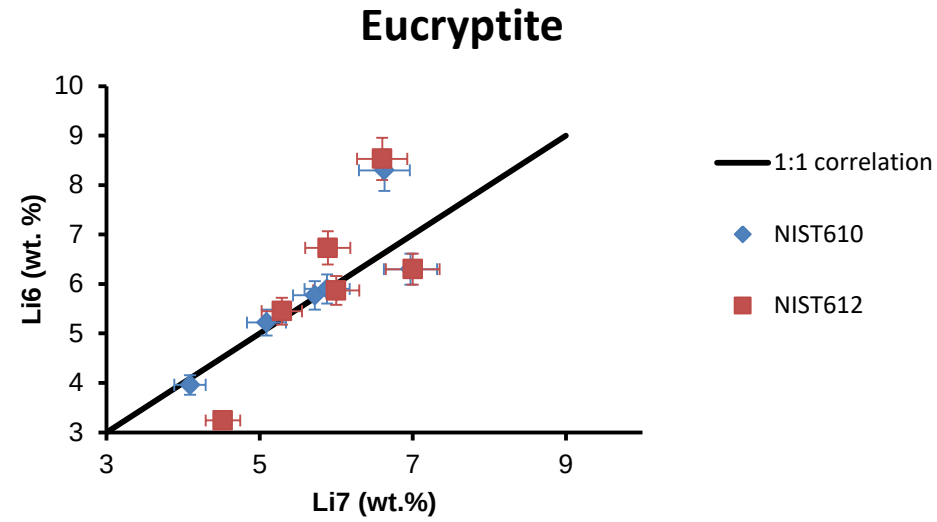
Eucryptite
Li6 (wt. %)
Li7 (wt.%)
10
9
8
7
6
5
4
3
3
5
7
9
1:1 correlation
NIST610
NIST612

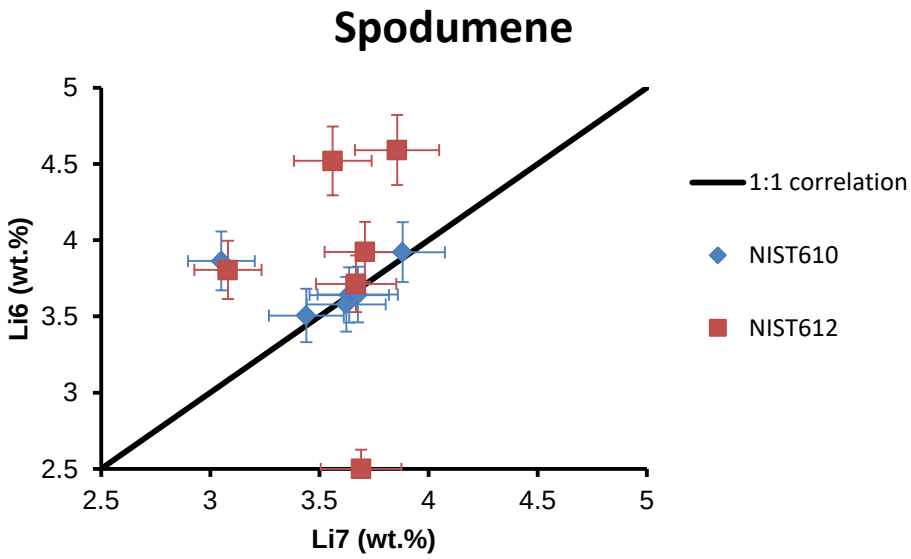
Spodumene
Li6 (wt.%)
Li7 (wt.%)
5
4.5
4
3.5
3
2.5
2.5
3
3.5
4
4.5
5
1:1 correlation
NIST610
NIST612

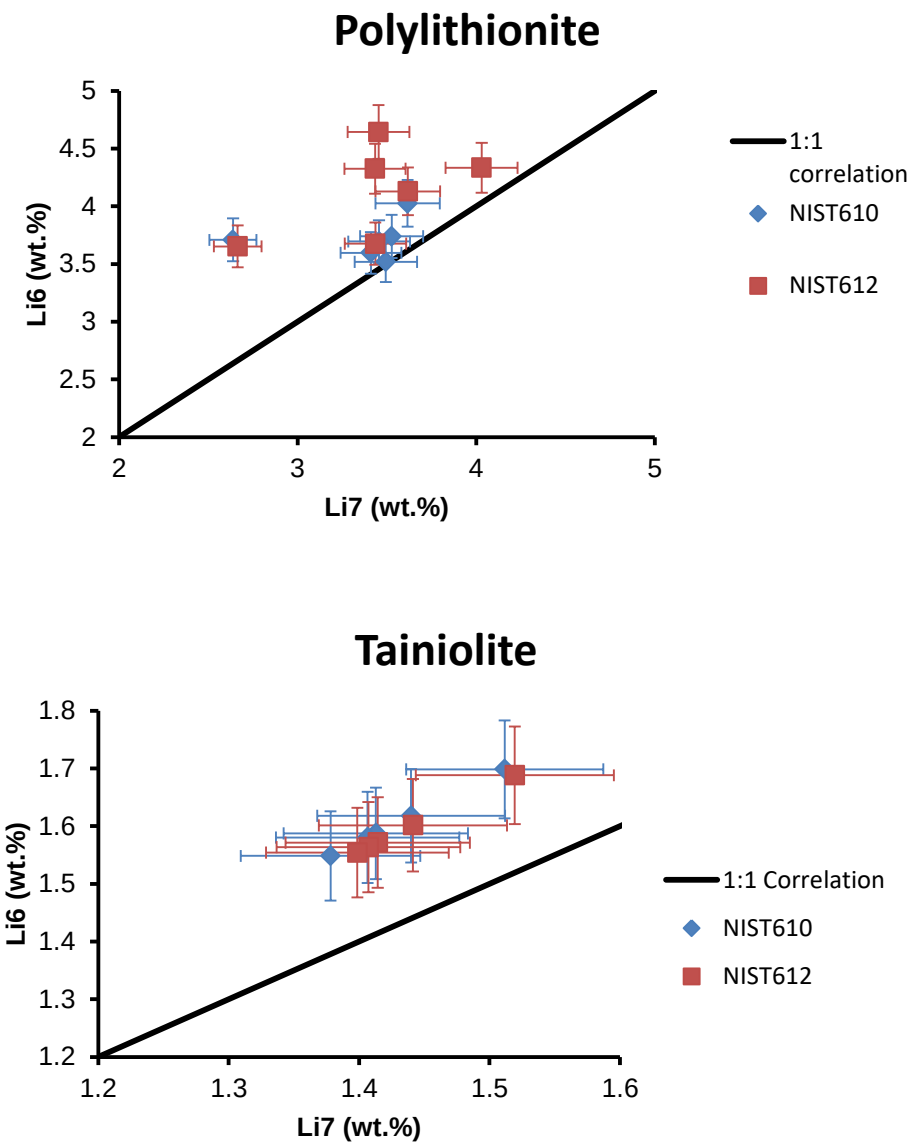

Figure 6-2. Agreement between Li^6 and Li^7 isotopes for the lithium minerals (black line represents 1:1 correlation, $R^2 \sim 0.90$)

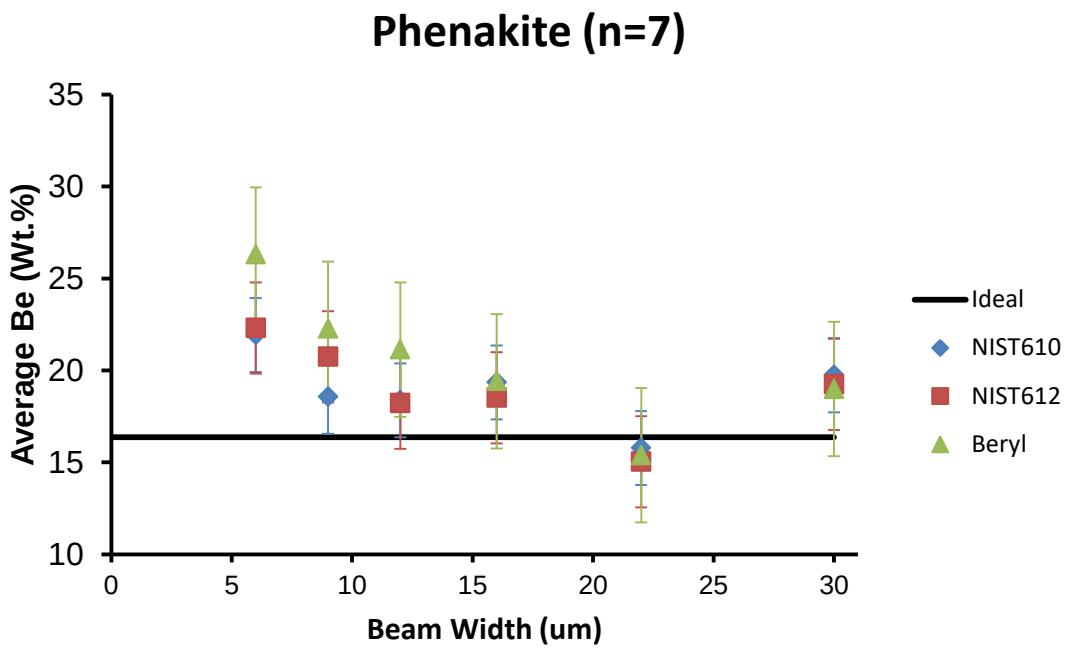
Phenakite (n=7)
Average Be (Wt.%)
35
30
25
20
15
10
0
5
10
15
20
25
30
Beam Width (um)
Ideal
NIST610
NIST612
Beryl

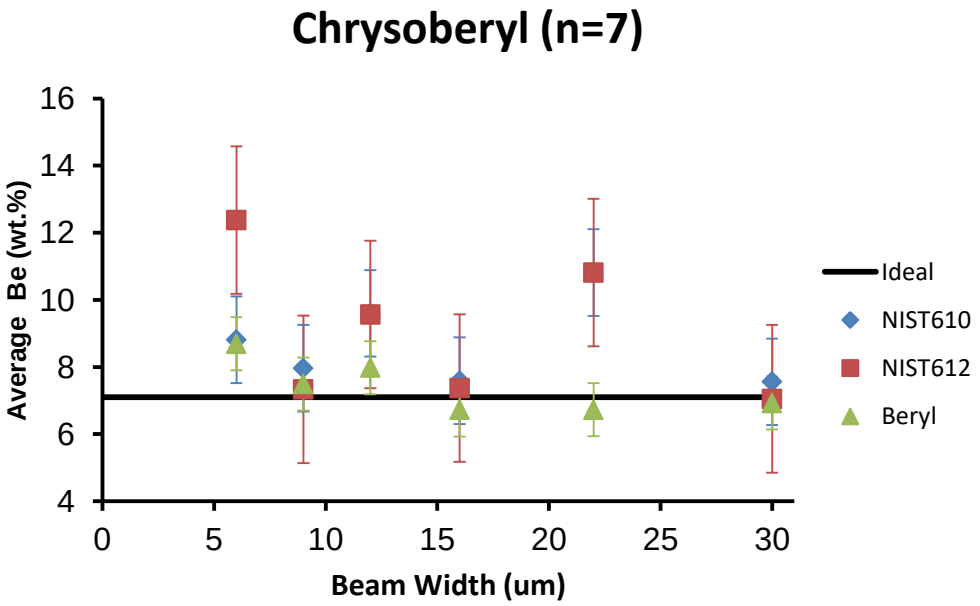
Chrysoberyl (n=7)
Average Be (wt.%)
16
14
12
10
8
6
4
0
5
10
15
20
25
30
Beam Width (um)
Ideal
NIST610
NIST612
Beryl

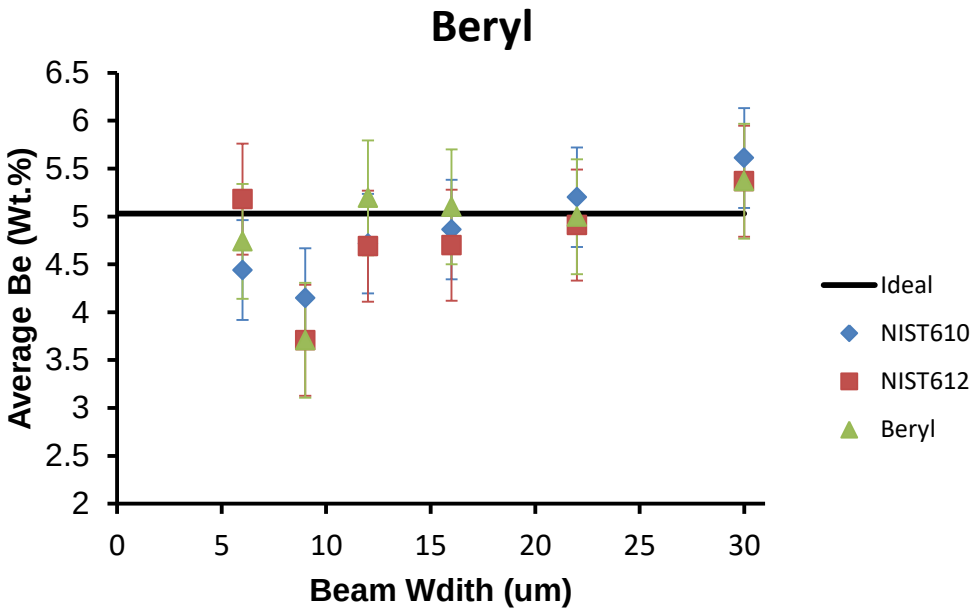
Beryl
Average Be (Wt.%)
6.5
6
5.5
5
4.5
4
3.5
3
2.5
2
0
5
10
15
20
25
30
Beam Wdith (um)
Ideal
NIST610
NIST612
Beryl

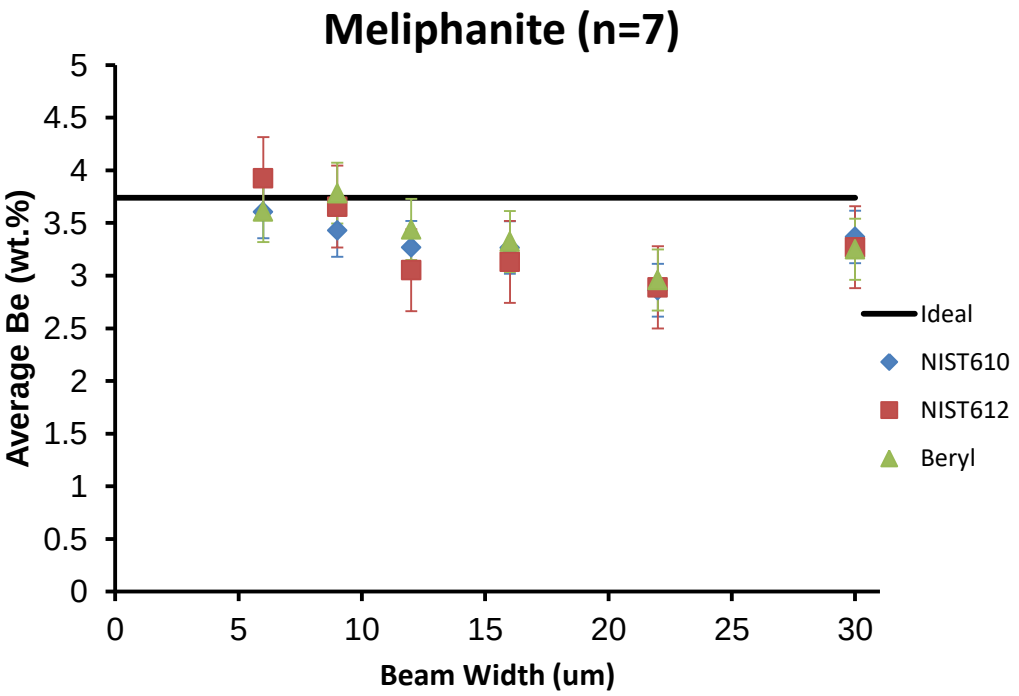
Meliphanite (n=7)
Average Be (wt.%)
5
4.5
4
3.5
3
2.5
2
1.5
1
0.5
0
0
5
10
15
20
25
30
Beam Width (um)
Ideal
NIST610
NIST612
Beryl

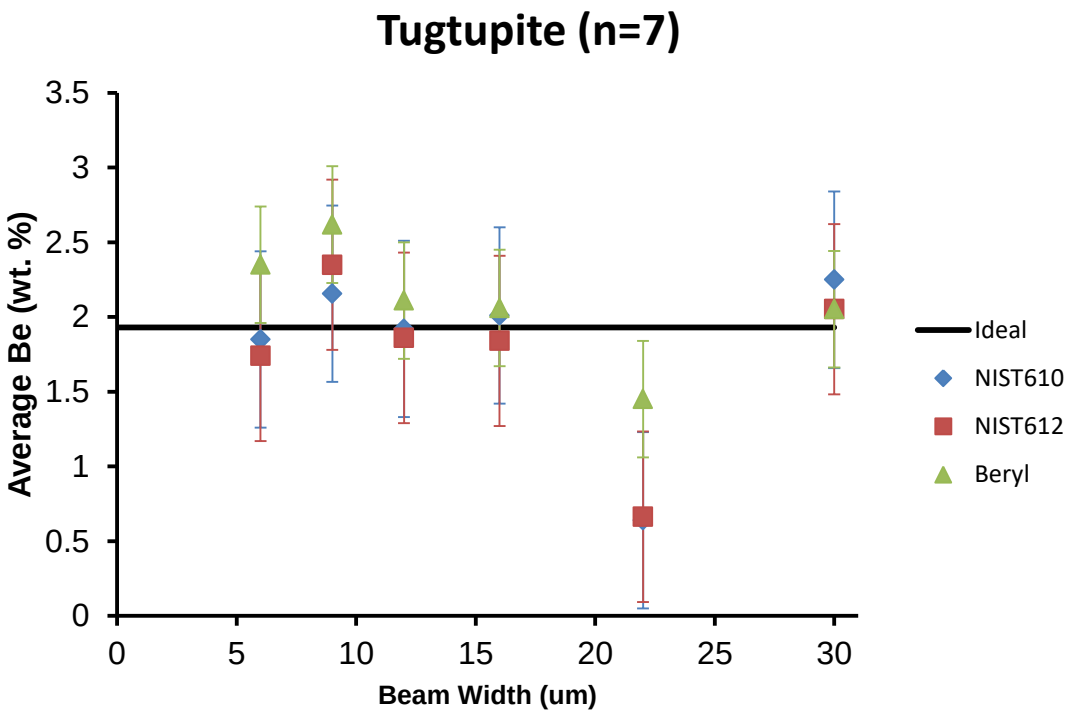

Figure 6-3. Ideal and measured Be compositions for phenakite, chrysoberyl, beryl, meliphanite and tugtupite (error bars represent 1 SD).

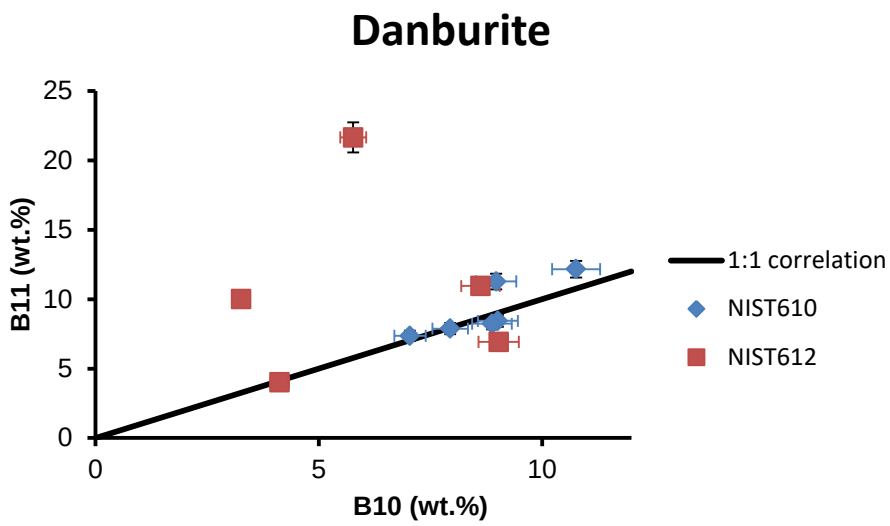
Danburite
25
20
15
10
5
0
B11 (wt.%)
0
5
10
B10 (wt.%)
1:1 correlation
NIST610
NIST612

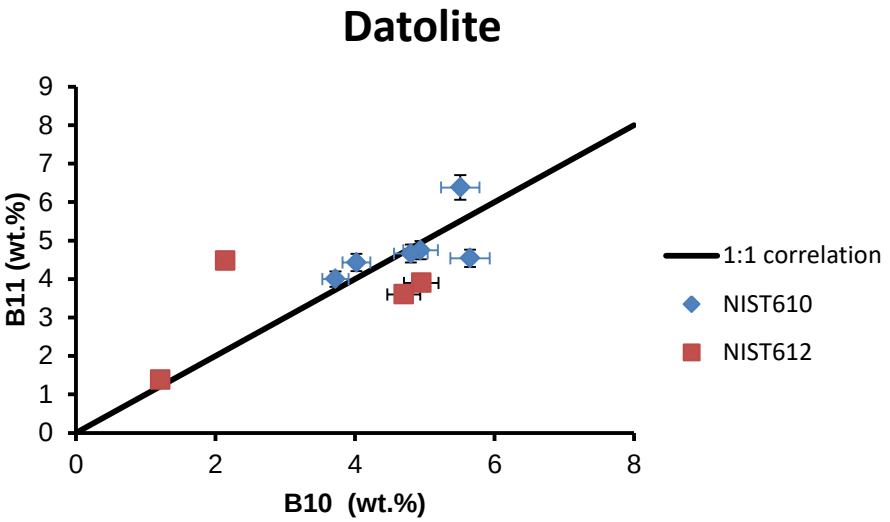
Datolite
9
8
7
6
5
4
3
2
1
0
B11 (wt.%)
0
2
4
6
8
B10 (wt.%)
1:1 correlation
NIST610
NIST612

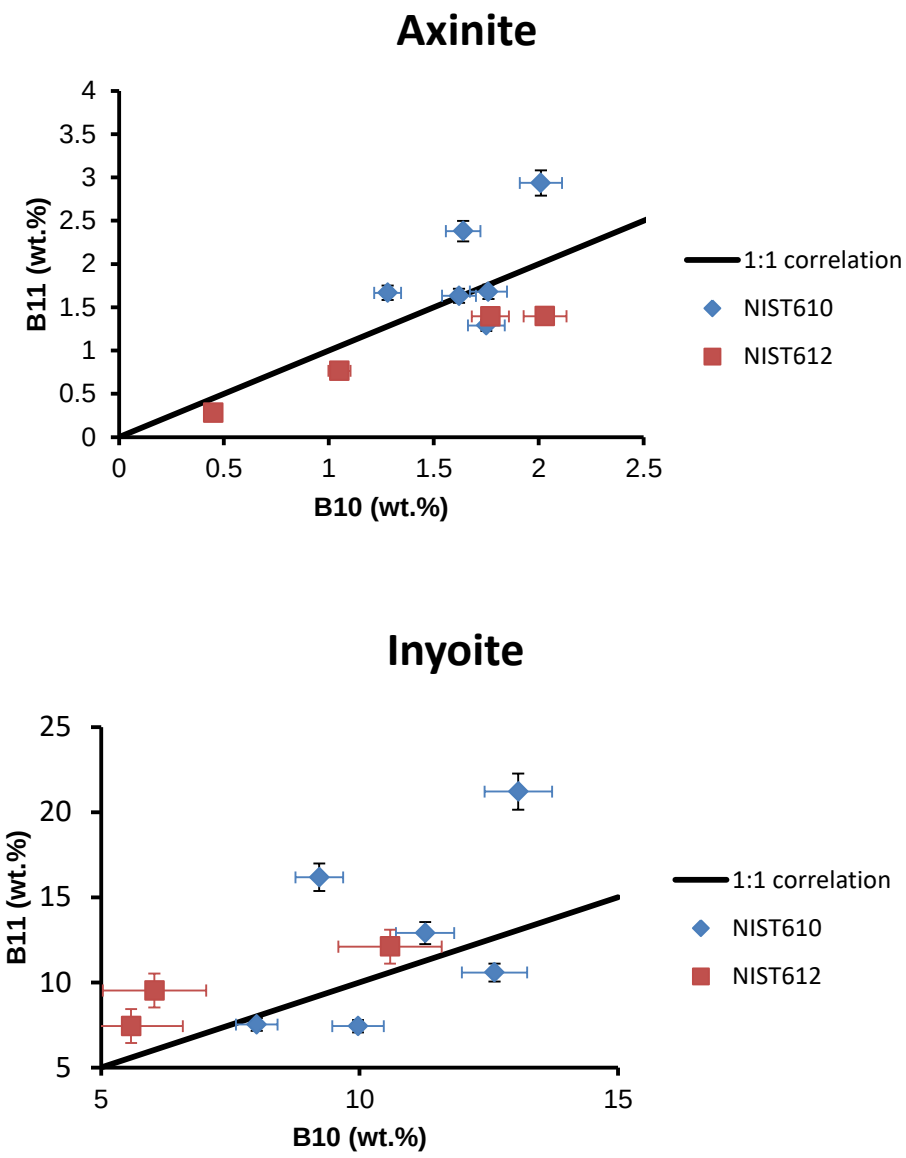

Figure 6-4. Agreement between B^{10} and B^{6} isotopes for the boron minerals.

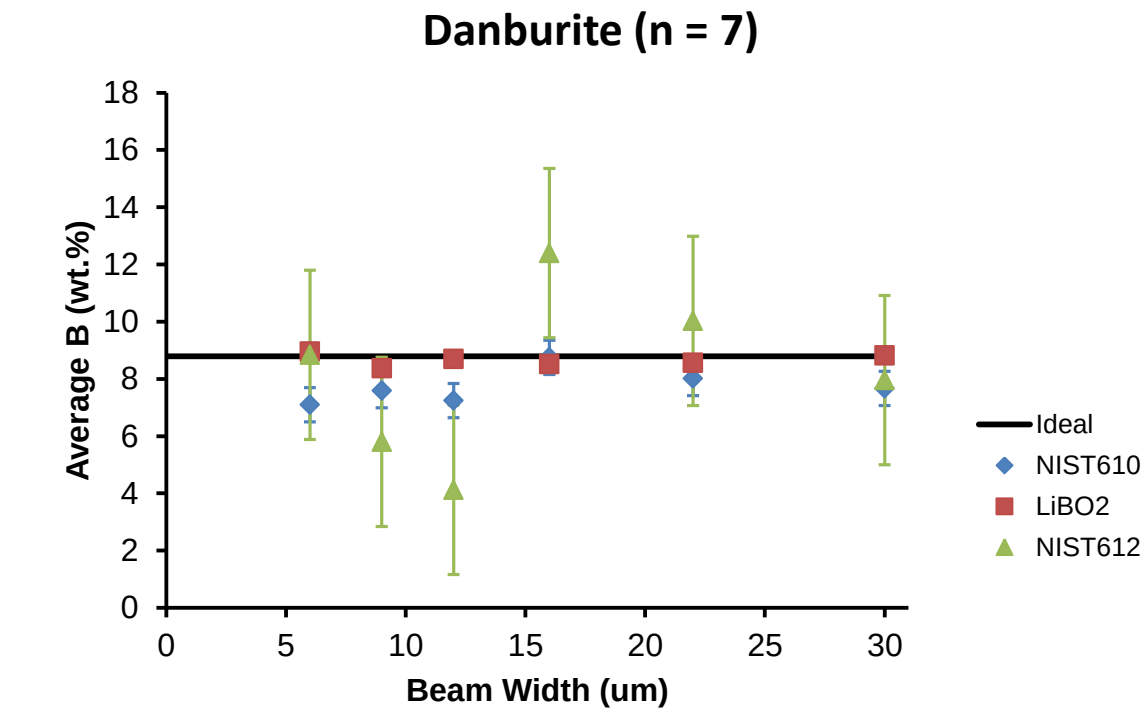
Danburite (n = 7)
Average B (wt.%)
Beam Width (um)
Ideal
NIST610
LiBO2
NIST612

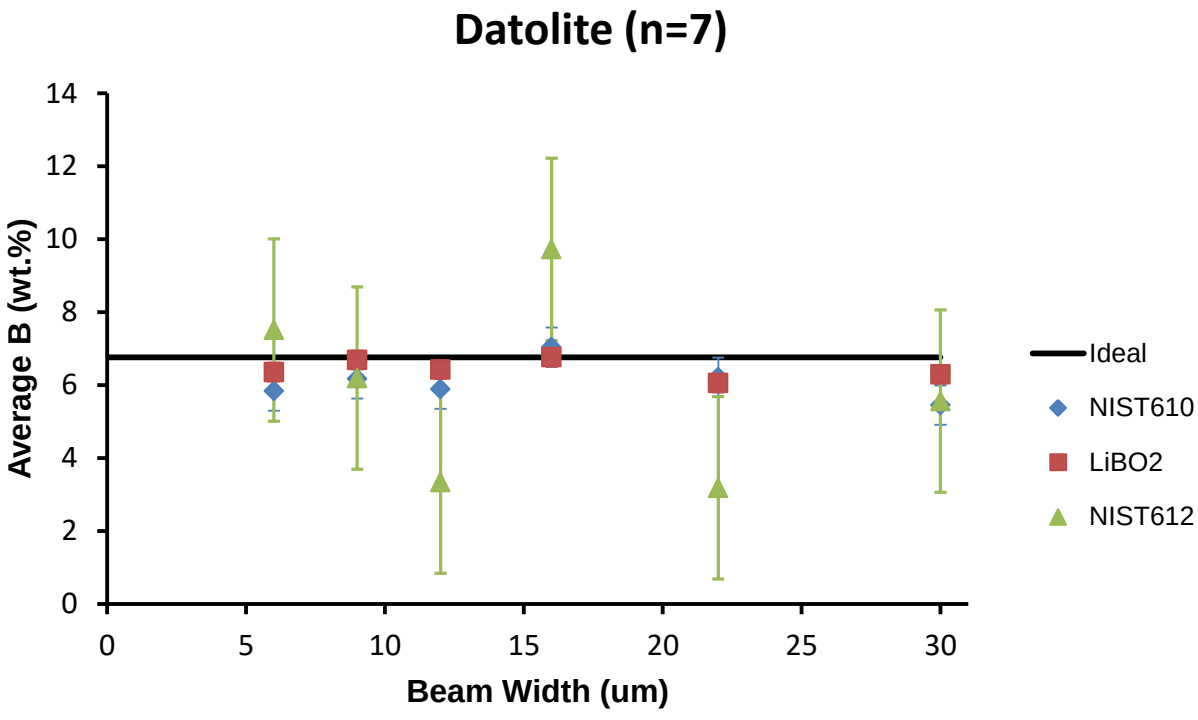
Datolite (n=7)
Average B (wt.%)
Beam Width (um)
Ideal
NIST610
LiBO2
NIST612

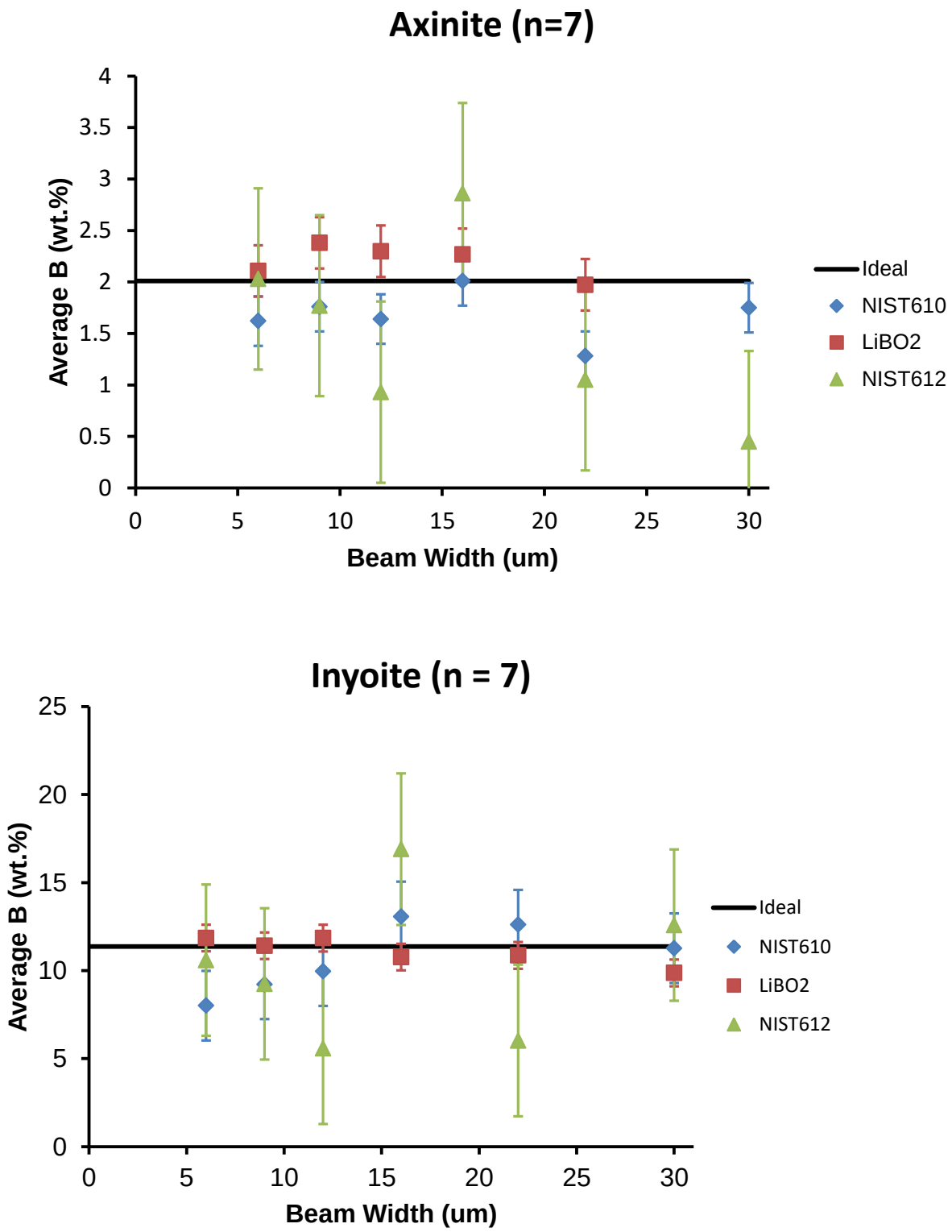

Figure 6-5. Ideal and measured B compositions for various B-bearing minerals (Error bars represent 1 SD)

Table 6-1. Data relating to the compositions, localities and ideal wt. % Li, Be, and B related to the minerals analyzed in this study.

B Minerals					
Mineral	Formula	Locality	Ideal wt. % B	Measured wt.% B	Range wt.% B
Axinite	$Ca_2(Mg,Fe)Al_2BO_3Si_4O_{12}(OH)$	Renison Bell Mine, Roseberry, Tasmania	2.01	1.88(3) (SIMS)[1]	1.77(2) - 1.96(3)
Datolite	$CaBSiO_4(OH)$	Farmington, Connecticut	6.76	7.36 (EPMA-WDS)[2]	7.22 - 7.48
Danburite	$CaB_2(SiO_4)_2$	Mina Aurora, Charcas	8.79	calc	-
Inoyite	$Ca_2B_2O_6(OH)_{10}•8H_2O$	U.S.B. Mine, Boron California	11.68	11.61 (EPMA-WDS)[3]	11.55 - 11.68

Be Minerals					
Mineral	Formula	Locality	Ideal wt.% Be	Measured wt.% Be	Range wt.% Be
Tugtupite	$Na_4AlBeSi_4O_{12}Cl$	Kvanfjeld, Greenland	1.93	calc	-
Meliphanite	(Ca,Na)2Be[(Si,Al)2O6(F,OH)]	Geiteroya, Langesundfjord Norway	3.74	calc	-
Beryl	$Be_3Al_2Si_6O_{18}$	Ray Mine, Burnsville North Carolina	5.03	4.60 (ICP-AES)[4]	4.29 - 5.07
Chrysoberyl	$BeAl_2O_4$	Lac Alatra, Madagascar	7.10	calc	-
Phenakite	Be_2SiO_4	Mt. Wheeler Mine, White Pine County, Nevada	16.37	calc	-

Li Minerals					
Mineral	Formula	Locality	Ideal wt. % Li	Measured wt. % Li	Range wt.% Li
Tainiolite	$KLiMg_2Si_4O_{10}(F,OH)_2$	Mont Saint Hilaire, Quebec	1.71	calc	-
Polylithionite	$KLi_2AlSi_4O_{10}(F,OH)_2$	Mont Saint Hilaire, Quebec	3.00	2.02 (LA-ICP-MS)[5]	1.65 - 2.44
				2.70 (ICP-AES)[6]	2.55 - 2.98
Spodumene	$LiAlSi_2O_6$	Baghlan, Nuristan Afganistan	3.73	calc	-
Eucryptite	$LiAlSiO_4$	Strickland Quarry, Portland, Connecticut	5.51	calc	-

1) Andreozzi et al. (2004)
2) Rinaldi et al. (2010)
3) Kusachi et al. (2004)
4) Sardi & Heimann (2014)
5) Elmi et al. (2014)
6) Brigatti et al. (2005)

Table 6-2. LLE compositions for NIST 610 and 612 glasses. Data from Jochum *et al*. (2011)

	NIST 610	NIST 612
Li (ppm)	468 ± 24	40.2 ± 1.3
Be (ppm)	476 ± 31	37.5 ± 1.5
B (ppm)	350 ± 56	34.3 ± 1.7